Autoregulation Modelling of Cerebral Haemodynamics

Katherine Tracey Moorhead

A thesis presented for the degree of
Master of Engineering
in
Mechanical Engineering
at the
University of Canterbury,
Christchurch, New Zealand.

14 March 2005

QP
108.5
.C4
.M825
2005

Acknowledgements

I would like to thank my research supervisors, Dr. J. Geoffrey Chase and Professor Tim David for their support and guidance over the last two years. I have been lucky to have supervisors who have played such active roles in the research. In particular, I would like to thank my primary supervisor, Geoff Chase. Geoff has been readily available to discuss ideas, motivate me when things were not going so well, and has spent a great deal of time helping me with journal articles and thesis writing. It was also Geoff who tricked me into presenting my research at the WC2003, which proved to be a very valuable learning experience.

Next, I would like to thank the rest of the 'Brain Group': It was great to have Dr John Fink from the Christchurch School of Medicine on hand to give the medical perspective. John was also really helpful in telling me which arterial geometries and clinical conditions to model, and what clinical responses to expect. He was very patient with my 'would this cause a stroke?' emails! When 'suffering appropriately', it is always more satisfying to have others suffering with you. Thanks then go to Stephen Moore, Samara Alzaidi, and Jade Arnold from the Brain Group. It has been useful to have people in the same research area to bounce ideas off.

I thank my friends in the BioEngineering Centre for what has been an enjoyable working environment. Lego and wasgij's providing interesting diversions from work. Most importantly, these guys usually knew how to fix my computer when it wasn't responding to FBH treatment.

Lastly, I would like to thank my family and friends for their support and encouragement. They always seemed to have faith when I was lacking. Finally to Dryden, because without the incentive of a celebratory exotic holiday, I might never have finished writing.

12 MAY 2005

Contents

List of Figures

List of Tables

Nomenclature

CoW	Circle of Willis
1D	One-Dimensional
3D	Three-Dimensional
CFD	Computational Fluid Dynamics
PID	Proportional-Integral-Derivative
MRA	Magnetic Resonance Angiogram
BA	Basilar Artery
LICA	Left Internal Carotid Artery
RICA	Right Internal Carotid Artery
$LPCA_1$	P1 Segment of Left Posterior Cerebral Artery
$RPCA_1$	P1 Segment of Right Posterior Cerebral Artery
LPCoA	Left Posterior Communicating Artery
RPCoA	Right Posterior Communicating Artery
$LACA_1$	A1 Segment of Left Anterior Cerebral Artery
$RACA_1$	A1 Segment of Right Anterior Cerebral Artery
ACoA	Anterior Communicating Artery
$LACA_2$	A2 Segment of Left Anterior Cerebral Artery
$RACA_2$	A2 Segment of Right Anterior Cerebral Artery
LMCA	Left Middle Cerebral Artery
RMCA	Right Middle Cerebral Artery
$LPCA_2$	P2 Segment of Left Posterior Cerebral Artery
$RPCA_2$	P2 Segment of Right Posterior Cerebral Artery
LAChA	Left Anterior Choroidal Artery
RAChA	Right Anterior Choroidal Artery
LScBA	Left Superior Cerebellar Artery
RScBA	Right Superior Cerebellar Artery
Ca^{2+}	Calcium ions
SR	Saroplasmic Reticulum
CaM	Calmodulin
CaCM	Ca^{2+}-CaM
MLCK	Myosin Light Chain Kinase
CBF	Cerebral Blood Flow
MAP	Mean Arterial Pressure
SA	Stretch Activated

PL-C	Phospholipase C
IP_3	Inositol Triphosphate
EDCF	Endothelium Derived Constricting Factor
EC	Endothelial Cell
EDRF	Endothelium Derived Relaxing Factor
CO_2	Carbon Dioxide
H^+	Hydrogen ions
K^+	Potassium ions
PO_2	Partial Pressure of Oxygen
TCD	Transcranial Doppler
MPM	Macroscopic Particle Model

Abstract

The Circle of Willis (CoW) is a ring-like structure of blood vessels found at the base of the brain. Its main function is to distribute a constant flow oxygen-rich arterial blood to the cerebral mass, despite changes in afferent pressures or flows. This objective is achieved by a local mechanism known as autoregulation, whereby the resistance in small vessels branching from the CoW changes by vasodilation or vasoconstriction of the smooth muscle cells surrounding the vessel.

A one-dimensional (1D) model of the CoW is developed to simulate a series of possible clinical scenarios such as occlusions in afferent arteries, absent or string-like circulus vessels, or arterial infarctions. A series of studies investigates various features of autoregulatory behaviour. Firstly, a simple model is created to verify solution methods; secondly, the model is validated against a three-dimensional (3D) Computational Fluid Dynamics (CFD) model; and lastly, the decentralised nature of cerebral autoregulation is investigated. Finally, an advanced, metabolic model of autoregulation is created, incorporating the successful aspects of the early model, as well as more physiologically accurate dynamics.

The advanced model captures cerebral haemodynamic autoregulation by using a Proportional-Integral-Derivative (PID) controller to modify efferent artery resistances and partial pressures of oxygen to maintain optimal efferent flow rates and oxygen supply to the cerebral mass for a given circle geometry and afferent blood pressure. This advanced model is physiologically relevant, matching the accepted physiological responses of blood flow as a function of arterial pressure, tissue oxygen partial pressure as a function of blood flow, as well as limited transient clinical data.

Results match accepted physiological response and exhibit excellent correlation with the limited clinical data available. In addition, a set of boundary

conditions and geometry is presented for which the autoregulated system cannot provide the necessary efferent flow rates and perfusion, representing a condition with increased risk of stroke and highlighting the importance of modelling the haemodynamics of the Circle of Willis. The system model created is computationally simple so it can be used to identify at-risk cerebral arterial geometries and conditions prior to surgery or other clinical procedures. In addition, the solution for the CoW arterial system is obtained in a far shorter time period using this time-varying resistance model than with higher dimensional CFD methods, and requires significantly less computational effort while retaining a high level of accuracy.

Chapter 1

Introduction

A stroke occurs when a blood vessel that carries oxygen and nutrients to the brain is blocked by a clot, leading to an ischaemic stroke, or bursts, causing a haemorrhagic stoke. Consequently, part of the brain cannot get the required oxygen and nutrients, and dies. Strokes can cause paralysis, affect language and vision, among other problems, and can often result in death. Modelling cerebral haemodynamics can be used to minimise stroke risk by identifying at-risk cerebral arterial geometries and boundary conditions prior to surgery or other clinical procedures. Hence, prior to a clinical intervention that may include significant variations in boundary pressures and flows, a simple patient specific model could be used to determine risk of stroke. The only requirement is a patient specific geometry available from Magnetic Resonance Angiogram (MRA) data.

1.1 Circle of Willis Structure

The Circle of Willis is a ring-like structure of blood vessels found beneath the hypothalamus at the base of the brain. Its main function is to distribute oxygen-rich arterial blood from the heart to the cerebral mass. Although the brain comprises only approximately two percent of the total body mass, it demands approximately twenty percent of the body's oxygen supply. If the brain cells are starved of oxygen for more than a few minutes due to decreased flow and perfusion pressure, many will become permanently damaged. More specifically, brain cell lysosomes being extremely sensitive to decreased oxygen levels can break open, releasing enzymes that bring about self-destruction of neural tissue. Figure 1.1 shows three orthographic projections of a MRA of an individual's

cerebro-vasculature. A schematic representation of the CoW based on the MRA is then shown in Figure 1.2 [Vander et al., 2001] labelling the major arteries considered in this study along with their abbreviations.

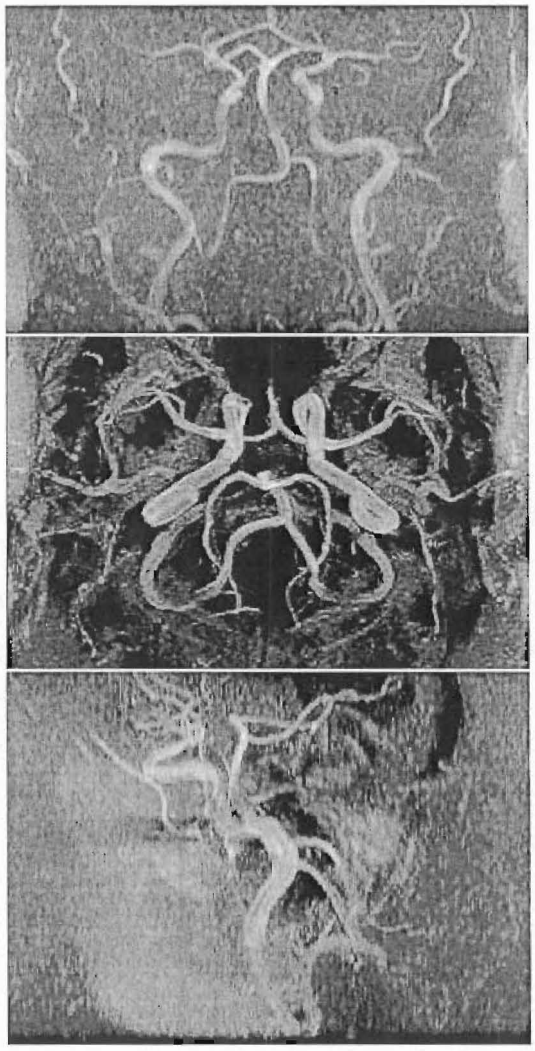

Figure 1.1 MRA Scan of an Individual's Cerebro-vasculature: Posterior View (*top*); Superior View (*middle*); Left View (*bottom*)

The Basilar Artery (BA) and the Internal Carotid Arteries (ICA's) supply the circulus arteries with oxygen-rich arterial blood, and because they bring blood *to* the CoW, are called afferent arteries. The circulus arteries distribute the oxygenated blood to the efferent arteries through the CoW. The efferent arteries are the route by which blood leaves the circulus vessels and supplies the four individual cerebral territories. Irrespective of pressure variations in the afferent vessels, the circulus vessels allow for a constant supply of blood to the cerebral mass, by

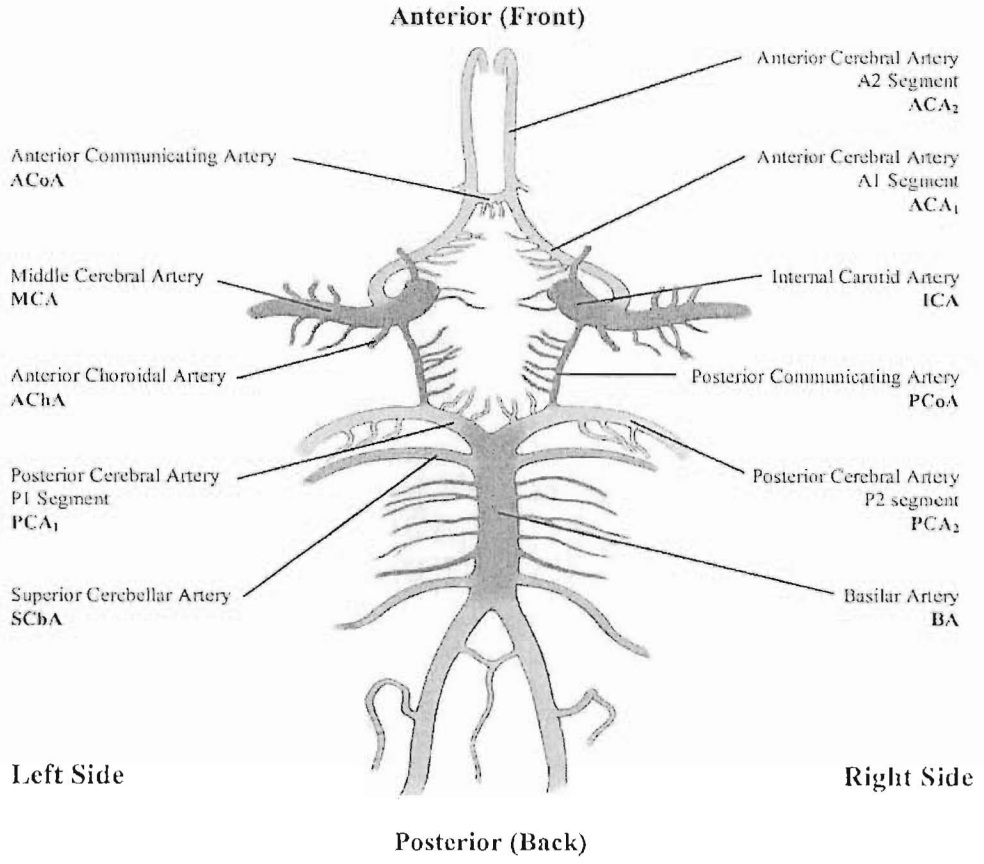

Figure 1.2 Circle of Willis Structure

vasoconstriction and vasodilation of the arterioles in the individual brain territories supplied by the efferent vessels. Each efferent artery predominantly supplies a particular cerebral volume and there is no redundancy in that supply, although there is some collateral supply across the brain at the level of the arterioles.

1.2 CoW Physiological Function

After its passage through the lungs, arterial blood is pumped by the left side of the heart into the aorta, providing oxygenated blood to all of the body. Three main arteries branch from the aorta: the brachiocephalic artery, the left common carotid artery, and the left subclavian artery. The brachiocephalic artery branches further into the right subclavian artery and the right common carotid artery. The left and right subclavian arteries give rise to the left and right vertebral arteries which then combine at the base of the brain in the BA, which supplies the CoW.

The common carotid arteries diverge into the external carotid arteries which supply facial muscles, and the ICA's which supply the CoW. The origins of the BA and ICA's are shown in Figure 1.3 [Tortora, 1997].

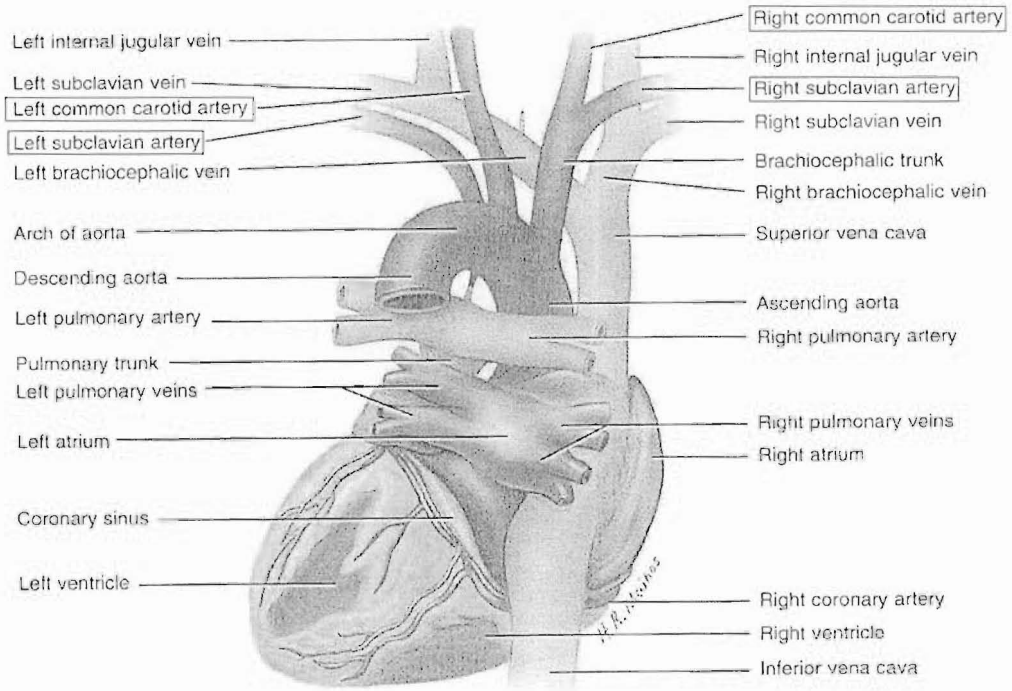

Figure 1.3 Scheme of Blood Distribution

More specifically, using Figure 1.2, the circle is composed of the Anterior Communicating Artery (ACoA), Left and Right A1 Anterior Cerebral Artery ($LACA_1$ and $RACA_1$, respectively), Left and Right Posterior Communicating Artery (LPCoA and RPCoA, respectively), and Left and Right P1 Posterior Cerebral Artery, ($LPCA_1$ and $RPCA_1$, respectively). The communicating arteries are much smaller than the other vessels within the CoW, and hence, as will be seen in Chapter 2, have a higher resistance to flow. As the PCoA's and ACoA's have a reduced diameter, they are more likely to be plagued by occlusions and hence appear string-like in many healthy individuals.

The purpose of the efferent arteries is to deliver arterial blood *from* the CoW to the cerebral tissue. There are ten main efferent arteries: A2 Anterior Cerebral Artery (ACA_2), P2 Posterior Cerebral Artery (PCA_2), Middle Cerebral Artery (MCA), Superior Cerebellar Artery (SCbA), and Anterior Choroidal Artery (AChA) on both the left and right sides. The four vascular territories

supplied by the efferent arteries are the lateral, medial, superior and inferior territories. Each of the territories obtains blood supply from the efferent arteries in varying proportions. The lateral, superior and inferior territories are perfused mainly by the MCA's, and the medial territories are perfused mainly by the ACA's [Ketchum, 2003]. Note that each efferent artery supplies a unique cerebral volume and there is no redundancy in that supply.

When arterial blood travelling from the efferent vessels reaches the peripheral tissues, the pressure difference encountered drives blood through the tissues. Diffusion of oxygen from the blood to the tissues is driven by the difference in partial pressure of oxygen between blood and tissues, which is, in part, a function of the driving pressures. If the blood flow through a particular tissue increases, there is a greater transport of oxygen such that the oxygen concentration in the interstitial fluid increases above the normal 40mmHg. The rate of oxygen consumption, that is the metabolic rate, also plays a role here. Guyton and Hall [1996] present a curve in which the interstitial partial pressure of oxygen is expressed as a function of the rate of blood flow, as shown in Figure 1.4.

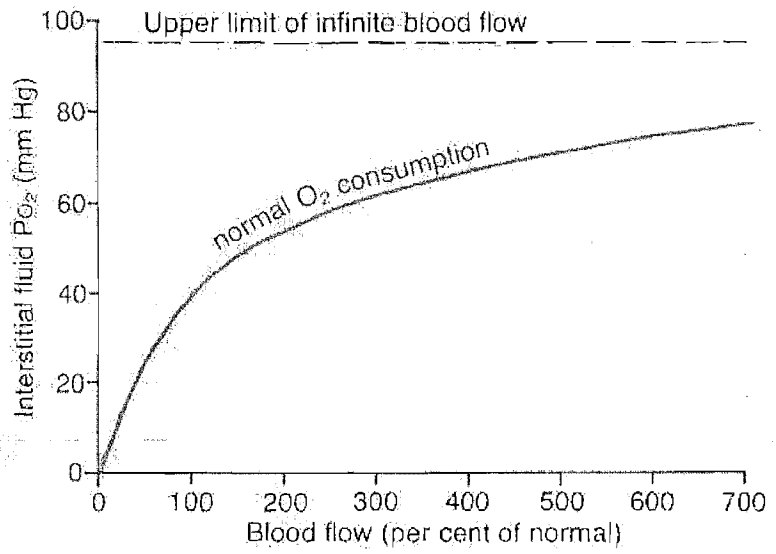

Figure 1.4 Interstitial Oxygen Partial Pressure as a Function of the Rate of Blood Flow

In the absence of the CoW, were any of the supply arteries to become occluded, the region of cerebral tissue usually supplied by that artery would be starved of oxygen and become ischaemic. Therefore, the great benefit of the circle structure lies in its ability to redirect blood from the afferent vessels to the region suffering a deficiency to maintain a constant supply of oxygenated

blood to all parts of the cerebral mass. This constant supply is achieved for a given artery by a process known as autoregulation where the resistance in small vessels branching from efferent arteries changes by either vasodilating or vasoconstricting. These changes enable an optimal reference flowrate to be maintained through each efferent artery to the cerebral tissue it supplies. Note that this form of control is decentralised, such that each of the territories must be satisfied independently of the requirements of the other territories.

1.3 Circle of Willis Abnormalities

While many individuals have a complete CoW geometry, various abnormalities are found, and these can be divided into four main categories: Absent vessels, string-like vessels, accessory vessels, and anomalous origins. All of these abnormalities have the potential to increase stroke risk under certain conditions.

Of the circulus vessels, the communicating vessels have a higher occurrence of omission [Alpers and Berry, 1963; Riggs and Rupp, 1963; Battacharji et al., 1967]. In a postmortem study of 350 CoW's, Alpers and Berry [1959] found that the PCoA was absent in 0.6% of cases, and the ACoA absent in 2% of cases. However, it should be noted that in all cases with an absent ACoA, the left and right ACA_1 fused, and later separated into the left and right ACA_2 at a variable distance. Thes added change has the effect of partly ameliorating the missing ACoA. These abnormalities are shown in Figure 1.5.

Alpers and Berry [1959] found that it is also the communicating vessels that are most likely to be appear string-like, a classification referring to a vessel with an external diameter less than 1mm. In 96 of the 350 circles studied string-like vessels were found, of which the PCoA was the most common. The ACoA was also found to be string-like in 10 of the circles studied, however this abnormality was often combined with duplication of the ACoA. The ACA_1 was also found to be string-like in 8 circles. A string-like PCoA is shown in Figure 1.6.

Accessory vessels refer to duplications or triplications of vessels associated with the CoW. Alpers and Berry [1959] found that such abnormalities occur most frequently in the anterior region of the CoW, in particular, in the ACA_2's and the ACoA. A triplicate ACA_2 was observed in 28 of the 350 cases, and accessory

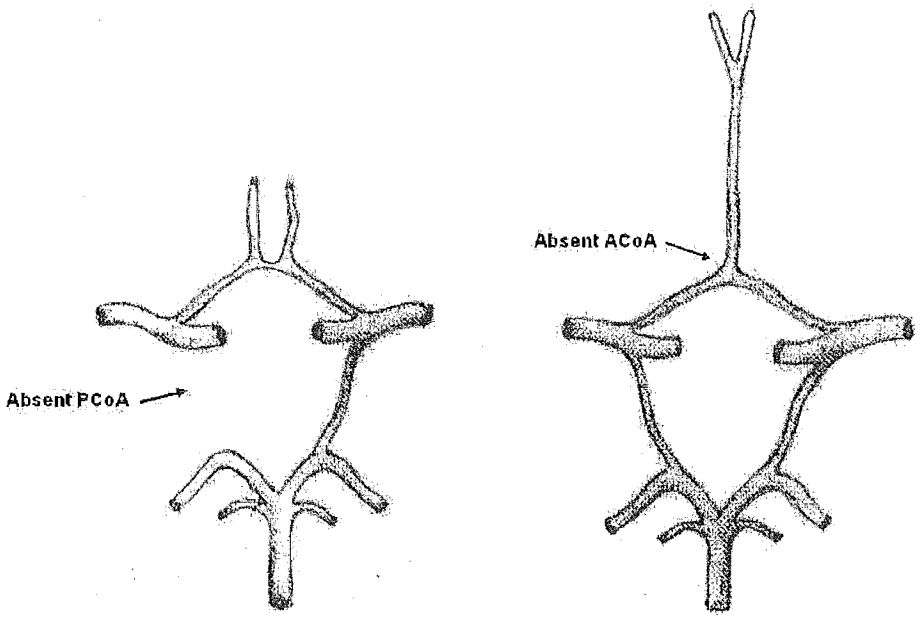

Figure 1.5 Absent Vessels: Absent PCoA (*left*); Absent ACoA with Fused ACA_1(*right*)

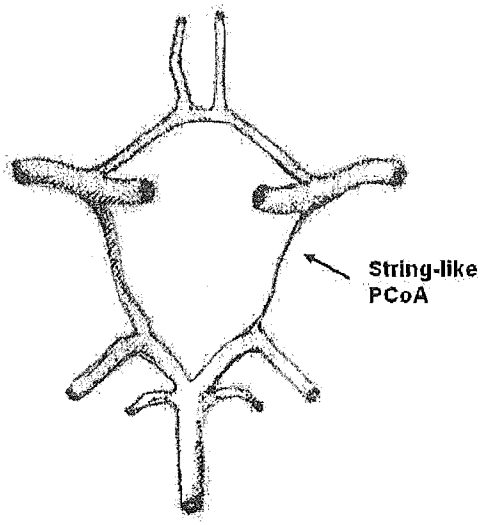

Figure 1.6 String-like Vessels: String-like PCoA

ACoA's were observed in 30 cases. These abnormalities are shown in Figure 1.7.

The most common vessel with an anomalous origin is the PCA_2, which on these occasions derives from the ipsilateral ICA instead of the BA. In this case, also known as a fetal P1, the ipsilateral PCA_1 then appears string-like, while the

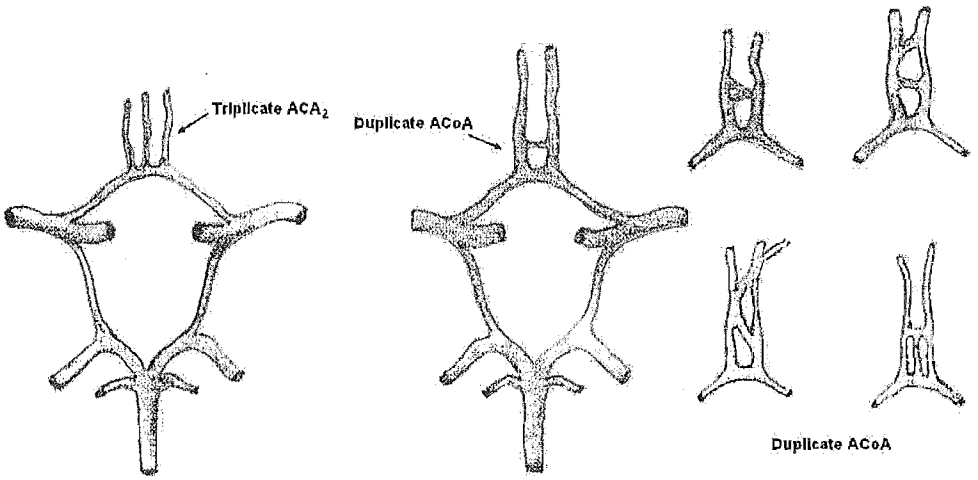

Figure 1.7 Accessory Vessels: Triplicate ACA_2 (*left*); Duplicate ACoA (*right*)

ipsilateral PCoA is greatly increased in size. Alpers and Berry [1959] discovered this abnormality in 51 of the 350 circles studied. Figure 1.8 shows a fetal P1.

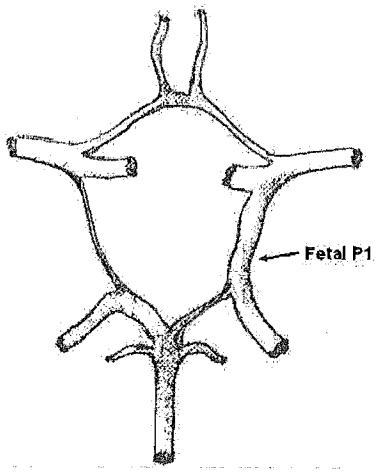

Figure 1.8 Vessels with Anomalous Origins: Fetal P1

While an individual possessing any of the variations discussed may, under normal circumstances, suffer no ill effects, there are certain clinical conditions, which compounded with effects of an absent or altered vessel, can lead to an ischaemic stroke. Hence, it is important to understand the dynamics associated with common abnormalities. Such data would be very useful for understanding potential outcomes prior to surgical or other intervention.

1.4 Smooth Muscle Contraction and Autoregulation

Despite any abnormalities, blood flow must be maintained in a tight range to all parts of the brain. Hence, a constant supply of blood and therefore nutrients is maintained to all parts of the cerebral mass despite variations in afferent flow by a process known as autoregulation. Autoregulation is a local mechanism whereby the resistance in small vessels branching from efferent arteries changes by either vasodilation or vasoconstriction of the smooth muscle cells surrounding the vessel. These changes are determined locally to maintain constant cerebral blood flow in that vessel or region.

Smooth muscle cells are organised into circular sheets around blood vessels, as shown in Figure 1.9 [Purves et al., 1995]. When they contract, this sheet shortens thus reducing the diameter of the vessel lumen. Smooth muscle cells contain thick filaments (myosin), thin filaments (actin), and intermediate filaments acting as a cytoskeleton. The thin filaments are anchored onto dense bodies, which are attached to the plasma membrane and held in place by intermediate filaments, as seen in Figure 1.10 [Randall et al., 2002].

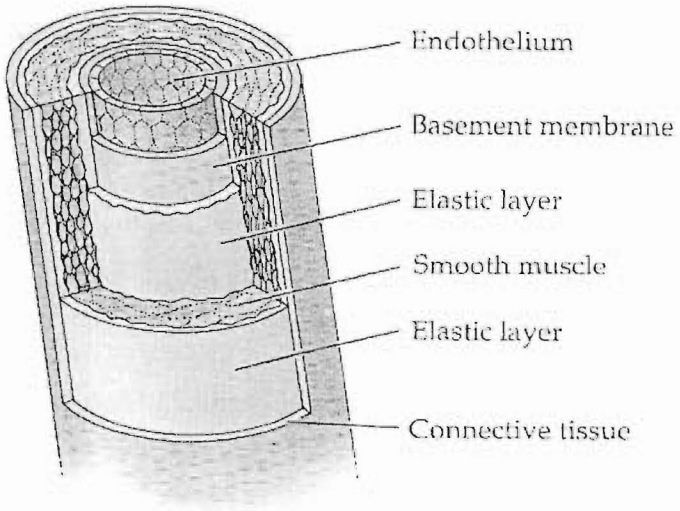

Figure 1.9 Arterial Wall

Myosin and actin on the thick and thin filaments, respectively, are aligned with each other. On cross-bridge formation and ATP hydrolysis, the myosin heads rotate, sliding the actin along the myosin, thus reducing the length of the muscle cell, as shown schematically in Figure 1.11 [Childs, 2001]. The result is

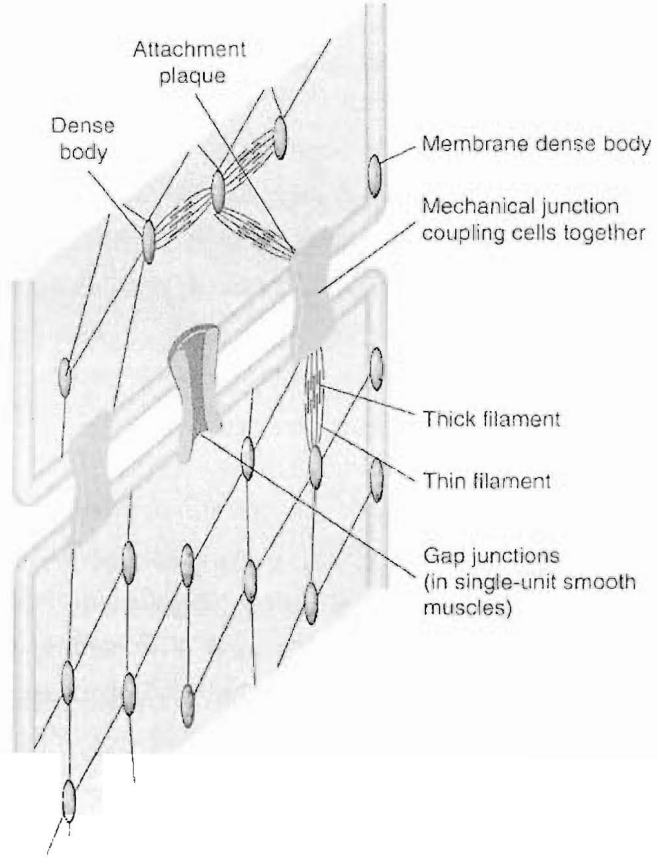

Figure 1.10 Alignment of Thick and Thin Filaments

smooth muscle contraction.

Smooth muscle cell contraction is initiated by an increase in free calcium ions (Ca^{2+}) in the cytosol, entering mostly from the extracellular fluid, but also from internal stores in the saroplasmic reticulum (SR). At low Ca^{2+} concentrations, caldesmon-tropomyosin binds to actin, thus blocking the myosin binding site. However, at intracellular Ca^{2+} concentrations greater than 10^{2+}M, Ca^{2+} combines with calmodulin (CaM) and the Ca^{2+}-CaM (CaCM) complex binds to caldesmon, dissociating it from actin and thus allowing association of actin with myosin, provided myosin is activated.

For myosin and actin to form cross-bridges, myosin must be activated either by binding Ca^{2+}, or by phosphorylation of its light chain by the CaCM-dependent enzyme myosin light chain kinase (MLCK), at the expense of ATP. Myosin is later deactivated by the enzyme myosin phosphatase when Ca^{2+} levels fall. When

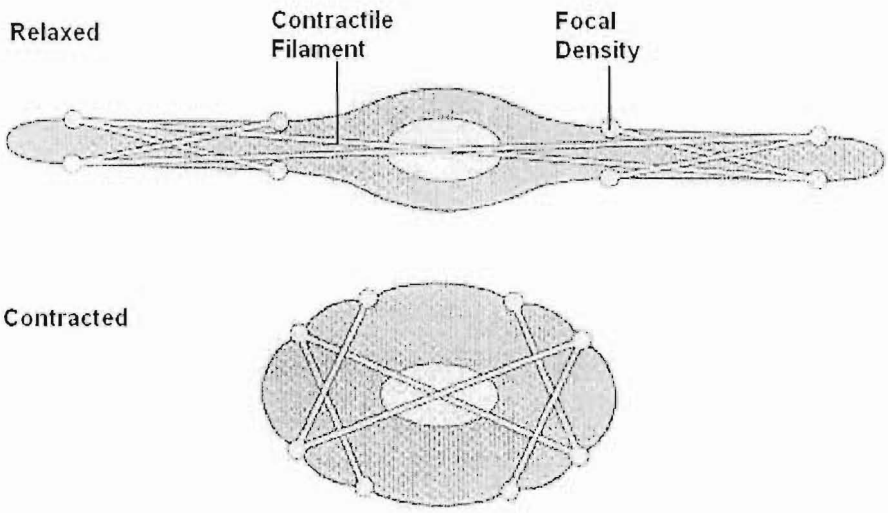

Figure 1.11 Schematic Smooth Muscle Cell

ATP binds to the myosin light chain, the ATP molecule splits into ADP and a phosphate group, and the high energy charged myosin head binds to actin forming a cross-bridge. Next the ADP and phosphate escape, resulting in a structural change in myosin causing the neck region to bend, sliding the actin along the myosin and shortening the length of the cell. When another ATP molecule binds to myosin, the actin and myosin dissociate.

Unlike skeletal muscle cells, smooth muscle contraction is prolonged because of slow cross-bridge cycling and an increased proportion of time of cross-bridge attachment. This is usually explained by smooth muscle cells having less ATP-ase activity, so that ATP hydrolysis driving myosin movement is reduced. This process is summarised in Figure 1.12 [San Mateo County Community College, 2002].

1.5 Autoregulation Physiology

There are two main autoregulation theories that explain how changes in flow and pressure act to change intracellular Ca^{2+}, and thus cause muscle vasomotion.

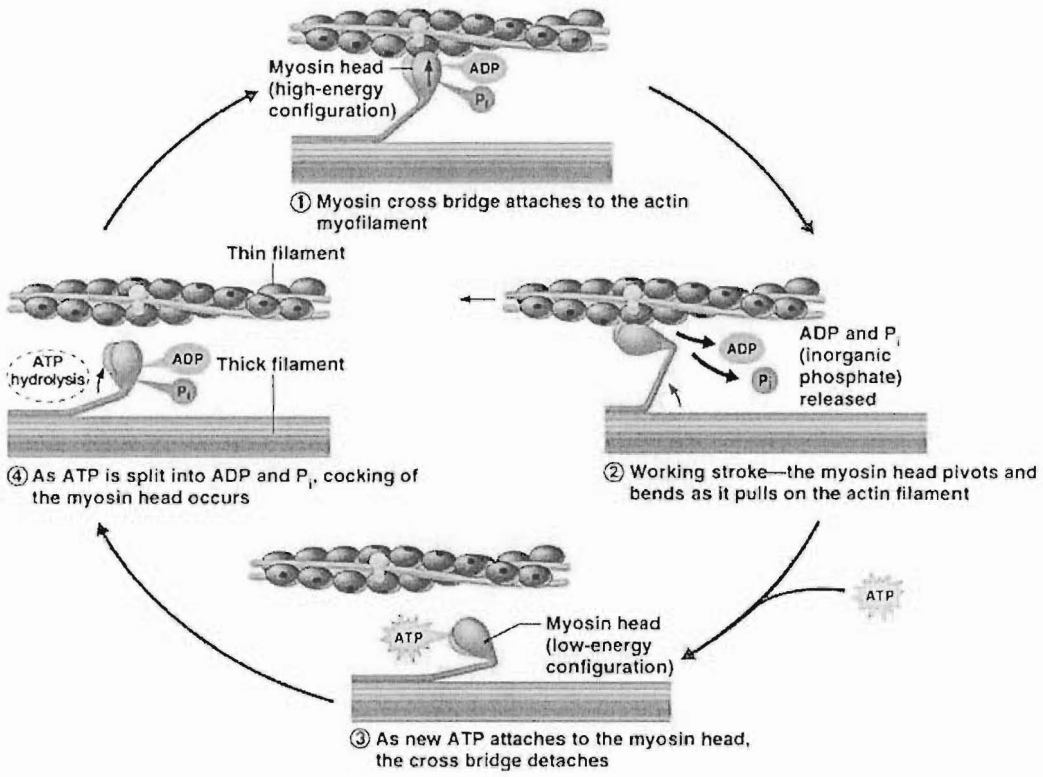

Figure 1.12 Smooth Muscle Contraction Dynamics

Specifically, there are myogenic and metabolic autoregulation mechanisms proposed. Both theories explain how blood flow is regulated to maintain a constant flow of nutrients to the cerebral mass. In reality, the autoregulation function most likely operates due to a combination of both myogenic and metabolic regulation.

The overall mechanism, in either case, results in modulating cerebral blood flow (CBF) as a result of mean arterial pressure (MAP) changes. As seen in the clinical data of Figure 1.13 [Dirnagl and Pulsinelli, 1990] the autoregulation function is only efficient between MAP ranges of approximately 70mmHg to 170mmHg. Since the data is so widely varying, this research uses the curve presented in Guyton and Hall [1996] shown in Figure 1.14, to approximate real behaviour.

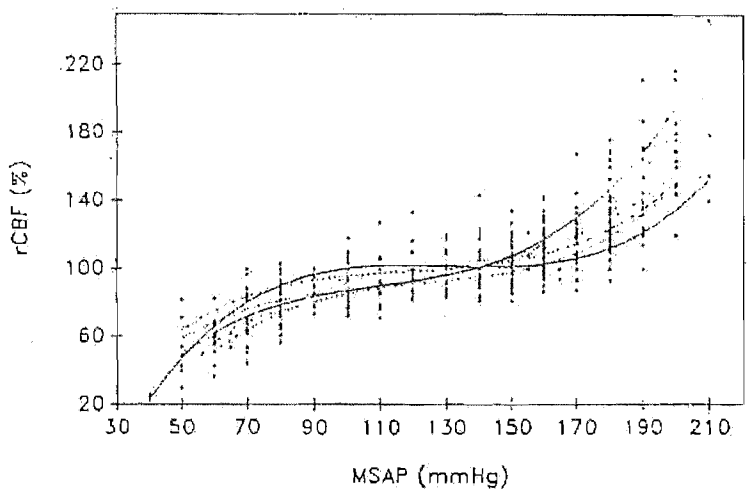

Figure 1.13 Clinical Data for Effect of MAP on Rate of Blood Flow

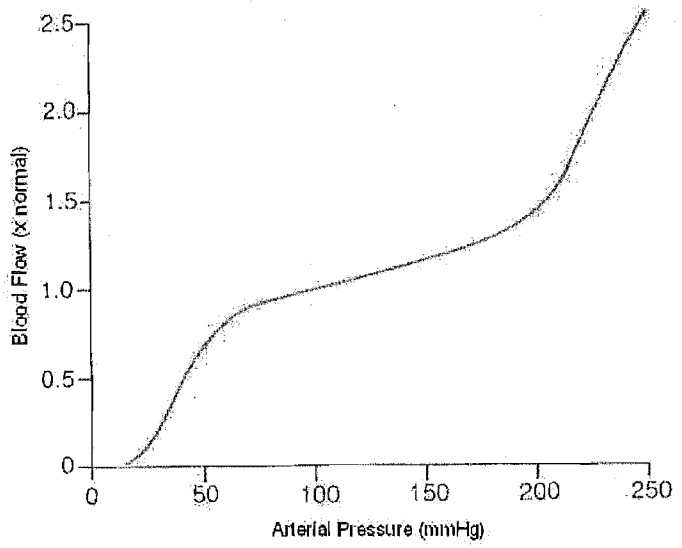

Figure 1.14 Blood Flow as a Function of Mean Arterial Pressure

1.5.1 Myogenic Autoregulation

Myogenic autoregulation is a means of maintaining a constant flow of nutrients to the brain despite changes in MAP. As MAP increases, the rate of flow of nutrients to the cerebral mass would tend to increase.

$$Q = \frac{\Delta P}{R} \tag{1.1}$$

where Q is the rate of blood flow through the vessel, ΔP is the change in pressure over the length of that vessel, and R is the resistance of the vessel to flow.

By myogenic autoregulation, an increased MAP causes a stretch in the blood vessel wall, triggering contraction of the smooth muscle cells surrounding the vessel, thus reducing the vessel diameter and increasing the vessel resistance.

$$R = \frac{8\mu l}{\pi r^2} \tag{1.2}$$

where μ is the dynamic viscosity of blood, l is the length of the vessel, and r is the radius of the vessel. This increase in resistance counteracts the increase in MAP, thus maintaining a constant flowrate, Q, through the vessel. The converse situation is also true, with vessels dilating when MAP decreases, to maintain constant flow.

There are several theories that explain the mechanisms that occur to couple a change in MAP with intracellular Ca^{2+} and therefore smooth muscle activation. Davis et al. [1992] developed a method to stretch single smooth muscle cells longitudinally, and record cell currents. It was found that cell stretch induced biphasic, sustained depolarisations of the membrane that were proportional to the degree of stretch. This discovery suggests the presence of a non-specific cation channel.

The stretch activated (SA) cation channel works as follows: inward current through the stretch-activated channel depolarises the cell membrane, which in turn activates voltage gated Ca^{2+} channels. Additionally, Ca^{2+} entering through the SA channel could trigger the release of Ca^{2+} from intracellular stores, or directly activate contractile machinery. Activation of ion channels resulting in increased intracellular Ca^{2+} initiates smooth muscle cell contraction, as explained in Section 1.3. In addition, mechanical deformation is known to generate various intracellular second messengers that trigger calcium release and protein kinase activation. Phospholipase-C (PL-C) activation leads to formation of IP_3, which triggers Ca^{2+} release from intracellular stores, initiating smooth muscle contraction. Hence, the mechanical stretch caused by an increase in MAP, induces smooth muscle contraction.

Katusic et al. [1993] found that removing the endothelium from canine basilar arterial rings prevented the active force development induced by stretch. It was then thought that vascular wall stretch or distension induces the release of an endothelium-derived constricting factor (EDCF) from endothelial cells (EC's), or decreases in the endogenous release of endothelium-derived relaxing factor (EDRF). Rubanyi et al. [1990] concluded that pressure-induced contraction of canine carotid arteries was mediated by depression of EDRF synthesis/release. A study by Lansman et al. [1987] used a patch clamping technique to demonstrate a cation channel in cultured ECs that is activated by pipette suction. Activation of the channel by stretch at a normal resting membrane potential would then depolarise the EC. This depolarisation could be conducted electrotonically to the smooth muscle layer within the vascular wall. Hence, as above, MAP is observed to induce smooth muscle contraction.

Cipolla et al. [2002] showed that an increase in MAP leads to an increase in wall tension which activates various signalling pathways. This activation stimulates actin polymerisation, increases formation of contractile stress fibres, and increases the vasomotive force production, resulting in an increased contraction. Therefore, although there is still much discussion among researchers as to specific physiological mechanisms, it is proved that arterial wall stretch induced by an increase in MAP, causes smooth muscle contraction. This contraction acts to decrease flow through the vessel, thus maintaining homeostasis.

1.5.2 Metabolic Autoregulation

Metabolic autoregulation is a means of maintaining a constant supply of nutrients to the brain despite changes in metabolism, blood oxygen content, or the rate of blood flow. Figure 1.15 [Guyton and Hall, 1996] shows that blood flow increases as arterial oxygen saturation falls, and Figure 1.16 [Guyton and Hall, 1996] shows that blood flow increases as the rate of metabolism increases.

The vasodilator theory suggests that when there is a decrease in oxygen delivery to the tissues, an increase in metabolism, or an increase in metabolite concentration (carbon dioxide (CO_2) and hydrogen ions (H^+)), there is a greater rate of formation of a vasodilator substance, which causes smooth muscles to dilate thus increasing the lumen diameter and therefore the amount of blood

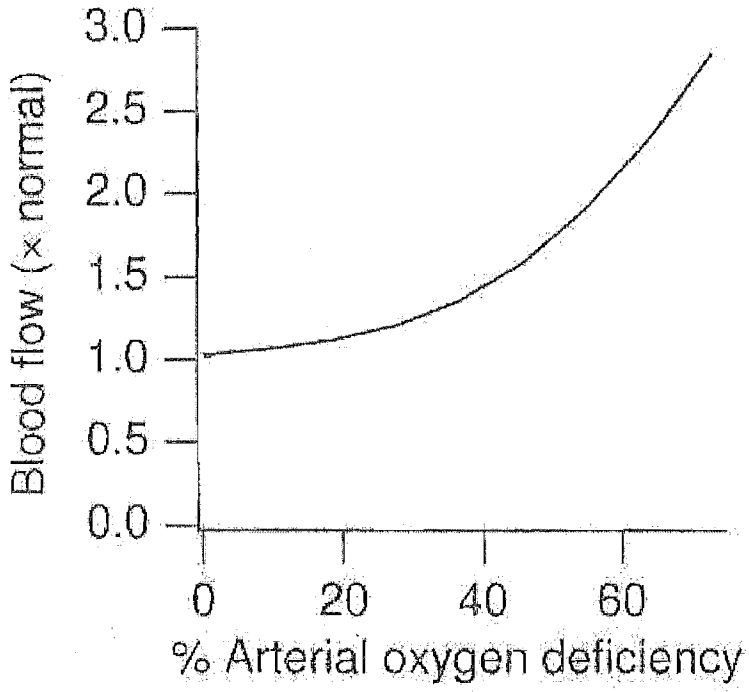

Figure 1.15 Effect of Arterial Oxygen Concentration on Blood Flow

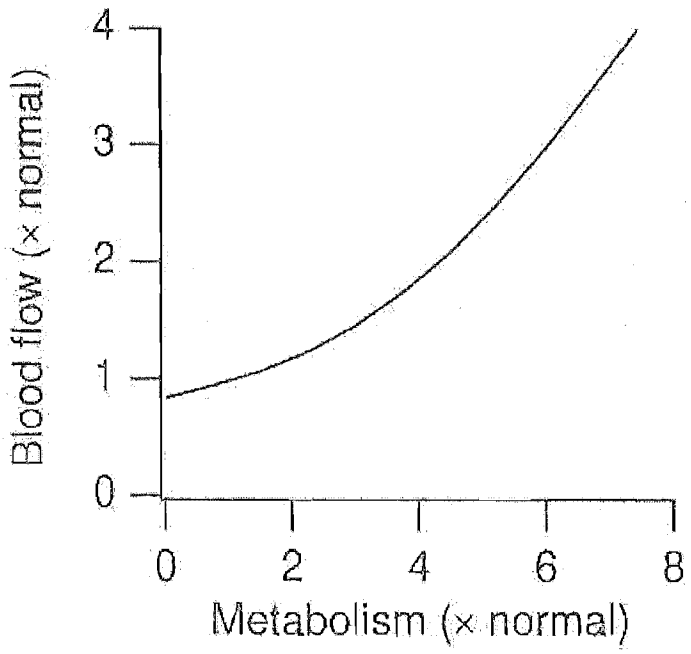

Figure 1.16 Effect of Metabolism on Blood Flow

flow. Many different vasodilator substances have been hypothesised, such as adenosine, hydrogen ions, CO_2, lactic acid, phosphate compounds, prostaglandins

and potassium ions (K^+), the most important of which appear to be adenosine and hydrogen ions [Guyton and Hall, 1996].

Adenosine is formed from AMP derived from hydrolysis of intracellular ATP and ADP. Adenosine formation increases during hypoxia and increased oxygen consumption, especially if the latter is accompanied by inadequate oxygen delivery. Adenosine causes relaxation in small arteries by blocking Ca^{2+} channels.

Carbon dioxide formation increases during states of increased oxidative metabolism. It readily diffuses from parenchymal cells where it is produced to the vascular smooth muscle of blood vessels where it causes vasodilation. An increase in CO_2 concentration is thought to increase cerebral blood flow by combining with water to form carbonic acid, which readily dissociates to form hydrogen ions.

When oxygen delivery to the tissue is insufficient, there is a decrease in the rate of oxidative phosphorylation, and an increase in anaerobic metabolism leading to an accumulation in lactic acid. Lactic acid dissociates to form hydrogen ions, and therefore has a vasodilatory effect, modulating vessel diameter, similar to CO_2.

It is generally assumed that the increase in hydrogen ions, which occurs due to an excess of CO_2 or an insufficient level of oxygen delivery to the tissues, exerts its vasodilating effect by competing for Na^+ and Ca^{2+} channels in the cell membrane [Siegel et al., 1977]. Peiper and Laven [1976] suggested that the decrease in intracellular pH reduces the rate of cycling of cross-bridges between actin and myosin, thus reducing cell contraction and promoting relaxation.

A second metabolic theory is the nutrient demand theory, which suggests that smooth muscle cells require oxygen (and other nutrients) to remain contracted. A decrease in the partial pressure of oxygen (PO_2) has been found to activate ATP-sensitive K^+ channels and Ca^{2+}-activated K^+ channels in the smooth muscle of cerebral arteries [Gebremedhin et al., 1994]. The resulting hyperpolarization limits Ca^{2+} influx through voltage sensitive L-type Ca^{2+} channels, to produce smooth muscle relaxation. In contrast, an increase in PO_2 acts to depolarize smooth muscle and causes vasoconstriction.

To summarise, the metabolic theory of autoregulation says that when there is a decrease in nutrient delivery to, or increase in nutrient usage by the tissues,

there is a increase in the production of vasodilator substances. These substances interfere with cation channels in the membrane to promote smooth muscle relaxation, thus decreasing vessel resistance to flow and maintaining an appropriate rate of blood flow to the tissues.

1.6 Physiological Considerations

When modelling the CoW, several input parameters, such as boundary pressures, are required, as well as clinical data detailing accepted temporal and steady state physiological responses to changes in arterial blood pressure.

1.6.1 Mean Arterial Pressure, Venous Pressure, and Intracranial Pressure

The cardiac cycle refers to events occurring from the beginning of one heartbeat to the beginning of the next. It consists of a period of relaxation, called *diastole*, during which the heart fills with blood, followed by a period of contraction, called *systole*. Figure 1.17 shows the variation of pressure over one heartbeat [Klabunde, 2004].

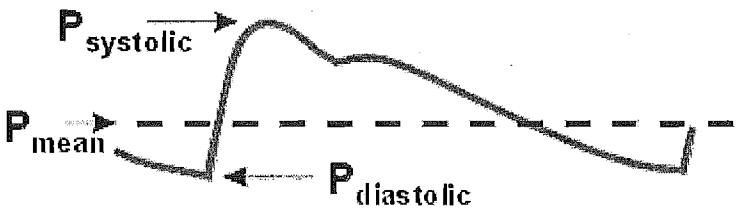

Figure 1.17 Pressure Variations over one Heartbeat

MAP is required as an input to the model as the pressure boundary condition upstream of the afferent vessels. It is determined by direct or indirect measurement of arterial pressure, but can be approximated by Equation 1.3:

$$MAP = P_{diastole} + \frac{1}{3}(P_{systole} - P_{diastole}) \tag{1.3}$$

For example, an arterial pressure of 130/85 refers to a systolic pressure of 130mmHg, and a diastolic pressure of 85, giving a MAP of 100mmHg, by Equation 1.3. Note that MAP is not simply an average of systolic and diastolic pressure, since during the course of one cardiac cycle, more time is spent in diastole than systole.

MAP is typically approximately 70-100mmHg, but this value varies with age. At birth, MAP is usually lower, at approximately 50-60mmHg, and by age 80, MAP has typically risen to approximately 120mmHg. The significant rise in MAP by age 60, is due largely to the increase in systolic pressure caused by hardening of the arteries, or atherosclerosis. Figure 1.18 illustrates MAP variations with age [Guyton and Hall, 1996].

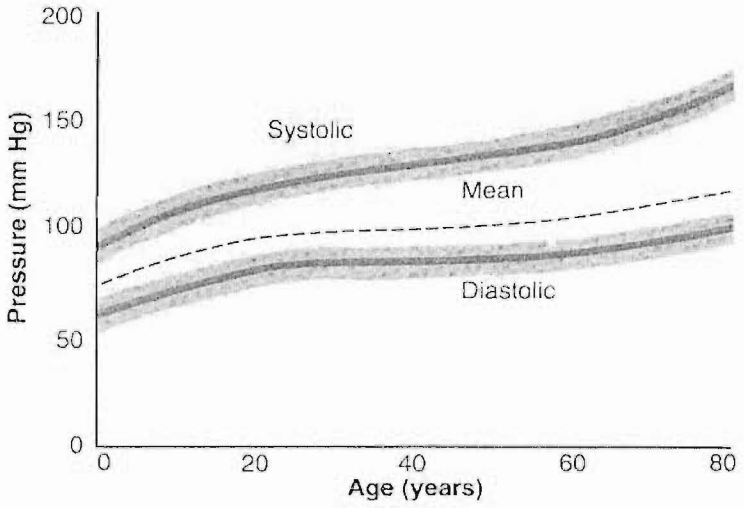

Figure 1.18 MAP Variation with Age

For the body to function properly, the heart needs to pump blood at a sufficient rate to maintain an adequate and continuous supply of oxygen and other nutrients to the brain and other vital organs. Cardiac output refers to the amount of blood pumped by the heart per minute. It is a function of the volume of blood pumped by the heart during each contraction (*stroke volume*), and the number of times the heart beats per minute, (*heart rate*). A normal resting cardiac output is approximately 5L/minute. Figure 1.19 shows how cardiac output varies with MAP [Guyton and Hall, 1996]. Note that at a MAP of 170mmHg, the cardiac output begins to drop off, and by 250mmHg, the cardiac output has fallen to zero.

Venous pressure, also called central venous pressure, is the boundary pressure used downstream of the efferent vessels. Normal values range from 2 to 7mmHg.

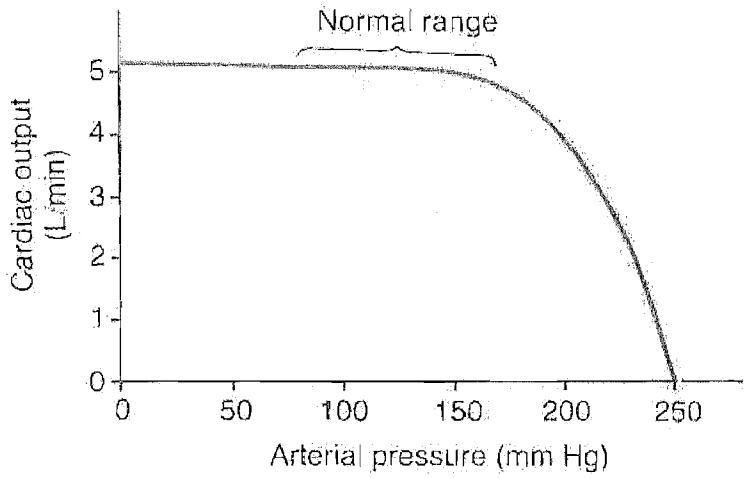

Figure 1.19 Normal Range of MAP

Intracranial pressure is the pressure within the rigid skull. It usually ranges between 5 and 13mmHg, but rises dramatically as intracranial volume increases due to injury.

1.6.2 Clinical Data

In addition to the steady state data of Figures 1.4 and 1.14, clinical data detailing the temporal response of efferent vessels to changes in input parameters is required. This data was obtained from thigh cuff experiments performed by Newell et al. [1994].

Newell et al. [1994] performed experiments in which a rapid step change in blood pressure was induced by inflating blood pressure cuffs around both thighs of a patient to 20mmHg above the patients systolic blood pressure for 3 minutes, and then deflating them. During the experiment, the percentage change and duration of the time-dependent velocity profiles were measured using Transcranial Doppler (TCD) recordings of the MCA. As observed in Figure 1.20, releasing cuff pressure resulted in a 20% drop in blood pressure, where the MCA took approximately 20 seconds to return to normal flow conditions.

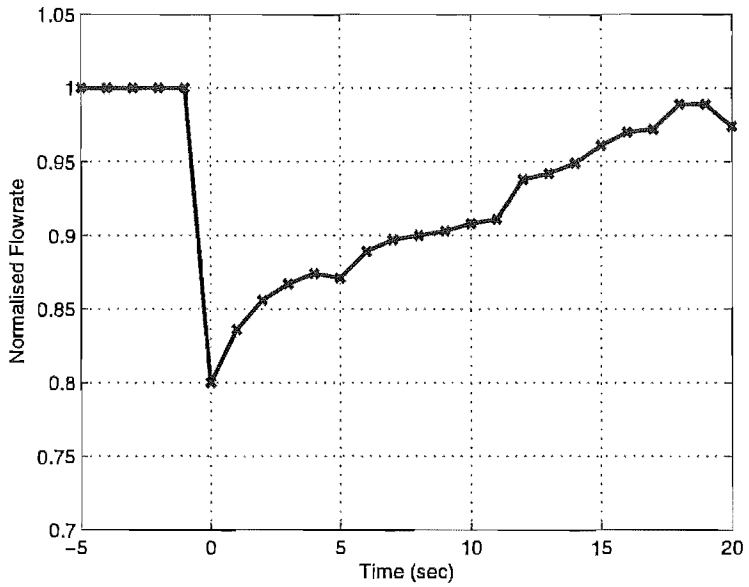

Figure 1.20 MCA Temporal Response to a Drop in MAP

1.7 Prior Modelling Research

Prior research has resulted in a variety of computational solutions. Hillen et al. [1988] created a simple model valid solely for the steady state. This model represented the peripheral resistances of the CoW as lumped blocks with a ratio of 6:3:4 for the ACA_2, MCA and PCA_2 resistances respectively. This ratio was chosen to inversely approximate the brain masses supplied by the corresponding arteries. However, the model has limited clinical application due to its lack of autoregulation mechanisms and dynamic response.

Cassot et al. [2000] developed a linear model of the CoW. This model neglected the effects of autoregulation of the cerebral vascular bed in maintaining optimal efferent flow conditions to the cerebral mass. Piechnik et al. [2002] concluded that this model made unrealistic assumptions of a passive resistor model of the downstream vascular bed, rather than including dynamic autoregulation as seen clinically.

Ferrandez et al. [2002] created a 2-dimensional model using CFD. This model incorporates autoregulation by modelling the arterioles, downstream of the efferent arteries, as porous blocks with variable resistors governed by a PI feedback controller. However, the dynamic resistance model is not accurate because

changes are made to the resistance even when the correct reference flowrate has been obtained. This approach also requires a significant amount of computational effort due to the higher dimensional CFD employed, resulting in a long solution time that is not suitable for a simple, diagnostic tool.

Lodi and Ursino [1999] model autoregulation by dynamically controlling the compliance of chambers based on volume changes. However, the model does not solve for equilibrium between flow and autoregulation changes. Hence, it ignores the transient dynamics that the current research focuses on. Hudetz et al. [1982] incorporate autoregulation with integral control based on pressures and flowrates, similar to the current research. This model also focuses on the long-term steady state response, and therefore does not seek to capture the crucial dynamics as to how that state is achieved.

Chapter 2

Basic Model

To perfectly model the full distribution of blood throughout the cerebral mass, every vessel out to the smallest arterioles would be incorporated in the model. The CoW supplies a large network of interconnected vessels, which branch from the circulus efferent vessels. In this study, a basic model of the CoW is created in which the vessels supplying cerebral tissue have been reduced to the six main efferent vessels labelled in Figure 1.2, due to lack of physiological data, as well as for geometric simplicity and reduced computation. The model is shown schematically in Figure 2.1, and includes efferent and afferent vessels and a sign convention for flow.

2.1 Fluid Dynamics

Due to the relatively small diameters of the blood vessels comprising the CoW and the velocity of blood flowing through them, the Reynolds numbers are approximately 200. As this value is well below the transition to turbulence, laminar flow may be assumed throughout the model. While it is generally accepted that blood is a non-Newtonian fluid, models that incorporate its behaviour, such as the Carreau-Yasuda model or the Casson model [Collins, 1961], predict an infinite shear viscosity that is approached above shear rates of $100s^{-1}$. Initial simulations indicated that shear rates throughout the CoW are well above this $100s^{-1}$ threshold, so a Newtonian fluid can be assumed.

The CoW can be modelled as a one-dimensional structure with laminar, viscous and incompressible flow [Moorhead et al., 2004]. Per the assumption made

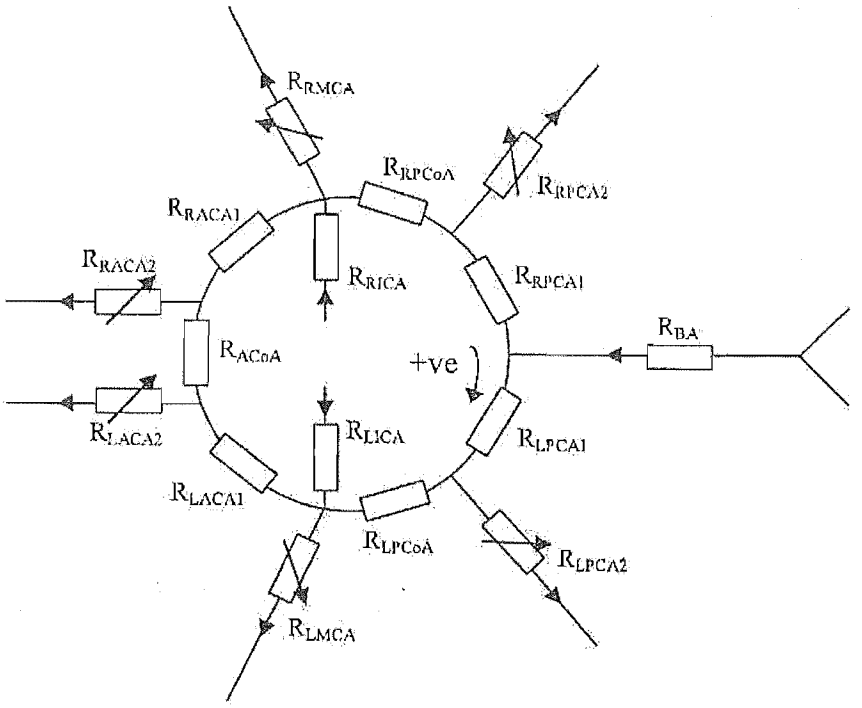

Figure 2.1 Schematic of the Basic CoW Model

by Ferrandez et al. [2002] and Moorhead et al. [2004], the flow in any arterial element is assumed to be Newtonian and axi-symmetric. Therefore, it can be modelled by the Poiseuille Equation for flow in a tube, where the flowrate, Q, is proportional to the pressure gradient along the vessel and the inverse of the vessel resistance to blood flow, as shown in Equation 1.1, and repeated here for clarity.

$$Q = \frac{\Delta P}{R} \tag{2.1}$$

In addition, resistance is a function of vessel length, radius and the dynamic viscosity of blood, as repeated here.

$$R = \frac{8\mu l}{\pi r^2} \tag{2.2}$$

Equations 2.1 and 2.2 are applied to each arterial element and combined

with equations for the conservation of mass at each vessel junction into a matrix equation:

$$\underline{A}\tilde{x} = \tilde{b} \tag{2.3}$$

where $\underline{A}$ is a matrix containing resistances for each arterial element, $\tilde{x}$ is a state vector containing flowrates through those arteries and nodal pressures at the end of the arteries such that $\tilde{x}(t) = \{q_1...q_{16}, P_1...P_7\}$, and $\tilde{b}$ is a vector containing arterial and venous boundary pressures. Note that if the afferent pressures in $\tilde{b}$, which drive the system, change dynamically, a time-varying system is created. The state vector $\tilde{x}$, then also becomes time-dependent, as the solution varies with each deviation in afferent pressure.

$$\underline{A}(\tilde{x}(t))\tilde{x}(t) = \tilde{b}(t) \tag{2.4}$$

The system in Equation 2.4 more accurately represents typical behaviour, as these afferent mean arterial input pressures are not typically constant.

2.2 Physiological Parameters

Data for arterial length and radius is found from known physiological data [Ferrandez et al., 2002] representing an average for the human population, and is shown in Table 2.1. The resulting resistances are calculated using Equation 2.2.

In Figure 2.1, afferent and circulus arteries are shown with constant resistances, as it is assumed that smooth muscle cell induced constriction and dilation of the artery walls does not occur to a significant degree in large, relatively rigid cerebral arteries [Fung, 1990]. Since the model uses the Poiseuille flow approximation, where the resistance of an arterial segment is inversely proportional to the fourth power of the radius of the vessel, small changes in the radius of small peripheral arteries causes the greatest changes in resistance, and thus flowrate. Efferent arteries are consequently shown with time-varying resistances that represent the combined resistance to flow of the smaller arteries and arteri-

Table 2.1 Reference Artery Lengths, Radii and Resistances

Vessel	Radius mm	Length mm	Resistance Nsm^{-5}
BA	2	30	17
ICA	2	250	139
PCA_1	1.5	20	35
PCoA	0.5	20	2852
ACA_1	1.25	20	73
ACoA	0.5	5	71
PCA_2*	1.5	70	5300
MCA*	1.75	70	4000
ACA_2*	1.25	50	8000

* The peripheral resistances have been added to the efferent vessels

oles downstream of the CoW.

These time-varying efferent resistors are capable of variations in resistance of between 5% and 195% of the 'normal' resistance [van der Zwan et al., 1993; Newell et al., 1994; Ferrandez et al., 2002; Gao et al., 1998; Mancia and Mark, 1983]. This variation corresponds to changes in arterial radius of up to 40% using Equation 2.2. Hence, upper and lower bounds can be used in these time-varying resistances, R, such that:

$$(1 - 0.95)R_{ref} \leq R \leq (1 + 0.95)R_{ref} \tag{2.5}$$

The combination of vessel resistance and time varying peripheral resistance in the ACA_2, MCA, and PCA_2 is set to approximate the ratio 6:3:4 in the 'normal' flow state [Hillen et al., 1986]. This ratio between the total resistances of each of the efferent vessels is approximately inversely proportional to the cerebral mass each efferent vessel supplies.

2.3 Autoregulation Model

The autoregulation process can be described by a relatively simple feedback control system, where the control input, $u(t)$, is a function of the flowrate error, e from a reference value, at that timestep. The error triggers the autoregulation

response modelled by the controller, causing a change in resistance that results in a modified flowrate. This process is shown schematically in Figure 2.2, where the plant is the time-varying flow and the controller is the time-varying resistor, and is defined:

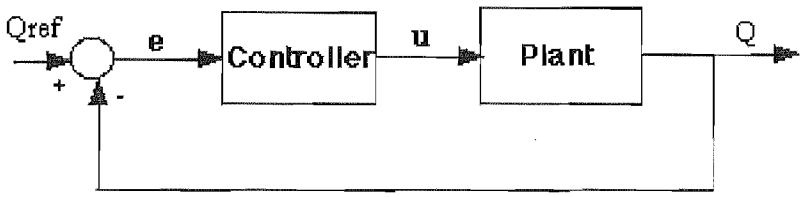

Figure 2.2 PID Controller

$$u(t) = K_p\, e + K_i \int e + K_d \frac{de}{dt} \tag{2.6}$$

where K_p, K_i and K_d represent proportional, integral and derivative control gains respectively, and are found by matching the time-dependent velocity profiles obtained from the experiments of Newell et al. [1994], described previously.

The various components of the PID controller operate on various aspects of the error. For example, consider the error in flowrate after a step change in pressure has been induced. As time passes, an error profile develops, representing the difference between the actual flowrate and the desired flowrate. The proportional gain acts on the absolute magnitude of that error; the derivative gain acts on the slope of the error profile thus reacting most strongly to *changes* in flowrate; and the integral gain acts on the cumulative running sum of the absolute error. When these three control components are combined in the right proportions, a flowrate profile can be created which matches the clinical data presented in Figure 1.20.

The dynamic behaviour of the peripheral resistance modelling the autoregulation process of the time-varying resistance can be described by a simple first order system:

$$\dot{R} = \frac{1}{\tau}(R_{ref} - R) + \frac{1}{\tau}u(t) \tag{2.7}$$

where τ is the time constant of the autoregulatory response, R and R_{ref} are the actual and reference resistances of the efferent artery respectively, and $u(t)$ is a control input defined by Equation 2.6. It should be noted that this model differs from that of Ferrandez et al. [2002], where in their case the dynamics were described:

$$\dot{R} = \frac{1}{\tau}(R) + \frac{1}{\tau}u(t) \tag{2.8}$$

However the Ferrandez equation would continue to alter the control resistance even though the flow is at the correct level. In contrast the present model provides for this, since when $Q = Q_{ref}$ and $u(t) = 0$, $R = R_{ref}$, as expected, which was not the case with the model of Ferrandez et al.

2.4 Numerical Solution

Initially, the reference resistances and flowrates are calculated using the steady state, 'normal' balanced configuration case. The given geometry may include circulus vessel omissions or string-like vessels. The solution method for the basic model is summarised in Figure 2.3.

At each time step, inner iterations between Equations 2.4 and 2.7 are used to find the equilibrium solution for the combined system of equations at that time step. To determine the efferent flowrates at each time-step, the control input for each vessel is calculated as in Equation 2.6 using the flowrate obtained from the previous solution of Equation 2.4 and comparing it to the reference flowrate. Efferent resistances are then recalculated thus giving an improved estimate of those resistance values. This value is then inspected to ensure it is within physiological limitations as set by Equation 2.5, and saturated if it exceeds the imposed limits. Using the improved resistance values, the flowrates for the current time-step can be recalculated. This process of obtaining improved resistance values and calculating corresponding flowrates is continued until the resistance and flowrates do not change between iterations, representing simultaneous satisfaction of Equations 2.4 and 2.7, indicating equilibrium for that time step in ensured. Each time step is solved this way until the final time is reached. Note that when the efferent

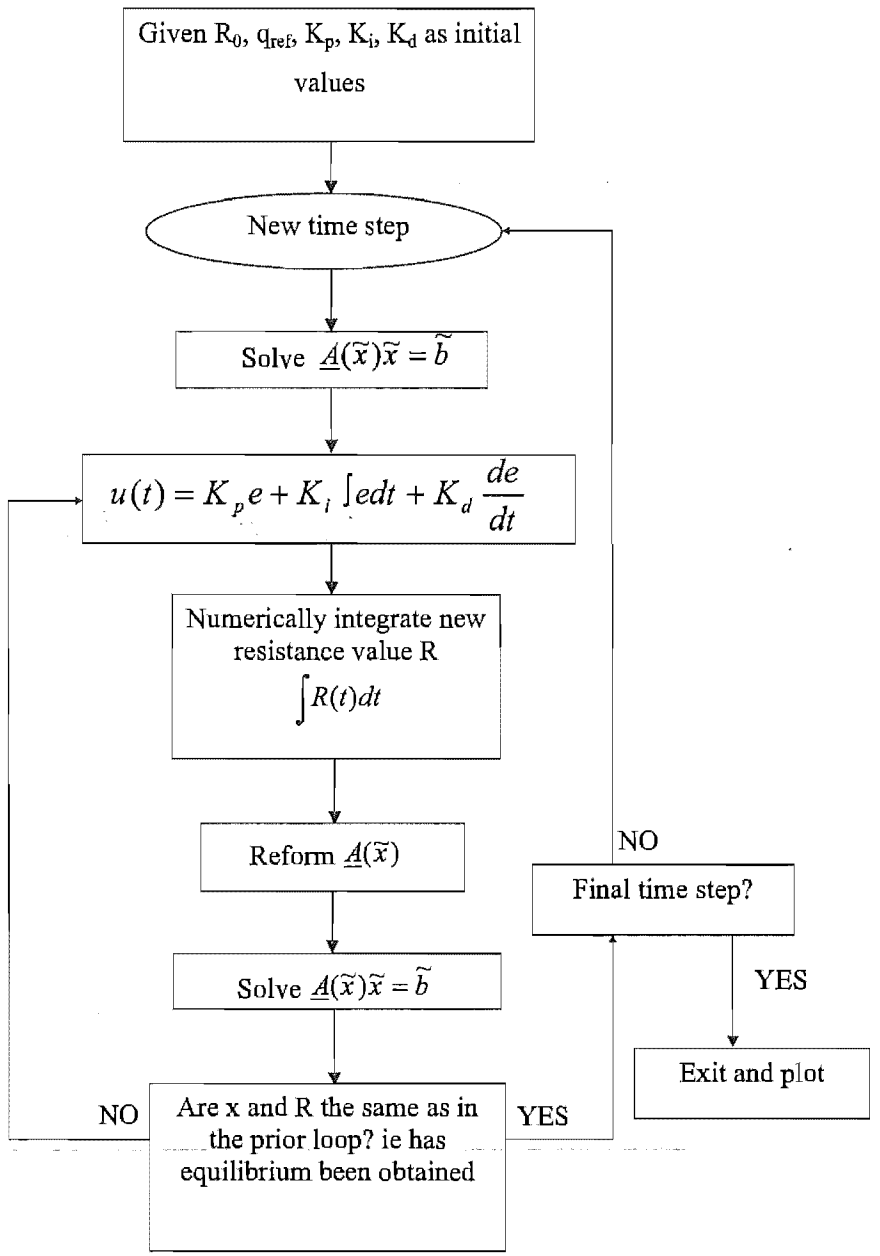

Figure 2.3 Schematic of the Basic CoW Model

flowrate is at its reference value, the control input tends to zero and a steady state response is achieved until the next perturbation of the afferent pressures.

The overall system model allows for many variations in circle geometry. To

simulate an absent vessel, the resistance of that vessel is set to a large value ensuring negligible flow through that segment. Similarly, simulation of string-like vessels can be performed by setting resistances to as much as sixteen times their original value to account for their narrower vessel radius. An increase in resistance of sixteen times is equivalent to a decrease in artery radius of 50% [Lodder et al., 1996].

Alterations of the afferent pressure time-dependent profiles are also easily simulated. These simulations have been used to model rapid pressure drops caused by a stenosis and/or surgical procedures such as a carotid endarterectomy, gradual pressure drops due to blood loss, and sinusoidal variations in pressure. Therefore, several combinations of clinically verified geometries and situations can be modelled using far less computational effort than similar models using higher dimensional CFD. The result is a potentially significant input to clinical decision-making.

2.5 Methods and Case Studies

The complete CoW is modelled with venous pressures of 4mmHg and an arterial pressure drop from 93mmHg to 73mmHg in the RICA using the specific arterial resistances from Ferrandez et al. [2000]. Due to lack of data for the response of the ACA_2 and the PCA_2, these arteries were assumed to have a similar, approximately 20 second, response time.

The time constant is taken to be $\tau = 3$ seconds [Ferrandez et al., 2000], and the proportional, integral, and derivative gains were of the order 0.1, 10, and 0.01, respectively. All reference values for flow are calculated using the balanced configuration of the CoW under 'normal' flow conditions. Figure 2.4 illustrates the 20% pressure drop and 20 second response time of the RMCA that was matched to the physiological data of Newell et al. [1994].

Simulations are carried out for the balanced configuration and each case where a single circulus vessel is omitted. In all cases, where only one vessel in the CoW was removed, the system is able to obtain the reference efferent flowrates upon simulation of a surgical procedure causing a temporal pressure drop of approximately 20% in the RICA. To reach the reference flowrates the flow is redirected

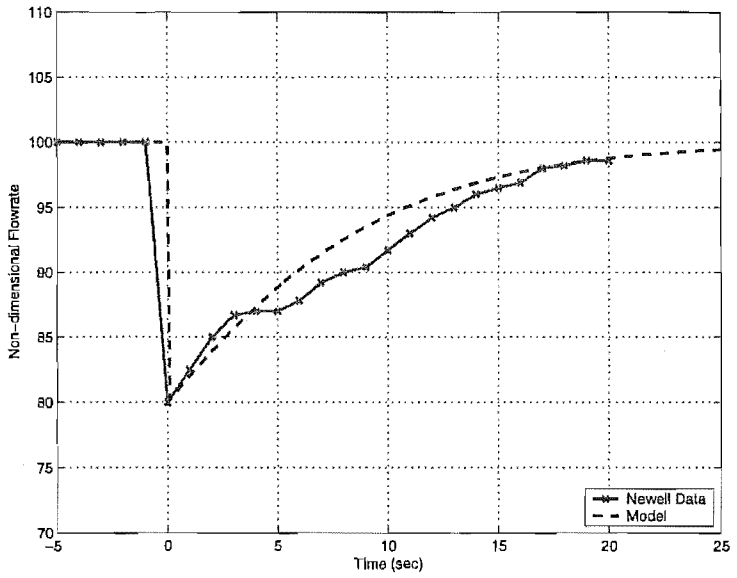

Figure 2.4 Comparison of Basic Model MCA Response to 20% Pressure Drop in RICA with Newell Data

as a result of independently changing resistance in the vascular bed of each efferent artery - the autoregulation function. In each case, these resistances remained within the 95% variation limit. Throughout the simulations, good correlation between this work and the work of Ferrandez et al. [2000] was observed, as shown in Table 2.2.

Table 2.2 Comparison of Results with Ferrandez

	% drop in RMCA flow after 20% pressure drop in RICA	
	Ferrandez	Basic Model
Balanced Configuration	18	19
Absent $LPCA_1$	Not simulated	19
Absent LPCoA	18	19
Absent $LACA_1$	18	20
Absent ACoA	18	20
Absent $RACA_1$	20	21
Absent RPCoA	20	19
Absent $RPCA_1$	Not simulated	19

The results displayed in the remainder of this research use a bar chart format. Resistances and flowrates have been normalised to the LICA in the balanced configuration case, such that the flowrates through each vessel are shown in a comparative, rather than an absolute sense. The x-axis follows the circle clockwise starting at the BA, with flowrates through afferent and circulus arteries shown on the left, and flowrates through efferent arteries on the right. Bars below the

x-axis indicate that flow is in the opposite direction to that assumed by the sign convention in Figure 2.1. Schematic figures show flow directions after the pressure drop, where solid arrows indicate a change in direction of flow from the steady state, pre-pressure drop case, and open arrows indicate that the flow direction has not changed.

2.6 Results and Discussion

2.6.1 Balanced Configuration

The 'normal' flow balanced configuration case with resistance values taken from physiological data [Ferrandez et al., 2000] are used as a baseline for analysing results. This case shows zero flowrate through the ACoA and equal flowrates across each of the left and right sections of the circle. The symmetry in the flow is due to the symmetrical nature of the resistances in the circle and the incoming flows. The high PCoA resistances (160 times higher than ICA) dominate the flow pattern reducing the flow to a minimal amount in these elements, and result in the BA supplying the efferent PCA's, and the ICA's supplying the efferent MCA's and ACA's. These results are in good agreement with the accepted physiological response [Newell et al., 1994].

A stenosis or occlusion in the RICA is simulated by a pressure drop from 93 to 73 mmHg, and the resulting normalised flowrates are shown in Figure 2.5. When compared to the normal flow case, the asymptotic flowrate after stenosis/occlusion dropped in the RICA with increased flow in the LICA and, to a lower extent, in the BA, to supply the efferent flowrate required. The flowrate in the LICA increased by 60% while the flowrate in the BA increased by 23%. The pressure change in the RICA also causes a change in the direction of flow through the RPCoA and $RACA_1$ resulting in a clockwise flow throughout the anterior regions of the circle, delivering flow from the LICA through the ACoA to the starved RMCA. Lastly, note that all efferent arteries recover reference flowrates after the pressure drop.

The step change in pressure from 93mmHg to 73mmHg in the RICA, results in significant changes in the flowrate and the pressure differential in the RMCA.

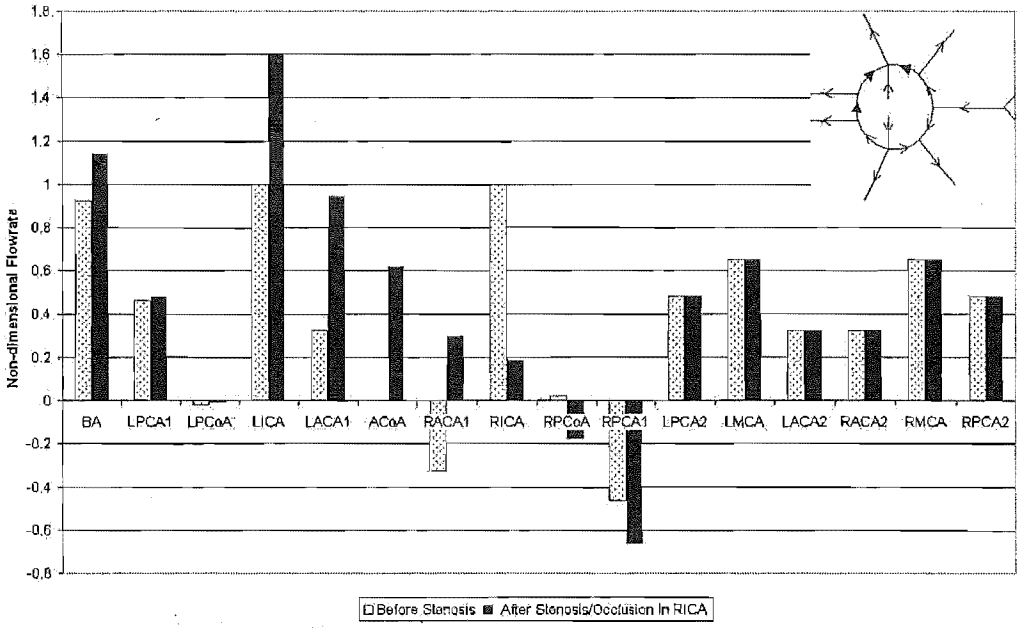

Figure 2.5 Normalised Flowrate through the CoW before and after Pressure Drop, in the Balanced Configuration Case

This result is expected because the RMCA is the first of the efferent vessels to be supplied by the RICA. More specifically, the flowrate dropped 18% and took approximately 20 seconds to return to its original value, as seen in Figure 2.6. The $RACA_2$ also had a significant change in flowrate of approximately 17% when the pressure drop occurs.

2.6.2 Absent ACoA

An absent or restricted ACoA is a common physiological condition [Alpers et al., 1959]. Under 'normal' conditions an absent ACoA poses no threat to brain function as shown by the flowrate of zero in the ACoA in the balanced configuration under 'normal' flow conditions. The complication of the omission of the ACoA is only significant under flow conditions such as a stenosis or occlusion of an afferent artery, where other arteries are absent, or where there is asymmetry in the circle.

Unlike the balanced case, the simulated stenosis/occlusion in the RICA in the absent ACoA case results in little change from the 'normal' flow case. The reason for the low change is that the RICA is now required, in conjunction with

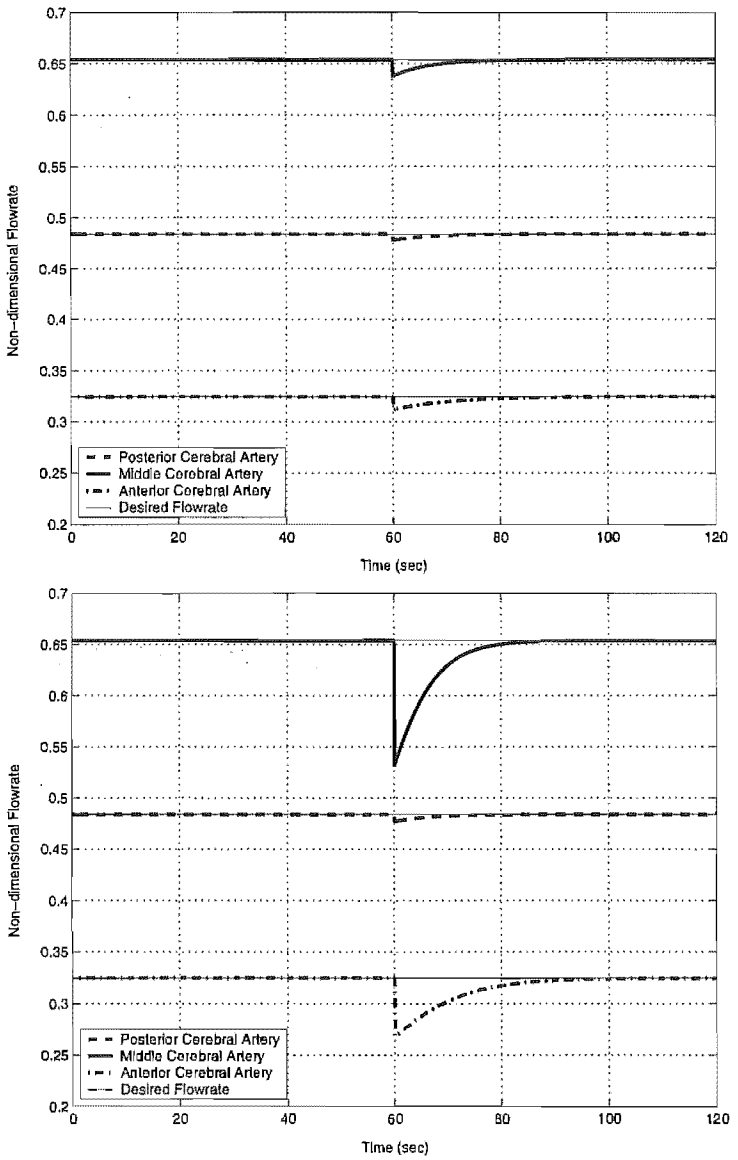

Figure 2.6 Efferent Arterial Response to Stenosis of the RICA, in the Balanced Configuration Case. Right Efferent Response (*top*); Left Efferent Response (*bottom*)

the BA, to supply all of the efferent vessels on the right side ($RACA_2$, $RPCA_2$, and RMCA). More specifically, the flow from the LICA cannot be rerouted though the ACoA, and the RPCoA assists only minimally in meeting the right efferent demands because of its very high resistance. Flow in the left portion of the brain is virtually unaffected by the stenosis/occlusion in the RICA. The flow through both ACA_2's are exactly the same as the 'normal' flow case, showing the anterior section of the brain to be unaffected by this pressure drop.

After a stenosis/occlusion, the flow through the $RPCA_1$ was higher than through the $LPCA_1$ (symmetrical in the steady state case). This observation is a result of compensation for the pressure drop in the RICA by the BA, which delivers blood at a higher rate through the $RPCA_1$ and RPCoA to supply the RMCA. It can thus be seen that the communicating arteries play a more significant role when the geometry is unbalanced in this fashion, as seen in the flowrate changes of Figure 2.7.

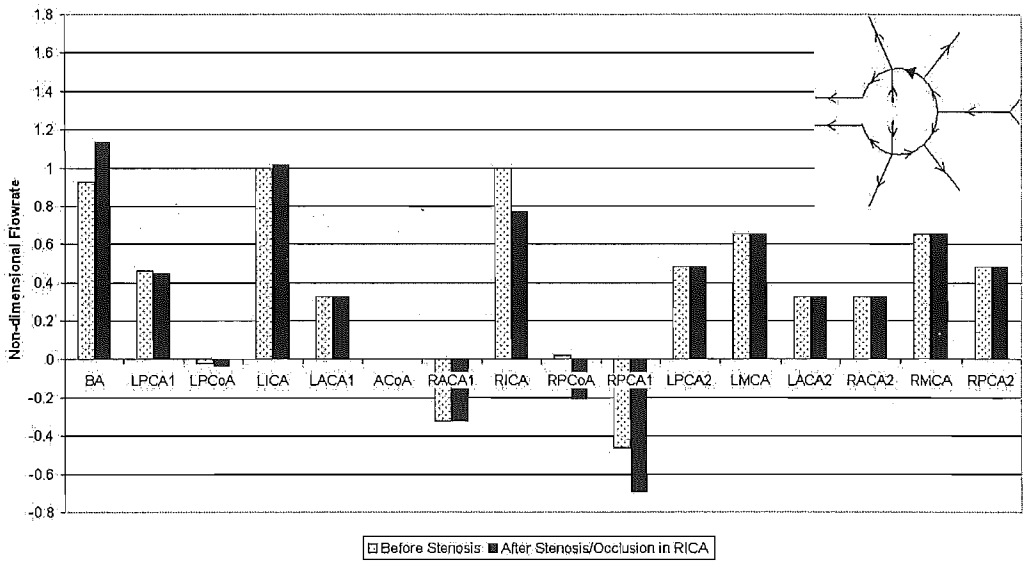

Figure 2.7 Normalised Flowrate through the CoW before and after Pressure Drop - Absent ACoA

2.6.3 Absent ACA_1

This case was very similar to an absent ACoA response with very little difference between the 'normal flow' and stenosis/occlusion situations, especially in the left portion of the brain. The only significant response immediately after the RICA stenosis/occlusion was in the adjoining RMCA, where the flowrate dropped 21% before returning to its asymptotic value. In both the absent $RACA_1$ and $LACA_1$ 'normal' flow cases, the flowrate through the ACoA is much higher than any other case and over five times higher than the next highest ACoA flowrate.

From all the cases where the geometry of the CoW is missing a single ves-

sel, the $LACA_1$ case showed the largest immediate drop in flowrate through the $RACA_2$ when the pressure drop was simulated, with a drop of 21%. Flow through both ACA_2's was also significantly affected, but returns to the desired flowrate. Also of interest, was that the stenosis/occlusion had absolutely no effect on the flow in the LMCA. The absence of the $LACA_1$ and the high resistance in the LPCoA essentially isolates the LMCA. Of the flow supplied by the LICA, only 5% is diverted away from the LMCA through the LPCoA to this artery.

2.6.4 Absent PCoA

Missing either of the PCoA's has little effect in the 'normal flow' case due to their high resistances. An absent LPCoA has less effect than an absent RPCoA in the right side stenosis/occlusion case, as it is the furthest of the circle vessels from the pressure drop. Hence, the response is very similar to the balanced case with the only significant difference being the flow through the ACoA. An absent RPCoA does not increase the BA flow, as in the balanced case and absent LPCoA case, as an increased BA flow cannot compensate for the reduced RICA flow with the RPCoA vessel missing. Immediately following the stenosis/occlusion, the RMCA is most affected in both the absent left and right PCoA cases, as it is in the balanced case, with the PCA_2's the least affected.

2.6.5 Absent PCA_1

With the $RPCA_1$ missing, the BA cannot supply the $RPCA_2$ as it would in all other cases. Consequently, the flowrate through the BA is over 45% less than the other omitted artery cases already discussed in both the 'normal flow' and stenosis/occlusion situations. There is a much larger response to the RICA pressure drop in the $RPCA_2$ than in any other case with a reduction of 31% before autoregulation returns it to the asymptotic flow state. There was no change in the flowrate through the RPCoA between 'normal flow' and stenosis/occlusion cases, however the flowrate was over 20 times higher than any of the other absentee cases.

As in the absent $RPCA_1$ case, the BA flowrate is much lower in the absent

$LPCA_1$ case than in any other cases. The flowrate demanded from the LICA was highest in this absentee situation. The stenosis/occlusion case demanded a 44% increase in flowrate through the LICA from the 'normal' flow case. The LICA supplies the efferent LMCA and $LPCA_2$, and the BA supplies the $RPCA_2$ and RMCA. In the 'normal' flow case the $LACA_2$ is supplied by the LICA, and supply from the LICA also reaches the $RACA_2$. With the reduction in flow in the RICA due to the pressure drop, the $RACA_2$ and even the RMCA need to obtain a part of their demand from the LICA.

2.6.6 Stroke Risk Case

All the prior cases with a single omitted artery were able to maintain the reference flowrate in all the efferent arteries, showing the robustness of the CoW system as a whole. This case represents a realistic situation of increased stroke risk where the autoregulation process cannot keep the efferent flowrates at the desired level. A situation is modelled in which there are decreases in radius of the LICA and RICA of 50% and 40% respectively, and the $LPCA_1$ is missing [Lodder et al., 1996]. This case represents a situation where the individual would be hypertensive to maintain proper flow to the cerebral mass, and the present model detected this. When a pressure drop is simulated representing the effects of a stenosis, the $LPCA_2$ cannot return to its reference flow value representing a potential stroke, as shown in Figures 2.8 and 2.9.

This failure to return to reference flowrate occurs because the resistance of the $LPCA_2$ cannot be further decreased since the maximum radius of the artery has been reached as a result of the autoregulation process model. The final flowrate is 8.5% lower than desired leading to reduced perfusion and higher stroke risk for this type of input. Note that the other efferent arteries all return to their asymptotic values.

2.7 Summary

A 1D CFD model of the CoW has been created to study autoregulation of cerebral blood flow for clinical events, such as occlusions or stenosis in afferent arteries,

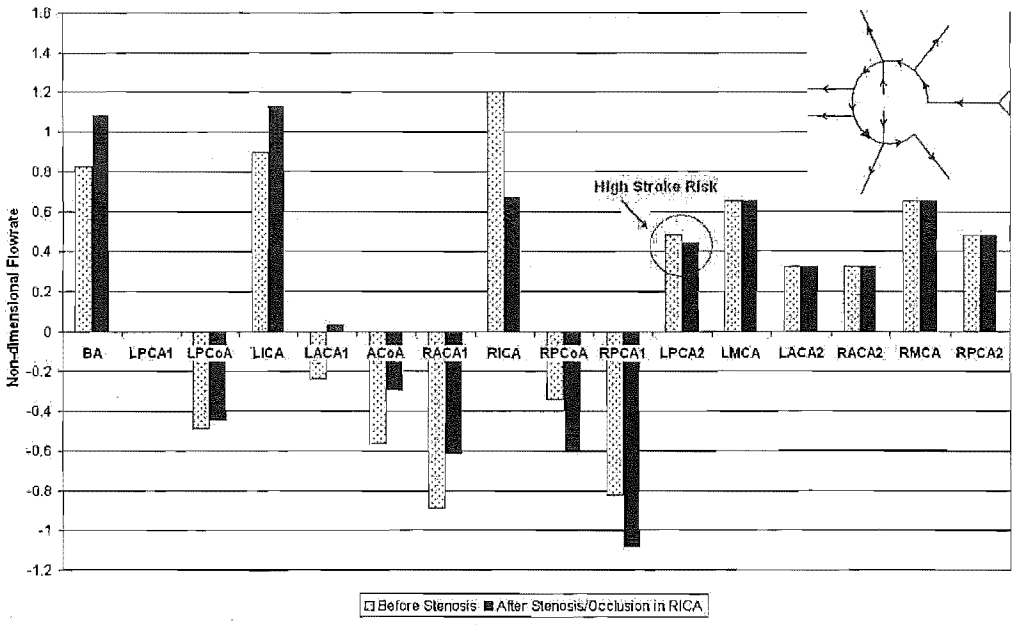

Figure 2.8 Normalised Flowrate through the CoW before and after Pressure Drop - Stroke Risk Case

absent or string-like circle vessels, or arterial infarctions. The model is a significant advancement over pre-existing models in its incorporation of inner iterations at each solution timestep to find the equilibrium state, within physiological limitations. The addition of the inner iterations recognises the non-linearity of the cerebral circulatory system and the autoregulation process in particular. Time varying resistance accounts for vasodilation and vasoconstriction of the efferent arteries such that a constant flowrate to the cerebral territories can be obtained after occlusion/stenosis in any afferent artery.

Results show good correlation with prior results using higher dimensional CFD [Ferrandez et al., 2000] with the same physiological data [Newell et al., 1994]. The time-dependent velocity profiles in the MCA were matched to give a 20% decrease in flowrate, followed by approximately 20 seconds to return to steady state conditions in response to a stenosis/occlusion in the RICA. The solution for the CoW arterial system is obtained in a far shorter time period using this time-varying resistance model than with higher dimensional CFD methods, and requires significantly less computational effort while retaining a high level of accuracy.

The model created has simulated the omission of any single circulus artery

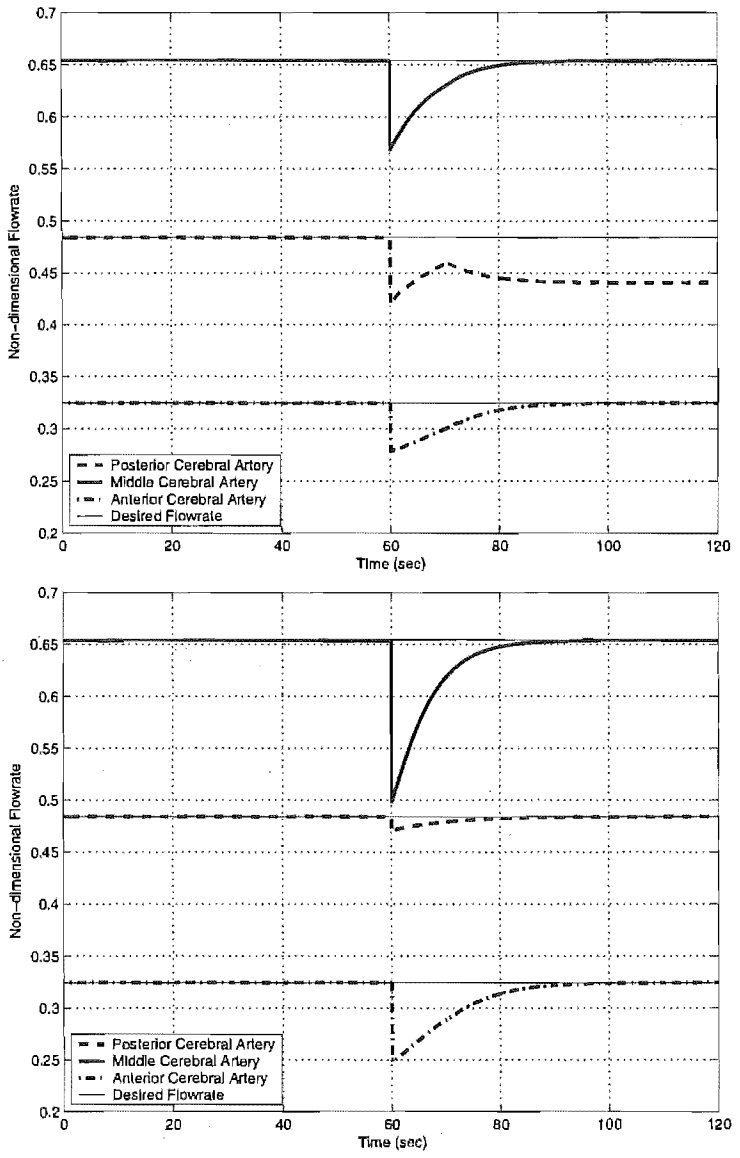

Figure 2.9 Efferent Arterial Response to Stenosis of the RICA, in the Balanced Configuration Case. Right Efferent Response (*top*); Left Efferent Response (*bottom*)

and found that no such omission leads to failure in reaching the required efferent flowrates for a RICA occlusion. This result highlights the known robustness of the CoW system in supplying the cerebral mass territories. A physiologically realistic case in which there is failure to reach the reference efferent flowrates was developed and simulated. While this particular case is not especially probable, it highlights the effectiveness of this model as a tool for determining potential outcomes of surgical or other therapies.

The model requires more physiologically accurate models, including metabolic

and/or myogenic models of autoregulation. In addition, the resistance limits require further examination, to determine the physical limits of autoregulation. Lastly, more clinical verification is required, which will also involve the modelling of a greater variety of potential CoW geometries, including more combinations of absent arteries.

Chapter 3

Validation of 1D Model

A 3D CFD model of autoregulation was created by S.M. Moore and is used to validate the 1D model [Moore et al., 2004]. The geometry required to develop the 1D and 3D computational domain was based on a MRA of an individual's cerebro-vasculature that is shown in Figure 1.1. It is observed that some of the arteries comprising the circle such as the PCoAs and the ACoA are not visible in the scan. As the scan implicitly detects blood flow through the arterial network, there was little or no blood flow through these arteries. These arteries therefore, were artificially placed into the circle at physiologically appropriate locations with the diameters obtained from Hillen et al. [1986]. Figure 3.1 shows a schematic CoW used for both 1D and 3D models. Note that it is different than the model in Figure 2.1 with additional small efferent vessels.

3.1 3D Model

The computational domain for the 3D model was created by forming a mesh from the CAD model based on the MRA scan of Figure 1.1. The mesh was comprised of a total of approximately 351 000 tetrahedral elements, ranging in size from 1mm near the ICA and BA inlets, to 0.05mm in the ACoA. The efferent arteries continually branch and decrease in size downstream of the circle to the capillary bed. Because of the inability of the MRA scans to pick up this detail and the computing power it would require to solve the fluid flow equations for the whole arterial bed, attempting to model the entire capillary bed throughout the brain is not currently possible.

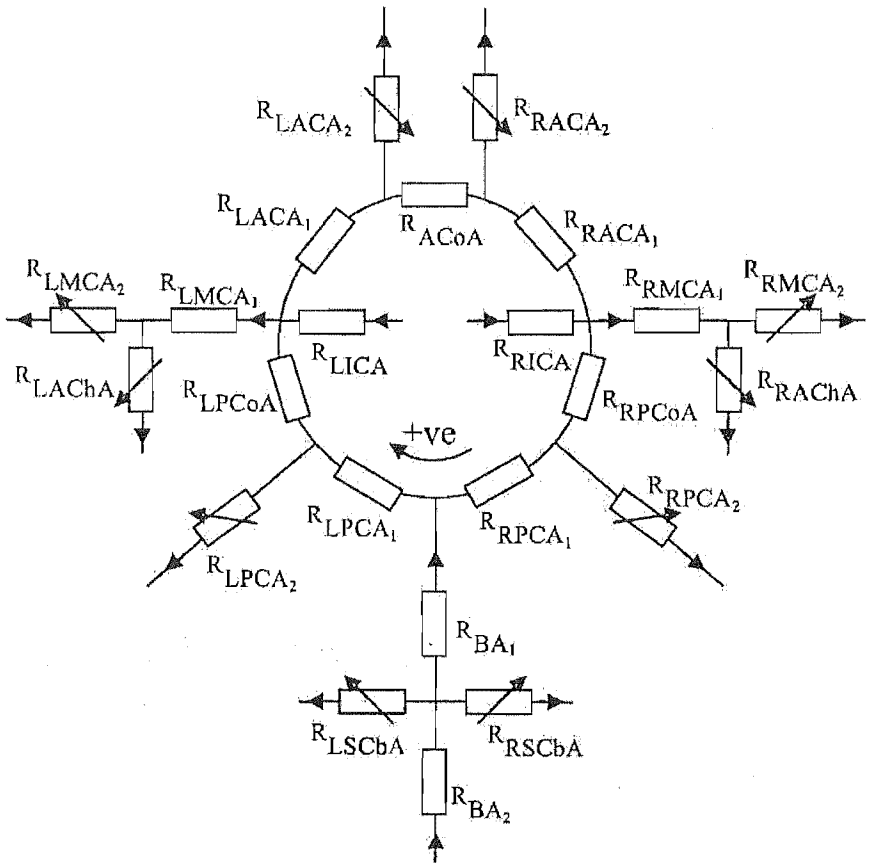

Figure 3.1 CoW Schematic

Ferrandez et al. [2002] developed a 2D CFD model of the circle of Willis with the novel approach of using a porous block to represent the effects of the capillary bed. This approach was used here with the major efferent arteries terminated a short distance downstream of the circle with a porous block. The porous block represents a resistance to the flow in much the same way as the capillary bed, so realistic representations of the flow can be obtained. The resulting solid model is shown in Figure 3.2.

3.2 3D Fluid Model

Blood flow through the CoW is unsteady, incompressible and viscous. Therefore, with the assumptions of laminar blood flow in the CoW the governing equations,

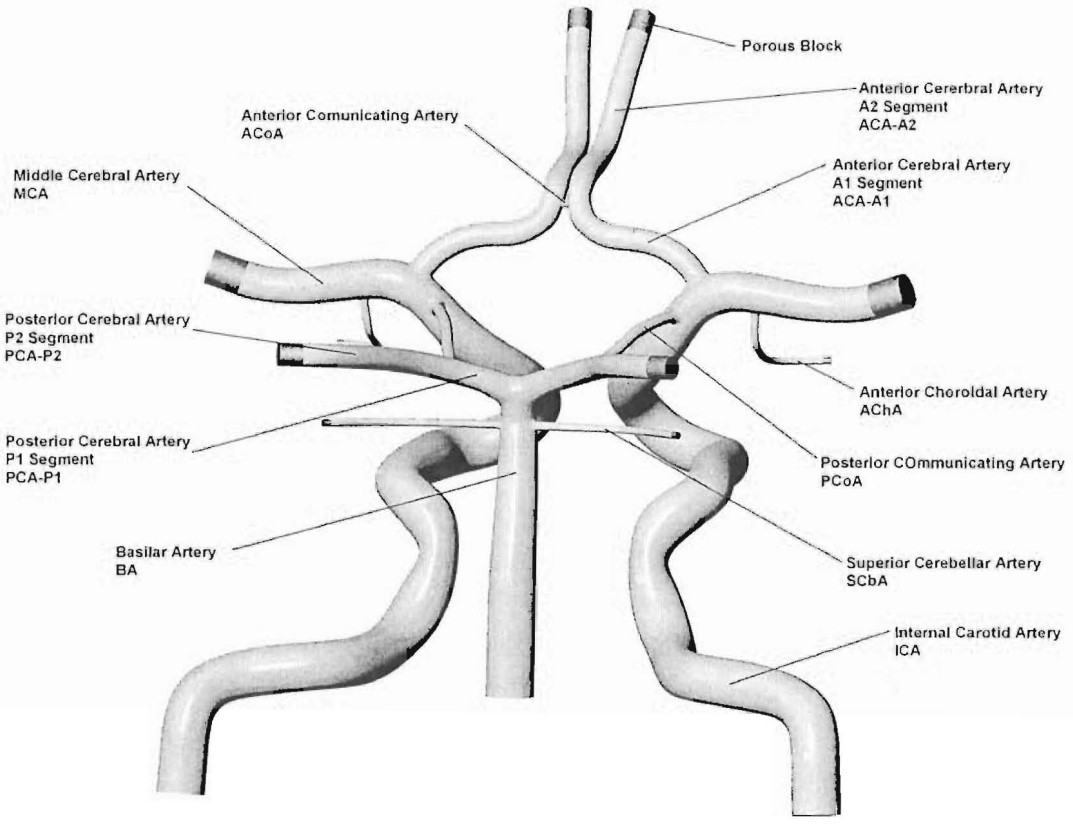

Figure 3.2 3D CFD CoW Solid Model

expressed in integral, conservation form, are the continuity equation:

$$\int_V \frac{\partial V}{\partial t} dV + \oint \rho \mathbf{u} d\mathbf{A} = 0 \tag{3.1}$$

and the momentum conservation equation:

$$\int_V \frac{\partial V \mathbf{u}}{\partial t} dV + \oint \rho \mathbf{u}\mathbf{u} \cdot d\mathbf{A} = -\oint p\underline{\mathbf{I}} d\mathbf{A} + \oint \overline{\overline{\sigma}} \cdot d\mathbf{A} + \int_V \mathbf{F} dV \tag{3.2}$$

where u is the 3D velocity vector, $\mathbf{I}$ is the identity matrix, $\overline{\overline{\sigma}}$, is the shear stress tensor and $\mathbf{F}$ represents a momentum source vector, used in the implementation

of the autoregulation mechanism. To solve this system of equations the finite volume method was chosen, which is a control volume based technique to convert the governing equations into an algebraic form that can be solved numerically [Collins, 1961].

The peripheral resistances of the porous blocks are incorporated into the CFD model by defining them in the same manner as a porous zone, requiring a permeability k as one of the input parameters. To relate the permeability to the peripheral resistance, R, a modified form of Darcy's law is used [Collins, 1961]:

$$k = \frac{\pi r^2}{R\mu L} \tag{3.3}$$

where r is the radius of the porous block and L is its length. To connect to the efferent arteries the radii of the porous blocks were matched to the radii of the arteries and the lengths of the blocks were arbitrarily chosen to be equal to twice the radius. Darcy's Law is associated with the volume-averaged properties of a flow, but it can be incorporated into the Navier Stokes equations, producing the Brinkman Equation [Collins, 1961]:

$$\left(\frac{\mu}{k}\right) \mathbf{u} = -\nabla p + \overline{\mu}\ \nabla^2 \mathbf{u} \tag{3.4}$$

where $\overline{\mu}$ is an effective viscosity. In the simulations performed, the two terms on the right hand side of Equation 3.4 are already incorporated into the momentum equation, however the implementation of the term on the left hand side can be incorporated by introducing it as a momentum source vector. Assuming an isotropic permeability of the porous block, the momentum equation is then modified with an additional momentum source to represent the effects of the porous block.

$$\int_V \frac{\partial \rho \mathbf{u}}{\partial t} dV + \oint \rho \mathbf{u}\mathbf{u} \cdot d\mathbf{A} = -\oint p\, \underline{\mathbf{I}}\, d\mathbf{A} + \oint \overline{\overline{\sigma}} \cdot d\mathbf{A} + \int_V \left(\frac{\mu}{k}\right) \mathbf{u}\, dV \tag{3.5}$$

3.3 Solution Method

Figure 3.3 compares the solution algorithms for the 1D and 3D models. It is clear that despite using the same equations to model the autoregulation mechanism, the algorithms differ in terms of how the equations are implemented in their discretised form. The major difference is that the 1D model uses the flow error for the current time step as the control input, whereas the 3D model uses the flow error from the previous timestep.

In using the flow error for the current time step a number of inner iterations need to be performed with the 1D model to ensure equilibrium between the flow solution and the peripheral resistances for every time step. To determine the efferent flowrates at each time-step, the control input for each vessel is calculated using the flowrate obtained from the previous inner iteration solution at that timestep, or the previous timestep in the case of the first inner iteration. Efferent resistances are then recalculated using the control input, thus giving an improved estimate of the resistance value using Equation 2.7. This value is then inspected to ensure it is within physiological limitations of 95% and saturated if it exceeds the limits. Using the improved resistance values, the flowrates for the current time-step can be recalculated. This process of obtaining improved resistance values and calculating corresponding flowrates is continued until the resistance and flowrates do not change between iterations, representing convergence. Note that when the efferent flowrate is at its reference value, the control input tends to zero and a steady state response is achieved until the next perturbation of the afferent pressures, as expected.

With the 3D model this inner iteration is not possible. Even though the solution of the Navier Stokes equations is an iterative procedure, altering the peripheral resistances and thus the momentum source vector for every iteration would effectively mean that a different system of equations would be solved each iteration. This approach would lead to divergence and therefore the flow error from the previous time step is used in the implementation of the autoregulation mechanism for the 3D model. Note that if the time steps are much smaller than the autoregulation time constant, τ, there should be little difference in the 3D model.

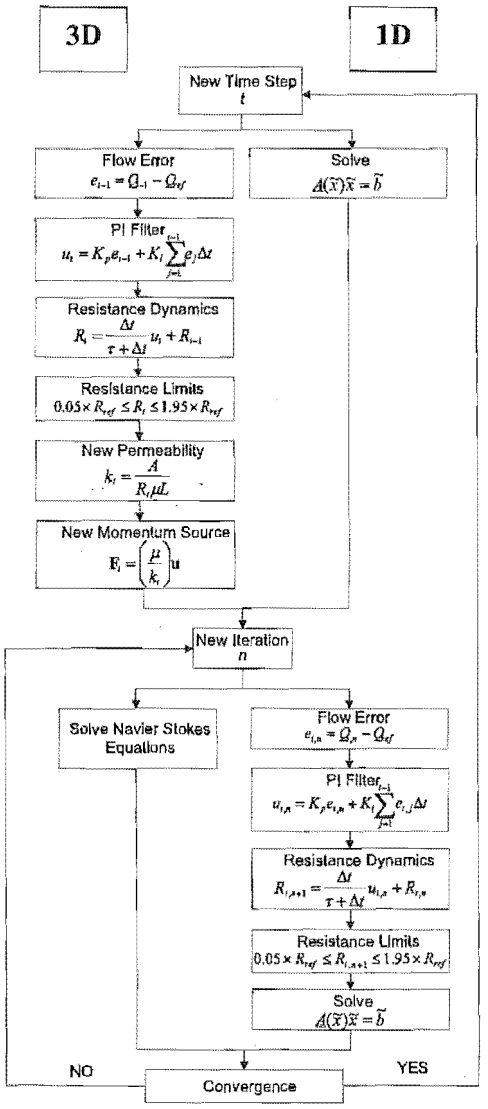

Figure 3.3 Comparison of 1D and 3D solution methods

3.4 Reference Fluxes and Resistances

The autoregulation mechanism responds to perturbations of the efferent flows from their reference value. To obtain realistic models of the flow, the evaluation

of these reference fluxes is critically important. Once the reference fluxes are determined, the reference resistances follow directly, as for each efferent artery its reference resistance, R_{ref}, is defined:

$$R_{ref} = \frac{P_{ref} - P_v}{Q_{ref}} \tag{3.6}$$

where P_v is the venous pressure boundary condition and P_{ref} is the pressure on the upstream side of the porous block once the reference flowrate has been reached. Hillen et al. [1986] suggested a total influx into the circle of Willis of 12.5 cm^3/sec, and a peripheral resistance ratio of 6:3:4 for the ACA, MCA and PCA's respectively. For the smaller AChA and SCbA arteries, less is known and Hillen did not include these arteries. Therefore, a resistance ratio of 75:75 is defined, which produces similar pressures on the upstream side of the porous blocks as the other major efferent arteries and contributes less than 5% of the total efferent flux.

Evaluation of the steady state reference fluxes requires an iterative procedure that was performed on the 3D model. This process involved altering the permeability of the porous blocks with afferent pressures of 100mmHg and efferent pressures of 10mmHg until a total flux of 12.5 cm^3/sec was achieved with the resistance ratio of 6:3:4:75:75. These reference fluxes were then used in the 1D model.

However, there is a disagreement in the two models as to the resistances required to produce the reference fluxes, because the 3D model predicts a greater loss in blood pressure travelling through the vessels comprising the circle than the 1D model. As a result, the pressure on the upstream side of the porous block is lower in the 3D model, resulting in a lower reference resistance once the reference flux is obtained. Using the 3D reference resistances in the 1D model results in efferent fluxes greater than the reference. Hence, to obtain the unique solution set of reference resistances for the 1D model, an iterative procedure was carried out where efferent reference resistances were altered until the 3D efferent fluxes were obtained.

Previously, 1D efferent resistances were obtained from Hillen [1988], and were 8, 4, and 5.3 $GNcms^{-5}$ respectively for the ACA_2, MCA and PCA_2. As previously

mentioned, Hillen et al. [1986, 1988] did not study the AChA or SCbA, so to obtain the 12.5cm3s^{-1} flux and include these extra vessels, resistance values were altered from the 3D model, as previously described. Table 3.1 shows the reference fluxes and resistances that are used throughout the rest of this study. Note that the difference in resistance is relatively minor for the major efferent vessels.

Table 3.1 Reference Flowrates and Resistances used in CFD Simulations

Artery	Reference Flux cm^3s^{-1}	1D Reference Resistance $x10^{11}$ $Ncms^{-5}$	3D Reference Resistance $x10^{11}$ $Ncms^{-5}$
ACA_2	1.277	8.428	7.37
MCA	2.798	3.942	3.66
PCA_2	1.993	5.458	4.89
$AChA_2$	0.090	106.123	92.73
$SCbA_2$	0.092	105.120	95.64

3.5 Results and Discussion

The 1D and 3D models were subjected to a 20 mmHg pressure drop in the RICA to observe the transient response for an ideal configuration. A configuration with an absent ipsilateral ACA_1 was also simulated to compare models for a common pathological condition of CoW geometry.

3.5.1 Balanced Configuration

Figure 3.4 illustrates the changes in efferent flux for both the ipsilateral and contralateral sides of the CoW. It is clear that the efferent fluxes for both 1D and 3D are virtually identical. Some important features of the pressure drop in the RICA are that it only has the effect of reducing the efferent flowrate in the anterior ipsilateral arteries it supplies, with the remaining vessels virtually undisturbed from their reference values.

Differences between the models become more apparent when the peripheral resistances and the flux distribution throughout the circle are considered. Figure 3.5 shows the peripheral resistances of the ipsilateral arteries. As only the anterior ipsilateral arteries experience a reduced flowrate, it is only these arteries where

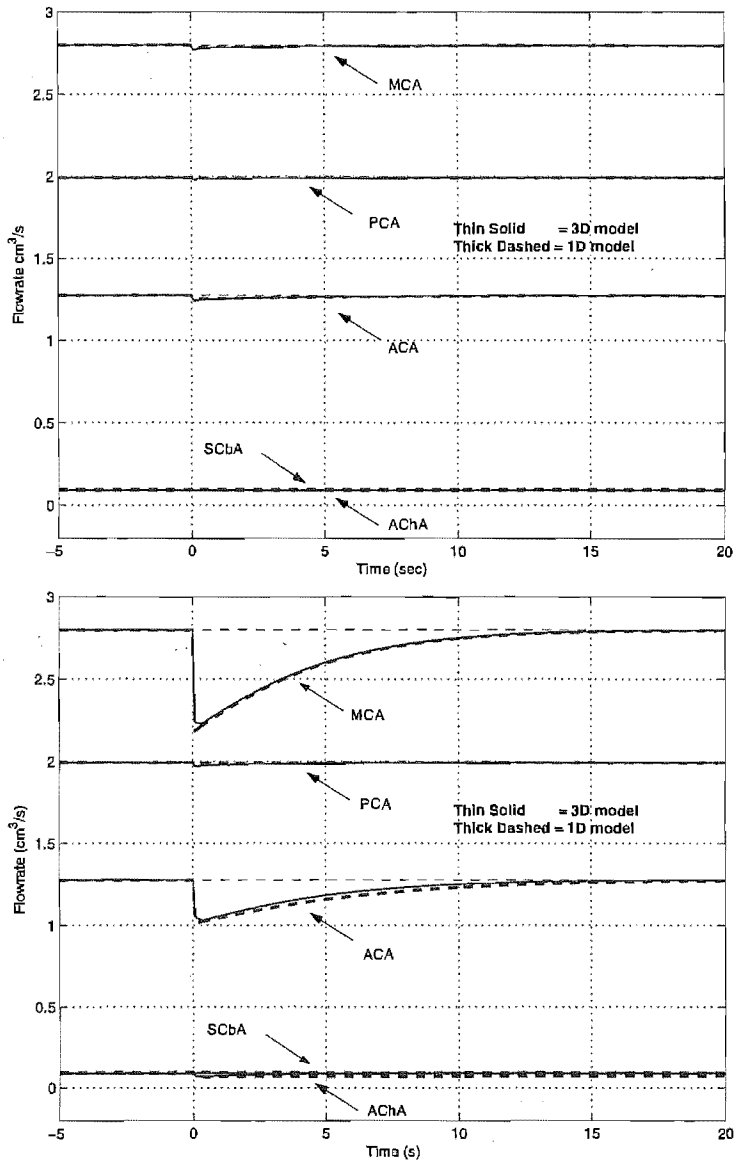

Figure 3.4 Efferent Arterial Response to 20mmHg Pressure Drop in RICA in the Balanced Configuration. Right Efferent Response (*top*); Left Efferent Response (*bottom*)

the peripheral resistance is altered, as expected. In this case, the results do not coincide because, as previously mentioned, the reference resistances differ between models to produce the same reference fluxes.

It can be observed in Figure 3.5 that the peripheral resistance of the 3D model changes by a proportionally larger amount than the 1D model to restore the efferent fluxes to their reference value. The explanation for this result is most easily understood when considering the flux distribution throughout the circle

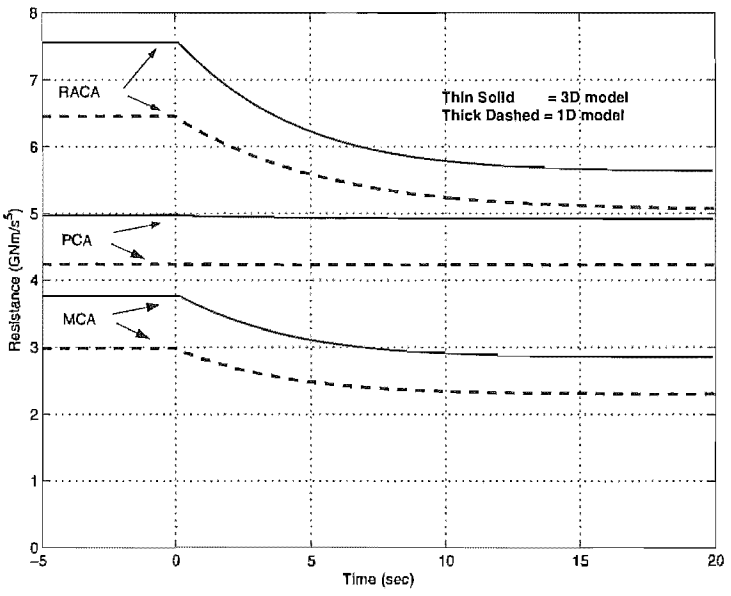

Figure 3.5 Ipsilateral Resistance for 20mmHg Pressure Drop in RICA in the Balanced Configuration

in response to the pressure drop. Figure 3.6 illustrates the fluxes throughout the arteries comprising the circle at the completion of the simulation. While the efferent fluxes are virtually identical between both models, fluxes within the circle are clearly different. With the 1D model there is a greater amount of blood flow re-routed through the communicating arteries to supply the anterior ipsilateral arteries starved of blood supply by the pressure drop. This result is evident in the larger flowrates through the contralateral ICA, ACA_1 and ACoA as blood is re-routed from the contralateral side of the circle through the ACoA. Additionally, the flowrates through the BA and the ipsilateral PCA_1 and PCoA are larger as more blood is re-routed through the posterior region of the circle through the ipsilateral PCoA.

The 3D model, in contrast, restores the starved anterior ipsilateral arteries by drawing more afferent blood supply through the ipsilateral ICA, which is the ICA with the pressure drop imposed on it. It appears that despite using the same lengths and diameters for both models to describe the geometry of the CoW, there is a significant difference between the models. More specifically, the 3D model experiences much larger losses in blood pressure through the communicating arteries than the 1D model, which assumes Poiseuille flow through these arterial segments.

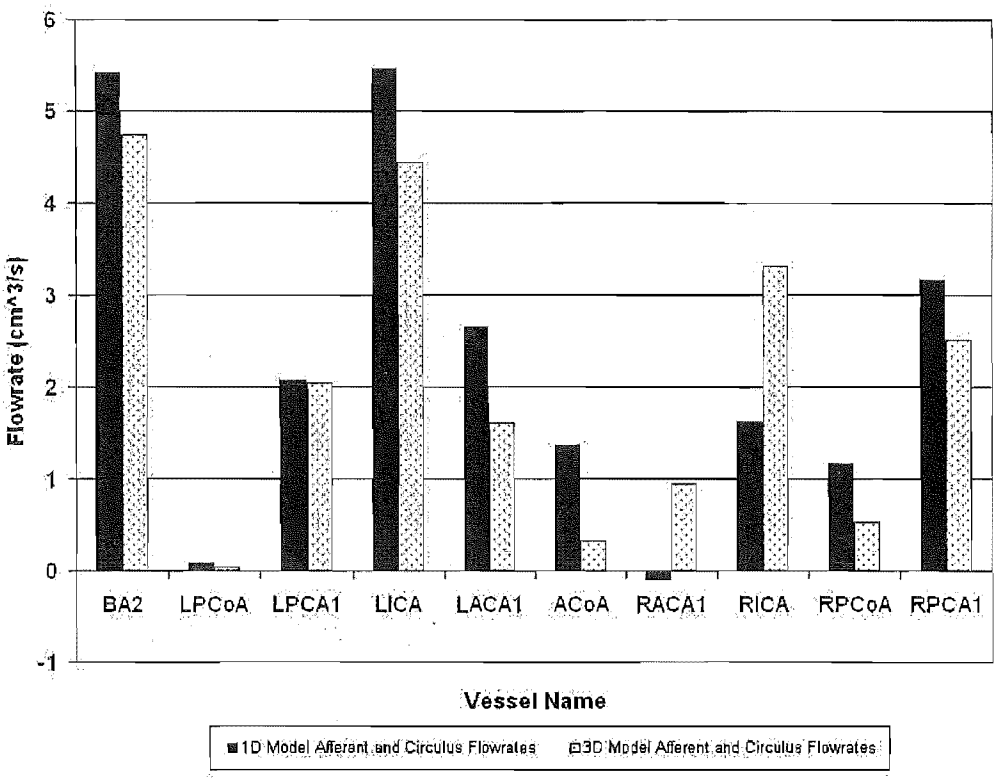

Figure 3.6 Comparison of Flowrates for 1D and 3D Models in the Balanced Configuration

Possible reasons for this discrepancy arise from the assumptions made for Poiseuille flow, some of which include axi-symmetric flow, implying a straight blood vessel, and also a fully developed velocity profile. In reality, these assumptions may not hold for smaller circulus vessels such as the ACoA, resulting in an underestimated resistance in the 1D model.

More specifically, it is obvious in the 3D model that the blood vessels of the CoW take complex paths through space. Furthermore, the diameters of a number of these segments comprising the circle are not of constant diameter, as approximated by the 1D model, especially at junctions. There are also problems with the assumption of a fully developed velocity profile, especially in the ACoA, which is a particularly short vessel where a velocity profile may not fully develop.

Finally, the assumption of steady flow, from which Poiseuille's law is derived, must be considered. Both models attempt to capture time dependent phenomena, and while the time dependent Navier Stokes equations capture time dependent behaviour, Poiseuille flow cannot. It can therefore be concluded that the discrepancy in circulus flux between the 1D and 3D models is most likely

due to the inaccurate assumption of Poiseuille flow which does not account for pressure losses through geometric complexity, particularly in the relatively small vessels such as the ACoA. Ultimately, the increased pressure loss through the communicating arteries means that when the peripheral resistance of the efferent arteries decreases in response to a decreased efferent flowrate, blood can be drawn through the communicating arteries in the 1D model, but will be drawn through the ipsilateral ICA in the 3D model.

3.5.2 Increased ACoA Resistance to Flow

The Poiseuille flow approximation effectively means that in the 1D model, more flow is able to pass through the communicating arteries than in the 3D model, for the balanced case. This difference can be overcome by increasing the resistance of communicating circulus vessels to produce the same effective resistance as the 3D model, and therefore achieve similar flux results. To match the 1D model fluxes to the 3D model fluxes, the resistance of the ACoA was increased 9-fold. A 9-fold increase in ACoA resistance was simulated in the ideal configuration of the 1D model, with the results shown in Figure 3.7, along with those without this change and those for the 3D model, repeated from Figure 3.6.

Increasing the ACoA resistance results in circulus and afferent fluxes in the 1D model that are much closer to those in the 3D model. Because less flow is able to pass through the ACoA, more flow is required to pass through the ACA_1 to supply the ACA_2. Without the increased ACoA resistance, enough flow can pass through to supply not only the ACA_2, but also to assist in supplying the ipsilateral MCA and AChA. This difference is evident in the change in direction of flow in the $RACA_1$ in Figure 3.7. In shorter vessels, vessels of variable diameter, and vessels taking indirect paths through space such as the communicating circulus vessels, Poiseuille flow assumptions result in resistance values that underestimate the actual resistance of those vessels to flow. Therefore, increasing the resistance of vessels such as the ACoA more accurately captures typical flow behaviour.

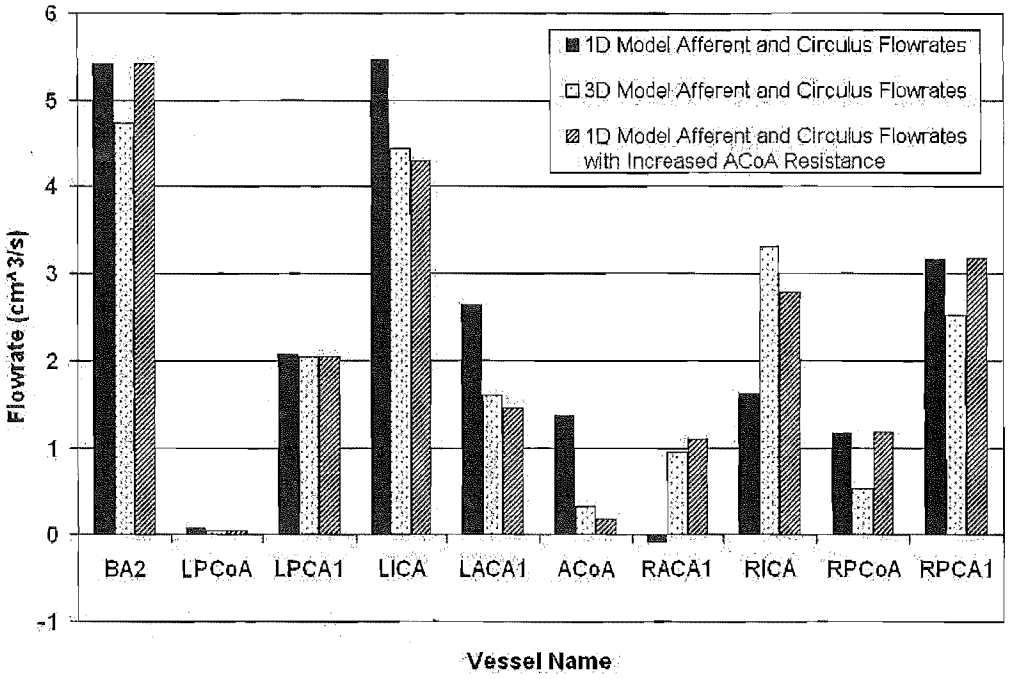

Figure 3.7 Comparison of Flowrates for 1D and 3D Models in the Balanced Configuration with an Increased ACoA Resistance

3.5.3 Absent Ipsilateral ACA_1

In a configuration with a missing ipsilateral ACA_1, blood must pass through the ACoA to supply the respective efferent ACA_2 segment, as it provides the only available route. The 3D model was unable to reach its reference conditions even before a 20 mmHg pressure drop was imposed on the RICA. With the ACA_1 absent, all the blood supply to the ACA_2 must pass through the ACoA, and the pressure loss through this segment therefore becomes so large that the peripheral resistance of the ipsilateral ACA_2 reaches its lower limit well before the reference fluxes can be obtained. The rest of the efferent arteries for the 3D model reach their reference flux in a short amount of time. Note that in the ideal configuration there is little flux through the ACoA, highlighting the impact of this vessel in a relatively common variation in CoW geometry. All of the efferent fluxes for the 1D model are initiated at their reference fluxes, including the ipsilateral ACA_2 segment, and the resistance of the ACoA is increased by a factor of 9, as discussed previously. Figure 3.8 shows the results of both models' attempt to reach the reference fluxes with this configuration. It is observed that the flux through the ACA_2 is $0.55 cm^3 s^{-1}$ less than the reference or desired value, indicating that ideal

perfusion cannot be reached since the downstream resistance of the ACA_2 has reached its lower limit. Conversely, the remaining efferent arteries are able to obtain optimal perfusion. The correlation between models is very good.

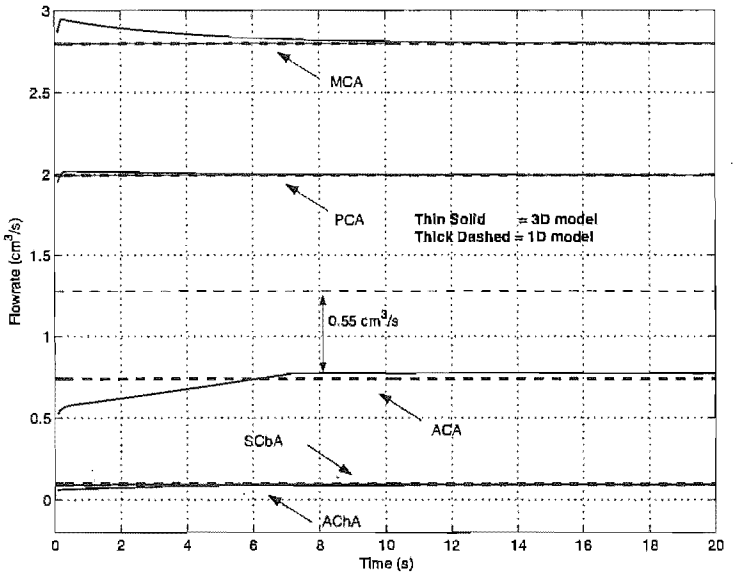

Figure 3.8 Steady State Ipsilateral Efferent Arterial Flowrate with an Absent $RACA_1$

Figure 3.9 illustrates the changes in resistance for both models. While the 3D model takes a certain amount of time to reach the lower resistance limit for the ipsilateral ACA_2, the 1D model begins the simulation in this state, due to the inner iterations guaranteeing equilibrium at each time step. However, the final resistance values are similar.

3.6 Summary

1D and 3D CFD models of the Circle of Willis were created to study autoregulation of cerebral blood flow. The geometry required to develop the 1D and 3D computational domains was based on a MRA of cerebro-vasculature and artery diameters given by Hillen et al. [1988]. The autoregulation process is described by a PID feedback control system, whereby the efferent flowrate error, indicating non-optimal perfusion, is feedback controlled by vasodilation and vasoconstriction of the capillary bed. Both models are concerned with the transient dynamics for autoregulation, where equilibrium is found not only before and long after afferent pressure perturbations, but also at every time step in between.

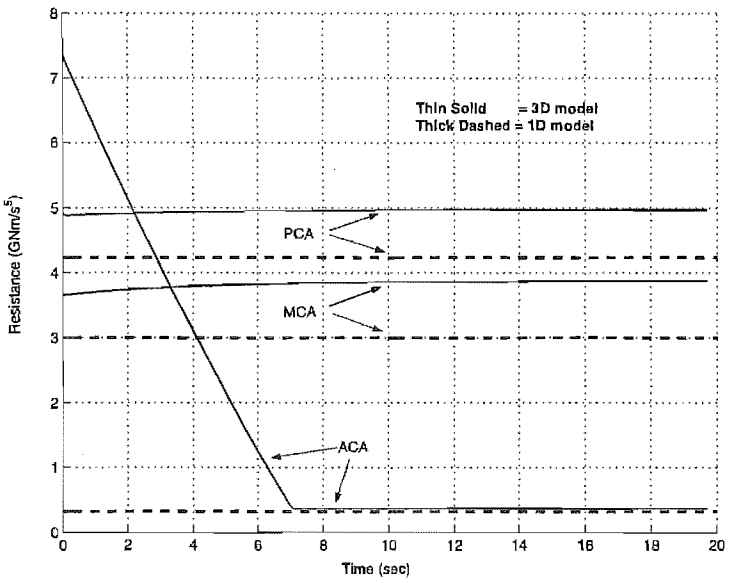

Figure 3.9 Steady State Ipsilateral Resistance

In both models, the RICA was subjected to a 20 mmHg pressure drop to observe the transient responses. The time dependent efferent flux profiles for the ideal configuration were found to exhibit excellent correlation between models. However, the Poiseuille flow approximation in the 1D model allowed for more flow through the communicating arteries than the 3D model, resulting in different circulus fluxes. To match the 1D model to the 3D model, the resistance of the ACoA was increased by a factor of 9 to correct for non-Poiseuille flow in this arterial segment. Incorporation of this increased ACoA resistance into the ideal configuration simulation improved agreement of circulus fluxes between models by an average of 60%. Although the 1D model initially requires validation from the 3D model, once verified, the 1D model obtains solutions in a far shorter time period requiring significantly less computational effort, and thus is a more suitable aid in real-time clinical decision-making. Overall, although both models use very different solution methods, results have been shown to be very comparable.

Future work will involve increasing the complexity of the 1D model, especially in providing more physiological parameters modelling the autoregulatory response. In addition, Since control is assumed to be decentralised, a 'tug of war' scenario is expected to occur if a sudden occlusion is imposed in an afferent artery, such that efferent flux profiles would fluctuate as a balance is found that best satisfies the independent requirements of the individual territories of the cerebral mass. Hence, it is important that both efferent and circulus fluxes match

between models. Future research will aim to verify this theory. Additionally, both models will be extended to include more accurate limits on peripheral resistance, in terms of the sensing and smooth muscle contraction mechanisms that bring about vasodilation and vasoconstriction of the arterioles in the individual brain territories supplied by the efferent arteries of the CoW.

Chapter 4

Decentralised Control Analysis and Resistance Limits

This chapter examines the decentralised nature of cerebral haemodynamic control to determine its impact on autoregulation and supply during clinical events. In Chapter 3, both the 1D and 3D models were subjected to a 20mmHg pressure drop in the RICA to observe the transient response for an ideal configuration. It was shown that the efferent flux profile for the ipsilateral side of the CoW is virtually identical between models for the balanced configuration, as seen in Figure 3.4.

During the course of the 3D comparison, it was postulated that a 'tug of war' scenario may occur if a sudden occlusion is imposed in an afferent artery, such that efferent flux profiles would fluctuate as a balance was found that best satisfies the independent requirements of the individual territories of the cerebral mass. This result is expected since control is assumed to be decentralised. Therefore, this chapter analyses this dynamic and its interaction with the resistance based limits of autoregulation.

4.1 Results

4.1.1 Occlusion of RICA

A situation is modelled in which the RICA becomes totally occluded. In both 1D and 3D models, a 'blood-stealing effect' is observed in which the flux profiles

of the MCA and ACA_2 fluctuate as a balance is found that best satisfies the independent requirements of each cerebral territory. This effect is clearly evident in Figure 4.1, where solid lines represent the 3D model and dashed lines show the 1D results.

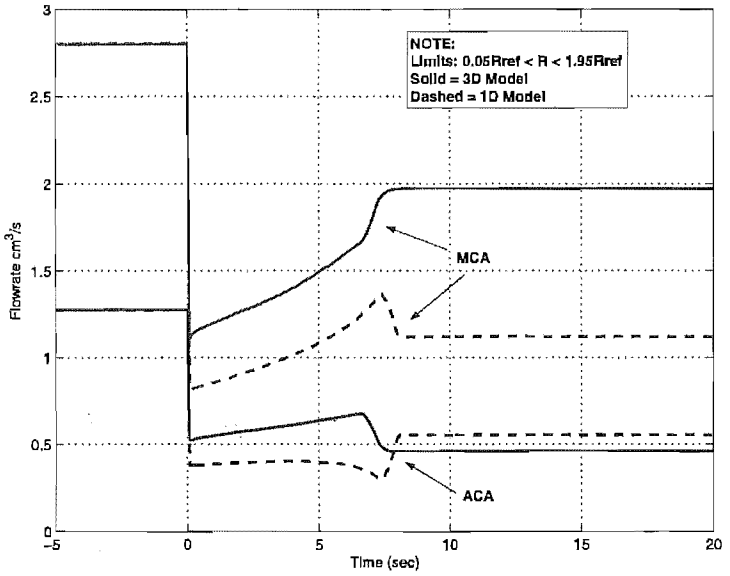

Figure 4.1 Ipsilateral Response to Occluded RICA

The response varies between models because of the different solution methods employed. In the balanced configuration case of Chapter 3, in which a 20mmHg pressure drop was simulated, the gains of the efferent arteries were set to match the clinical data of Newell et al. [1994]. Since the autoregulation control algorithm reacts to the magnitude of the flow error, the largest arteries required the smallest gains and the smallest arteries required the largest gains to achieve the same relative response. Therefore, the MCA had a smaller control gain acting on a larger error to give the same relative response as the larger ACA control gain acting on a smaller error.

In the 1D model, when the initial error detected is in the same ratio as the balanced case described above, an equal response would be expected such that no blood stealing would be observed since both arteries would be satisfied at the same time. In contrast, the error in the MCA in Figure 4.1 is proportionally bigger than that of the ACA_2, hence in the 1D model, its demands begin to be satisfied first. At time $t = 7.4$ sec, the ACA_2 has the proportionally larger error, so its demands start to be met, at the expense of the MCA.

The 3D model employs a different solution method in which the proportional gain plays a far greater role. It is observed that both the ACA_2 and MCA flows begin to return to their reference values immediately after the occlusion, with the MCA returning at a greater rate due to the proportionally larger MCA error as discussed for the 1D model. At time $t = 6.6$ sec, the MCA suddenly wins the 'tug-of-war', as a result is found that best satisfies the independent requirements of each cerebral territory. Due to lack of clinical data for verification, it is unknown at this time which model has the more accurate clinical response.

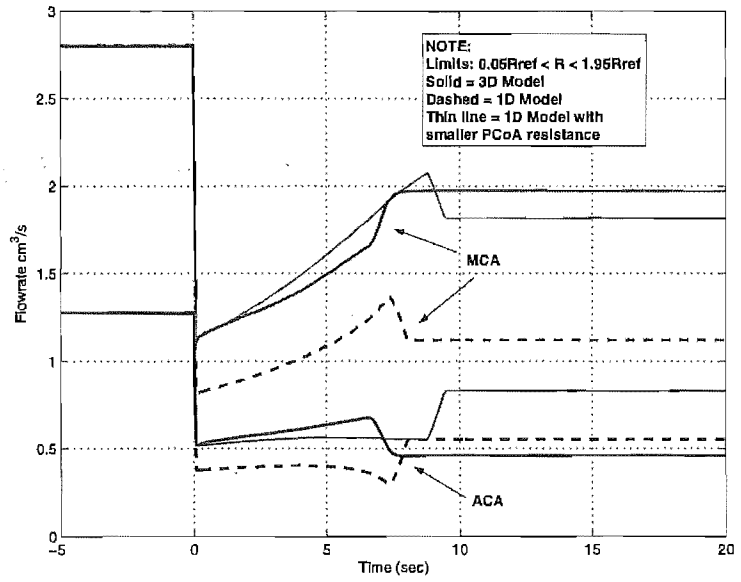

Figure 4.2 Ipsilateral Response to Occluded RICA with Increased PCoA Resistance

Figure 4.2 illustrates that the result is highly dependent on flow through the communicating arteries which are likely to be very patient specific due to the impact of their specific geometry. As mentioned earlier, the 1D model does not account for geometric complexity in its Poiseuille flow approximation, and as such allows too much flow through the communicating arteries. This effect was compensated for by increasing the resistance of the ACoA 9-fold, and the PCoA's 4-fold. In Figure 4.2, the thin line represents the response to occlusion when the resistance of the PCoA is increased by a factor of 2.5 instead of 4.0. This result hi-lights the difference between the two models in terms of solving for flowrates through the communicating arteries, and the need for more clinical verification.

4.1.2 Tighter Resistance Limits on Efferent Vessels

Previous results have assumed that the time-varying efferent resistances are capable of variations of 95%, corresponding to a change in arterial radius of 40% [Newell et al., 1994; Gao et al., 1998; Mancia and Mark, 1983]. It is currently thought that these limits are too relaxed, and in particular that they allow the arteries to dilate more than is physiologically observed. Guyton and Hall [1996] present a curve in which blood flow is expressed as a function of arterial pressure. This curve, shown in Figure 1.14, shows that autoregulation is efficient between mean arterial pressures of 70mmHg and 170mmHg, but is ineffective at pressures outside this range, indicating a limit of the autoregulatory system.

A similar curve for a balanced CoW with resistance limits of 95% is shown in Figure 4.3, which plots the normalised MCA flowrates at different mean arterial pressures. Of particular note from Figure 4.3, is that flow is maintained at much lower mean arterial pressures than observed physiologically. More specifically, the model allows efferent vessels to dilate to a greater extent than clinically observed.

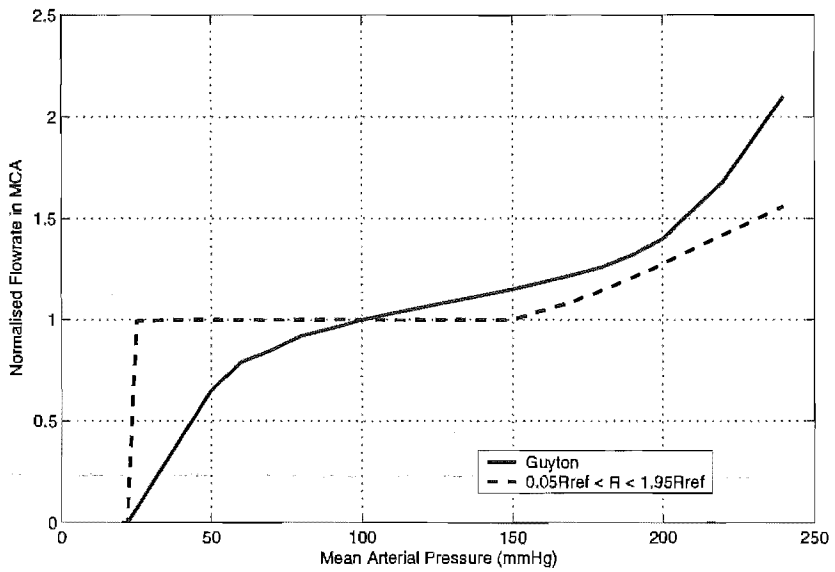

Figure 4.3 MCA Flowrate as a Function of MAP

The resistance limits were then reduced, such that the allowable resistance value was in the range $0.55R_{ref} < R < 1.7R_{ref}$. A 7% dead-band was also employed such that if the error obtained from the solution algorithm was within 7% of the reference value, the controller was switched off. The resulting curve is shown in Figure 4.4, and matched the clinical expectation well. Note that dashed

lines represent the limits of the physiological range usually observed in humans, as shown in Figure 1.19.

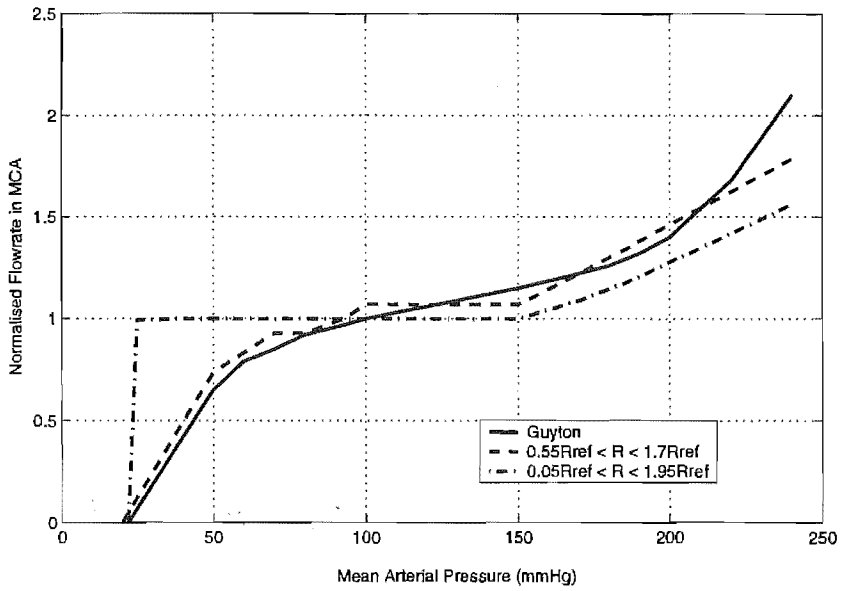

Figure 4.4 MCA Flowrate as a Function of MAP with 7% Deadband

4.1.3 'Blood Stealing' with Tighter Resistance Limits

As seen from Figures 4.3 and 4.4, the upper resistance limit has negligible effect on blood stealing because at high pressures there is oversupply. However, the lower resistance limit corresponding to dilation greatly affects the blood stealing phenomenon, as seen in Figure 4.5. More specifically, the tighter the lower resistance limit, the lesser the degree of blood stealing, and the more uniform the response. Figure 4.6 shows the 1D and 3D model responses to an occluded ICA, with the resistance limits $0.55R_{ref} < R < 1.7_{Ref}$. Note that the 1D model is shown with both a 4-fold increase in PCoA resistance and a 2.5-fold increase in PCoA resistance.

An increased PCoA resistance of 2.5 appears to more accurately match results from the 3D model. Both models show a much reduced 'blood stealing' response than was the case with resistance limits of $0.05R_{ref} < R < 1.95R_{ref}$. Although in both resistance limits cases, MCA and ACA_2 flowrates were unable to be restored to the reference values, with tighter limits on dilation, these flowrates

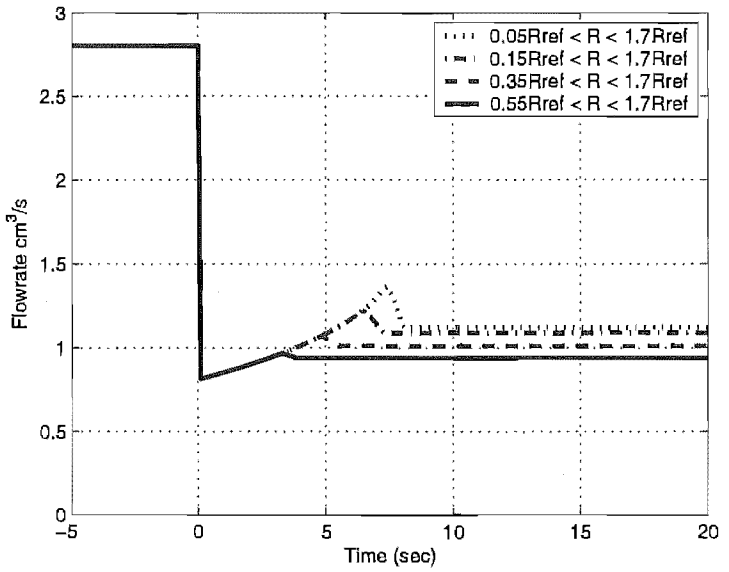

Figure 4.5 RMCA Flowrate in Response to Occluded RICA - Varying Resistance Limits

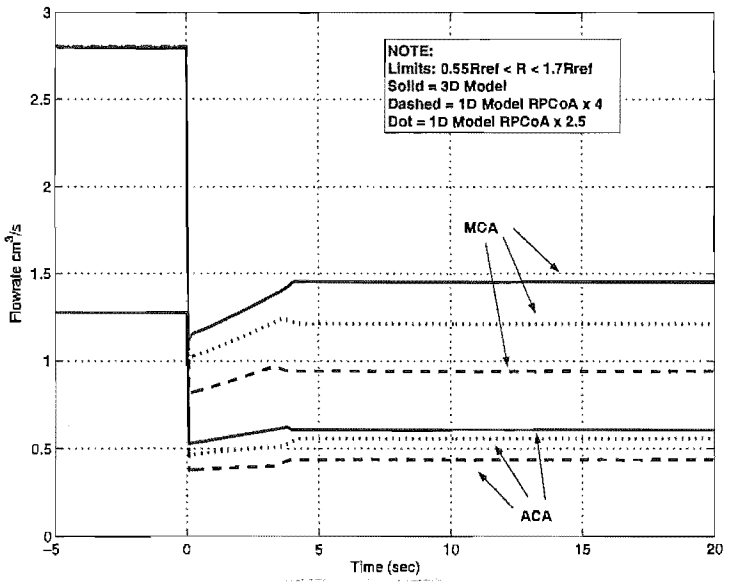

Figure 4.6 Ipsilateral Response of MCA and ACA_2 to an Occlusion of the RICA - Tighter Resistance Limits

did not return as close to reference as in the weaker limits case, as seen in Table 4.1.

In the weak resistance limits case, blood stealing did not occur until flowrates had returned to a particular percentage of their reference value. With tighter limits, this value is never reached, and so blood stealing is greatly minimized.

Table 4.1 Percentage of Reference Resistance Achieved after RICA Occlusion

	3D model		1D model PCoA x4		1D model PCoA x2.5	
	MCA	ACA	MCA	ACA	MCA	ACA
Tight Limits ($0.55R_{ref} < R < 1.7R_{ref}$)	52	48	34	34	43	44
Weak Limits ($0.05R_{ref} < R < 1.95R_{ref}$)	71	36	47	65	50	65

4.2 Summary

1D and 3D CFD models of the CoW were used to study the decentralised nature of autoregulation. With weak dilatory resistance limits, results show that if a sudden occlusion is imposed in an afferent artery, a 'tug of war' scenario occurs, such that efferent flux profiles fluctuate as a balance is found that best satisfies the independent requirements of each territory of the cerebral mass. With physiologically realistic, tighter resistance limits matched to data from Guyton and Hall [1996], this blood stealing phenomenon is minimized, but not eliminated. Hence, clinically, the decentralised aspect of cerebral autoregulation could result in ischaemic stroke after sudden pressure drops due to stenoses or occlusions, where a centralised controller would have a different outcome. This study hi-lights the need for more physiologically accurate models of autoregulation, as well as better approach for determining physiological resistance limits.

Chapter 5

Metabolic Model of Autoregulation

5.1 Introduction

Chapter 2 presented a basic model of the CoW. Although some good results and correlations with prior models and clinical data were achieved, the model was too simple to capture all the transient dynamics of autoregulation. Chapter 3 validated the 1D model against a 3D CFD model, and pointed out certain limitations, such as the Poiseuille flow approximation allowing for too much flow through the geometrically complex communicating arteries. Chapter 4 investigated the decentralised nature of autoregulation control, and found that the physical limits of vessel contraction and dilation, and hence autoregulation, were not well defined. A more physiologically realistic model was required to overcome these weaknesses in the model.

An advanced model was created that included the successful components of the previous model, as well as better resistance limits for smooth muscle vasomotion, and the oxygen dynamics that drive the autoregulatory response. This advanced model is more physiologically relevant, matching the accepted physiological responses of blood flow as a function of arterial pressure, tissue oxygen partial pressure as a function of blood flow, as well as limited transient clinical data. Cerebral haemodynamic autoregulation is captured by using a PID controller to modify efferent artery resistances and partial pressures of oxygen to maintain optimal efferent flowrates and oxygen supply to the cerebral mass for a given circle geometry and afferent blood pressure.

More specifically, the model adds simple oxygen metabolism dynamics. As

oxygen deficiency is the prime trigger for cerebral autoregulation, it is an input for this mechanism. Oxygen itself is assumed proportional to flow, and its changes are a function of the error from a reference flow. The consequent changes in oxygen result in vessel dilation/contraction as part of autoregulation. These changes in turn, affect/correct, flow. The overall mechanism with two dynamics is thus more physiologically relevant.

This advanced model uses the full configuration of the CoW with ten main efferent vessels, as shown in Figure 3.1, and repeated in Figure 5.1.

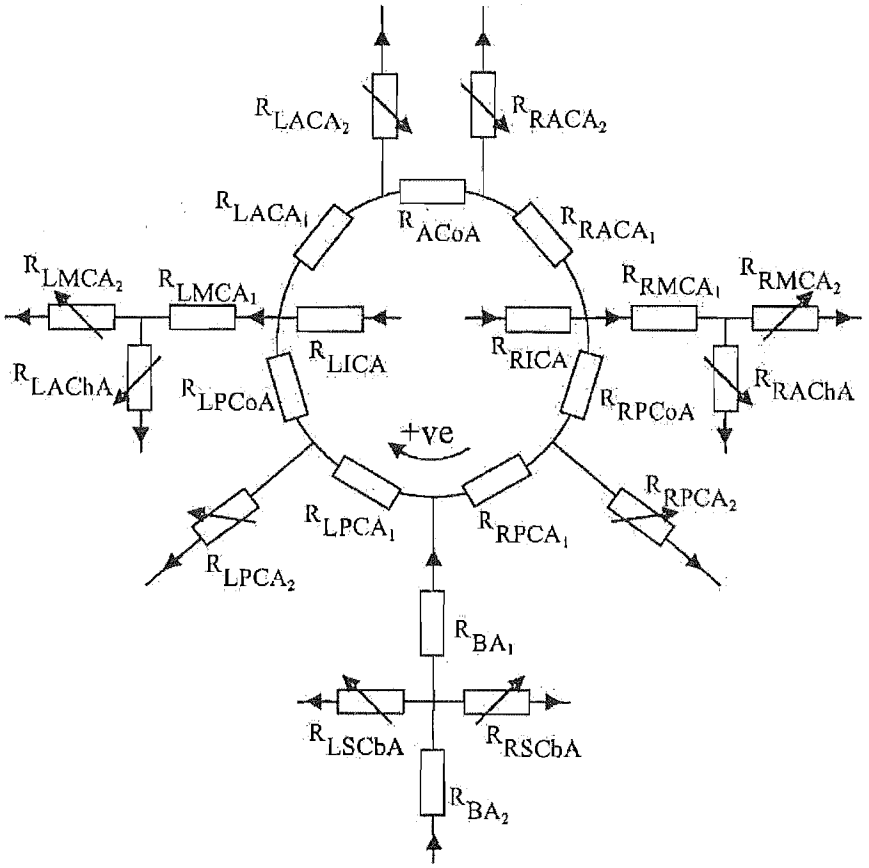

Figure 5.1 Schematic of the Advanced CoW Model

5.2 Autoregulation Dynamics

This model represents a metabolic model of autoregulation, where a decrease in blood flowrate results in a decreased interstitial oxygen partial pressure, causing a greater formation of vasodilator substances diffusing to the smooth muscle cells

to cause muscle relaxation. The result is a change in efferent resistance. Thus, there are two dynamics: 1) for oxygen signal pathway dynamics, and 2) for the resulting smooth muscle contraction/dilation dynamics.

Guyton and Hall [1996] present a curve in which blood flow is expressed as a function of arterial pressure. This curve, shown previously in Figure 1.14, shows that autoregulation is efficient between mean arterial pressures of approximately 70mmHg and 170mmHg, but is ineffective at pressures outside this range, indicating a limit to the autoregulatory system. Normal cerebral blood flow is 48-50mL blood/100g cerebral tissue/min. However, if this reference flow is not obtained, stroke will not necessarily ensue automatically. The ischaemic threshold is generally considered to be approximately 20mL/100g/min [Heiss et al., 1999; Baron, 2001], although it should be noted that tissue perfused at 20mL/100g/min is not necessarily irreversibly damaged immediately, because the length of time that tissues are perfused at such levels plays an important role. That is, if flow is later restored to the region of the brain suffering a deficiency, or if adequate collateral flow is supplied, the cerebral tissue can be fully or partially salvaged. For the purposes of this study, perfusion of 20mL/100g/min is assumed to cause stoke. As such, a 'stroke line' can be inserted onto the curve of Figure 1.14 at 0.408 times normal blood flow, as shown in Figure 5.2.

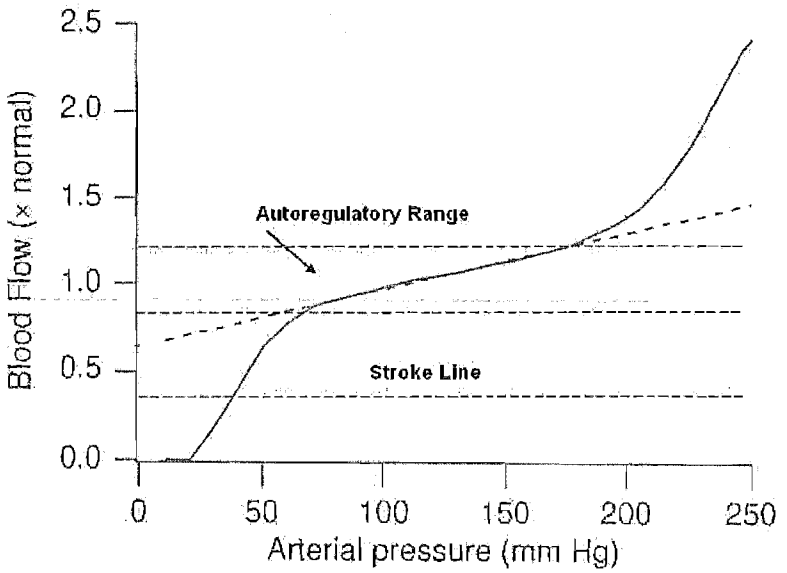

Figure 5.2 Effect of MAP on Blood Flow

The plateau region of Figure 5.2 from approximately 70-170mmHg indicates

the region where autoregulation operates effectively. It can be modelled:

$$Q = \frac{1}{1 + B \times [O_2]_a}\left(M \times B + \frac{P_a - P_v}{R_0}\right) \tag{5.1}$$

where flowrate, Q, is expressed as a function of arterial oxygen concentration, $[O_2]_a$, metabolic rate, M, arterial and venous pressures, P_a and P_v, B indicates the sensitivity of resistance to oxygen, and R_0 is a parameter linking arterial resistance with venous oxygen content [Keener and Sneyd, 1998]. Both of these parameters can be found for the steady state using normal values for arterial and venous oxygen concentration of 104mmHg and 40mmHg respectively, as well as a normal metabolic rate defined:

$$M = Q([O_2]_a - [O_2]_v) \tag{5.2}$$

Note that the model of Equation 5.1 accurately follows the curve in Figure 5.2 up to pressures of 220 mmHg, as seen in Figure 5.3, and that human mean arterial pressures are rarely encountered beyond 200mmHg [Guyton and Hall, 1996], as it would entail an extremely high systolic pressure of approximately 240mmHg. The MAP at which the stroke line intersects with the model is approximately 34mmHg. Therefore, an afferent pressure drop to just below 34mmHg in an individual with no other abnormalities, would be expected to cause stroke, in this illustrated case.

Efferent arteries are modelled with variable resistors per the prior modelling in chapters 2-4. These resistors are capable of variations in resistance of between 50% and 155% of the 'normal' resistance, per the results in chapter 4.

$$0.5 \times R_{ref} < R < 1.55 \times R_{ref} \tag{5.3}$$

Note that these variations are consistent with the data in Figure 5.2, but are slightly tighter than the clinical observations of Fog et al. [1937], who found a maximum dilation corresponding to a 57% decrease in resistance. A 50% decrease in resistance corresponds to a 19% increase in radius, whereas a 57% decrease

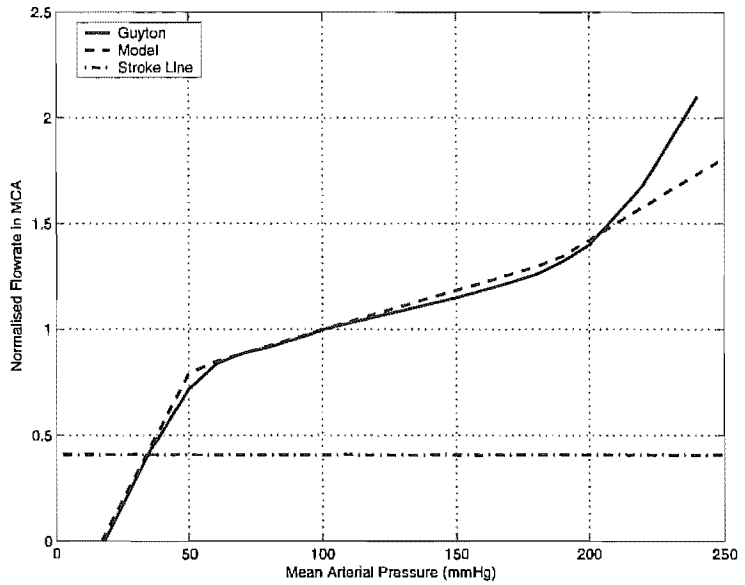

Figure 5.3 Flowrate as a Function of MAP

in resistance corresponds to a 23% increase in radius, using Equation 2.2. Note however, that clinical data is found to be widely varying, as seen in Figure 1.13 [Dirnagl and Pulsinelli, 1990].

To prevent stroke, autoregulation must try to maintain flowrates in the middle linear range, or at least above the 'stroke line' in Figure 5.2. Outside the autoregulatory range, autoregulation is unable to restore flowrates to their reference values. Hence, they rise above or fall below the desirable range of flow, resulting at the extreme of MAP, in stroke. Reference flowrates are therefore set to follow the dotted line in the model in Figure 5.4, even if it is not physically possible to achieve. This approach captures the body's drive to maintain a desired range of flow at any near arterial pressure, regardless of autoregulatory capability, which is modelled separately.

When arterial blood reaches the peripheral tissues, the pressure difference encountered drives the flow of blood into the tissues, from which oxygen diffuses to the tissues based on partial pressures differences. If the blood flow through a particular tissue increases, there is a greater transport of oxygen, such that the oxygen concentration in the interstitial fluid increases above the normal 40 mmHg. The rate of oxygen consumption (ie metabolic rate) can also play a role, although only normal metabolic rates are considered at this time.

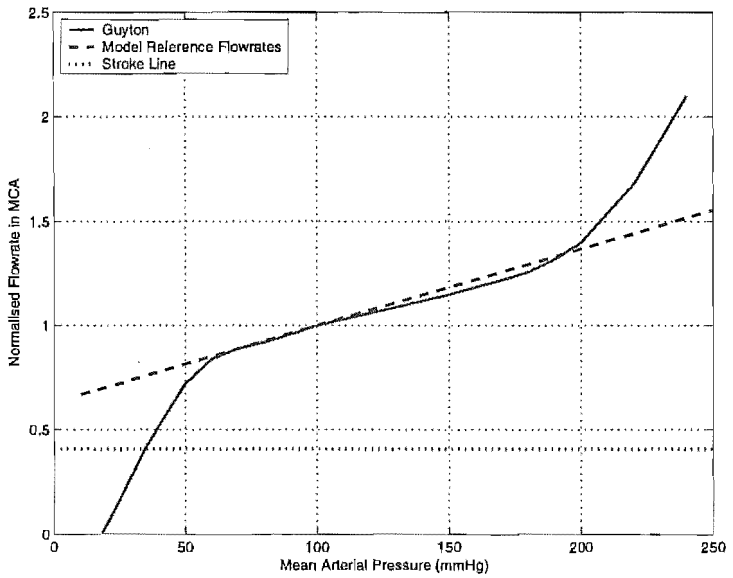

Figure 5.4 Autoregulation Limits

Guyton and Hall [1996] present a curve in which interstitial oxygen partial pressure is expressed as a function of flowrate. A curve has been fitted to this data, as shown in Figure 5.5, and is defined:

$$iPO_2 = (Q + 64) \times (1 - e^{-0.87 \times Q}) \tag{5.4}$$

where interstitial partial pressure of oxygen, iPO_2, is a function of normalised flowrate, Q.

The autoregulation process can then be *generically* described by relatively simple feedback control systems. where the control input, $u(t)$, is a function of the error, e, from a reference value, at that timestep:

$$u(t) = K_p\, e + K_i \int e + K_d \frac{de}{dt} \tag{5.5}$$

where K_p, K_i and K_d represent proportional, integral and derivative control gains respectively, and are found by matching clinical data from the Newell et al. [1994] thigh cuff experiments where. The data, which is shown in Figure 5.6 after releasing the thigh cuff, shows a 20% drop in blood pressure, where the MCA

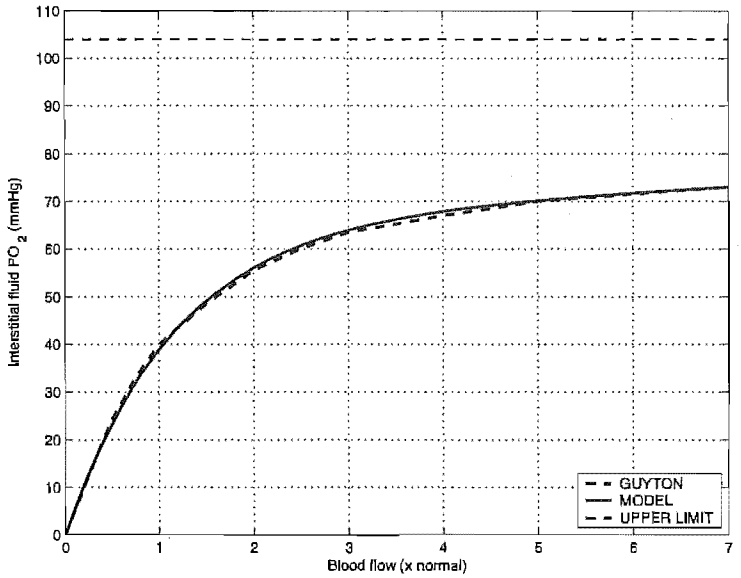

Figure 5.5 Interstitial Oxygen Partial Pressure as a Function of Flowrate

took approximately 20 seconds to return to normal flow conditions.

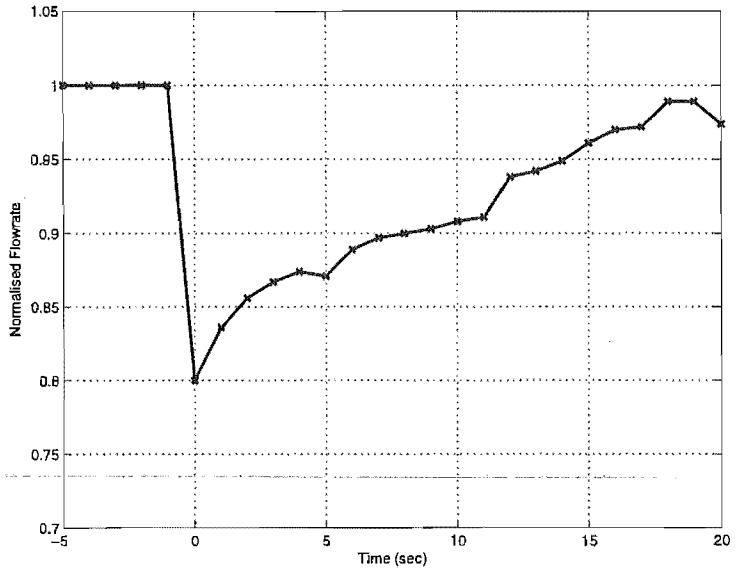

Figure 5.6 MCA Flux Profile after 20mmHg Afferent Pressure Drop - Newell et al.

The dynamic behaviour of the system can be described by simple first order dynamic systems of the form:

$$\dot{x} = \frac{1}{\tau_1}(x_{ref} - x) + \frac{1}{\tau_2}u(t) \tag{5.6}$$

where x is the parameter in question (partial pressure of oxygen or peripheral arterial resistance), τ_1 and τ_2 are time constants associated with the biochemical pathways, and $u(t)$ is the control input defined in Equation 5.5.

Based on the pressure at each timestep, the reference flowrate can be found using Figure 5.4, and therefore the correct oxygen partial pressure can be found from Figure 5.5. Inner iterations use the error in flowrate and in oxygen partial pressure to calculate the control input required to correct the error. The solution process is shown in Figure 5.7. Figure 5.7 also shows the exact forms of Equations 5.5 and 5.6 for the oxygen dynamic signalling pathway and arterial vasoconstriction/vasodilation dynamics.

At each timestep, the afferent pressures are known. Therefore, using Figures 5.4 and 5.5, Q_{ref} and iPO_2ref are known. When there is a change in afferent pressure, the flowrate, Q, calculated using resistances from the previous timestep, varies from Q_{ref}. This change in flow causes a change in oxygen partial pressure. A control input based on the flow error is used to correct for the partial pressure of oxygen. This change in oxygen partial pressure causes a change in the diameter and thus resistance of the vessel.

A control input based on the error in oxygen partial pressure is used to correct for the vessel resistance. These new peripheral resistances are used to reform the $\underline{A}$ matrix, and Equation 2.4 is re-solved for flowrates and circulus pressures. The new flow error is then re-calculated, and the inner iteration continues until convergence, and thus equilibrium, is reached for that timestep.

The time constant associated with resistance dynamics is 3 sec, ($\tau = 3$ in Figure 5.7) whereas the time constant associated with oxygen dynamics is 35 sec, ($\alpha = 35$ in Figure 5.7). These values indicate that constriction/dilation of vessels in response to changes in the concentration of vasodilator substances occurs faster than oxygen delivery to the tissues and the accumulation/reduction of metabolites in response to changes in flowrate, as expected.

For the oxygen dynamics, the integral gain is the major control component, whereas for the resistance dynamics, the derivative gain is the most important. Integral memory has been incorporated into the model to ensure a graded error. More specifically, discrepancies in flowrate and oxygen concentration in the dis-

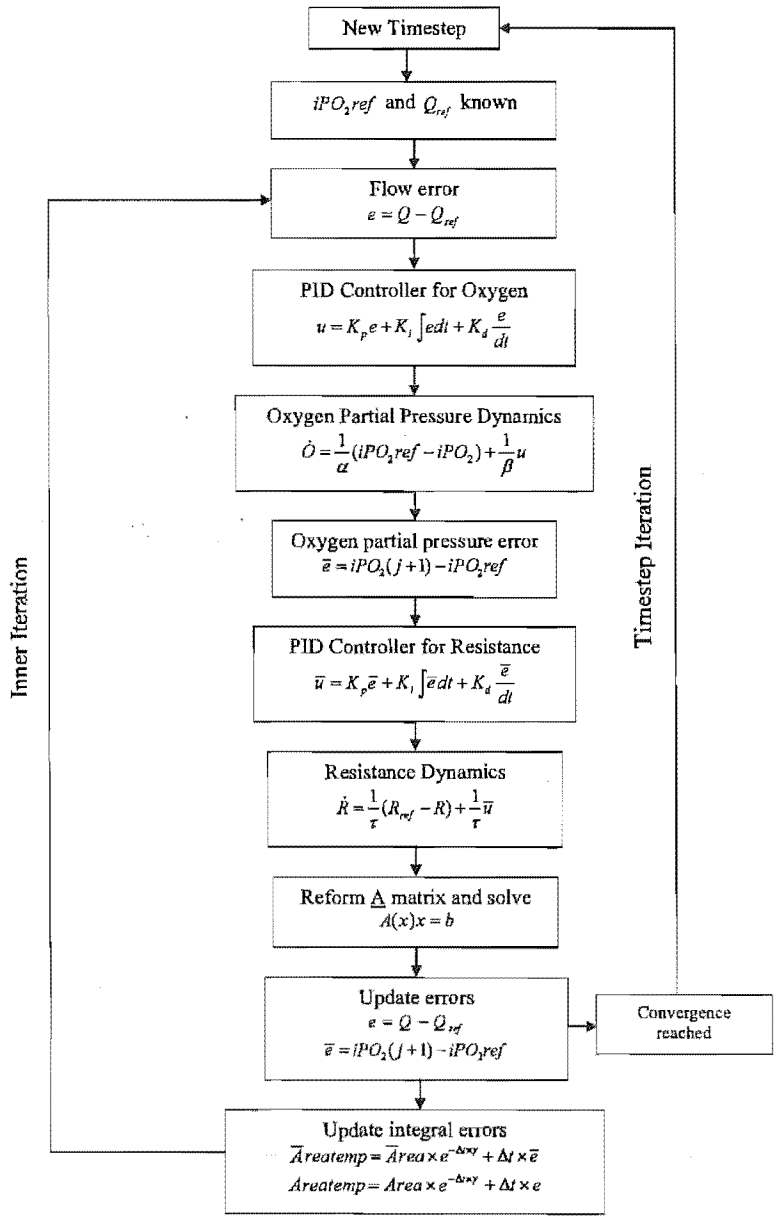

Figure 5.7 Solution Method

tant past are considered by the model to be less important than discrepancies at the current and more recent timesteps. Integral memory can be physiologically explained by metabolites and other signalling chemical ions only being active in

the bloodstream for a finite time period.

This model is an improvement on many previous models in that it recognises the non-linearity of the system, and requires inner iterations to solve for equilibrium at each time-step. In addition, it is physiologically, a more realistic model, accounting for oxygen diffusion and vasodilator generation, as well as smooth muscle vasoconstriction and vasodilation, unlike other similar previous work [Moorhead et al., 2004].

5.3 Model Verification and Simulation Methods

The overall system model allows for many variations in circle geometry. To simulate an absent vessel, the resistance of that vessel is set to a large value ensuring negligible flow through that segment. Similarly, simulation of string-like vessels can be performed by setting resistances to as much as sixteen times their original value. An increase in resistance of sixteen times is equivalent to a decrease in artery radius of 50%. In addition, any type of time-varying afferent mean arterial pressure profile is easily simulated. These simulations have been used to model rapid pressure drops caused by a stenosis and surgical procedures, such as a carotid endarterectomy. Several combinations of clinically verified geometries and situations can be modelled using far less computational effort than similar models using higher dimensional CFD.

5.3.1 Investigation of Advanced Model Parameters

When an arterial pressure drop from 100mmHg to 80mmHg is simulated with both the old and advanced models, the results in Figure 5.8 are obtained. Note the difference in shape between the old and new models. The new model clearly has an initial fast response followed by a slower response, as is observed to occur in Newell's data [Newell et al., 1994] from Figure 5.6. Additionally, no combination of autoregulation control gains in the original, single dynamic, model can provide this shape of response. Hence, the added oxygen dynamic in this model enables a wider range of dynamic responses to be modelled.

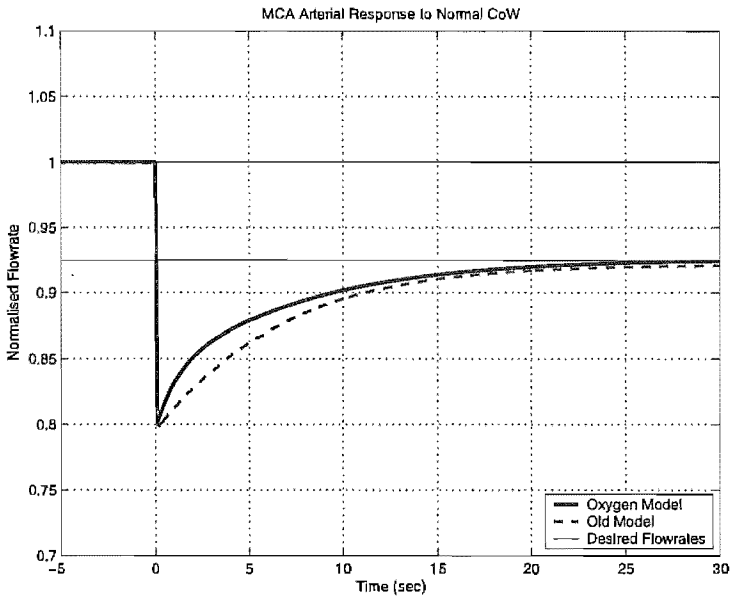

Figure 5.8 A Comparison of the Shapes of the Old and Advanced Models

Flux profiles were compared when the model is run with and without integral control. As seen in Figure 5.9, the characteristic shape of the new model was lost when integral control was abandoned from both dynamics, and the flux profile obtained was very similar to the old model profile.

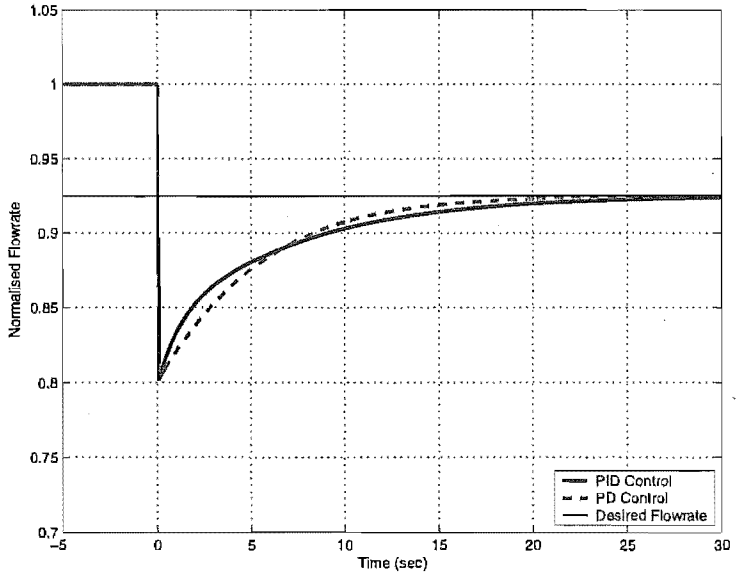

Figure 5.9 Comparison Between PD and PID Control for a 20mmHg Pressure drop in the Afferent Arteries

Since there is only one piece of clinical data available in Newell et al. [1994], it is possible that other flux profile shapes may more accurately describe physio-

logical behaviour. Figure 5.10 shows some flux profiles that can be obtained using the new model, however until more clinical data is available, one can not be sure which profile is the most accurate. Therefore, the profile with the high resistance gain matching the data of Newell in Figure 5.6, is used in the remainder of the simulations.

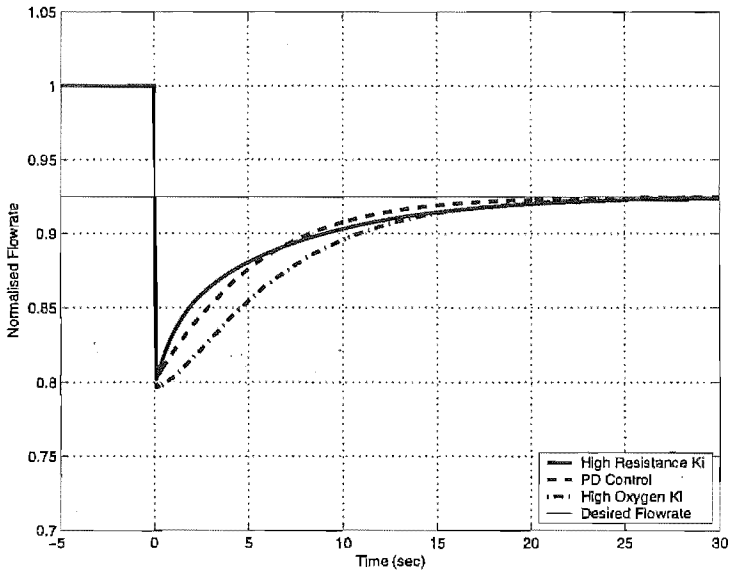

Figure 5.10 Comparison of Different Flux Profiles Obtainable with the Advanced Model

5.3.2 Model Verification using Clinical Data

Newell et al. [1994] performed thigh cuff experiments in which releasing cuff pressure caused a pressure drop in all afferent CoW vessels from 100mmHg, which wavered towards 80mmHg before climbing to 86.2mmHg, as shown in Figure 5.11.

The complete CoW is modelled with venous pressures of 7mmHg, intracranial pressure of 10mmHg [Walters, 1998], and an arterial pressure profile following that of Newell et al. [1994] in all afferent arteries. Figure 5.12 shows a comparison between this metabolic model and the results of Newell et al. Note that the maximum error in Figure 10 is 2.58%, while the average error is 1.03%, thus the model shows excellent correlation with clinical results.

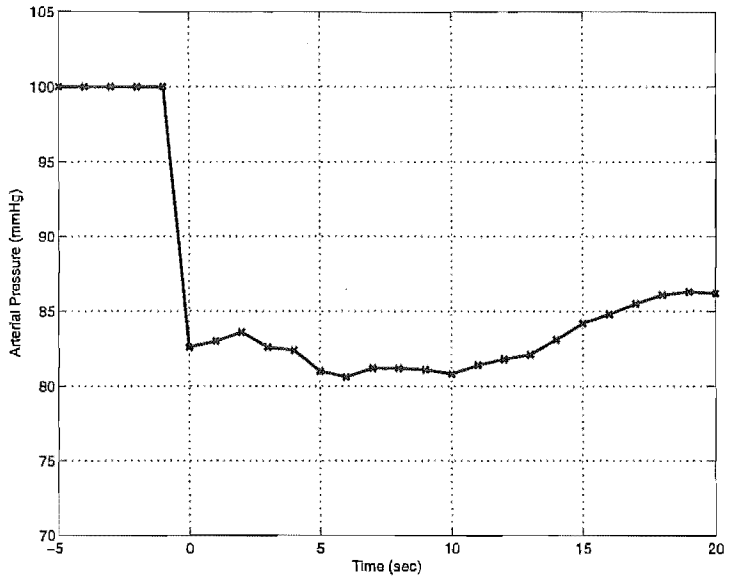

Figure 5.11 Newell Pressure Data

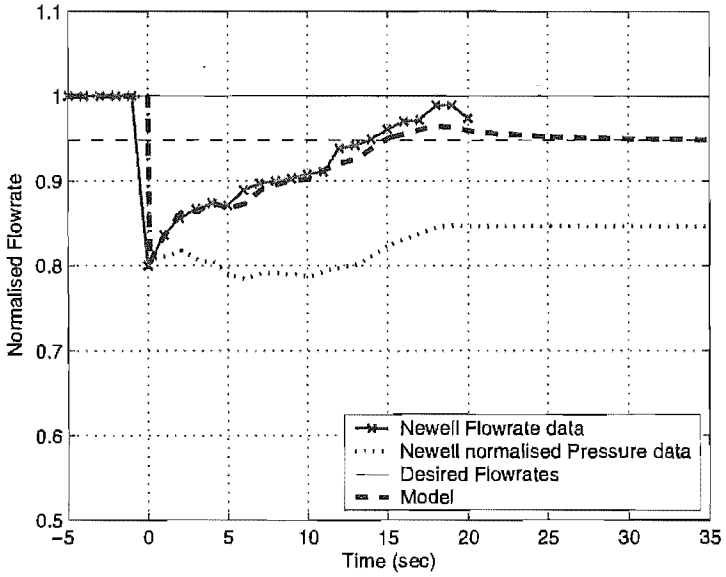

Figure 5.12 Comparison of Oxygen Model with Newell Flux Profile

5.3.3 Asymmetric Afferent Arterial Pressures

Modelling the same pressure drop in all afferent arteries provides the results in Figure 5.12. However, to model a stenosis or occlusion in one afferent artery, the input pressures will vary in each afferent artery. Figure 5.4 is used to find the desired flowrates in this case. To model a 20mmHg pressure drop in the RICA,

the model of Figure 5.4 is run without a pressure drop with afferent pressures of 100mmHg in the LICA and BA, and 80mmHg in the RICA. The steady state efferent flowrates obtained are the reference flowrates to be used in the main metabolic autoregulation model, during a transient analysis of a RICA drop of 100mmHg to 80mmHg.

Simulations are then carried out using this approach for the balanced configuration and each case where a single circulus vessel is omitted. In all cases where only one vessel in the CoW was removed, the system is able to obtain the reference efferent flowrates upon simulation of a surgical procedure causing a temporal pressure drop of approximately 20% in the RICA. To reach the reference flowrates, the flow is redirected as a result of independently changing resistance in the vascular bed of each efferent artery - the cerebral autoregulation function.

5.4 Results and Discussion

The results displayed in the remainder of this research use a bar chart format. The x-axis has afferent vessels on the left, and then follows the circulus vessels clockwise starting at the $LPCA_1$, with flowrates through efferent arteries shown on the right. Bars below the x-axis indicate that flow is in the opposite direction to that assumed by the sign convention in Figure 5.1. The four bars indicate from left to right:

1. flowrates before the pressure drop;
2. flowrates after recovery from the pressure drop;
3. the desired reference flowrates after the pressure drop; and
4. the ischaemic threshold

The goal of autoregulation is to match the second and third bars, however, stroke is only deemed to occur if the third bar falls below the fourth bar. Schematic figures show flow directions after the pressure drop, where solid arrows indicate a change in direction of flow from the steady state, pre-pressure drop case, and open arrows indicate that the flow direction has not changed.

5.4.1 Balanced Configuration

The 'normal' case with a complete CoW is used as a baseline for analysing results. The solid black bars in Figure 5.13 therefore show zero flowrate through the ACoA and equal flowrates across each of the left and right sections of the circle. The symmetry in the flow is due to the symmetrical nature of the resistances in the circle and the incoming flows. The minimal flow observed in the PCoA's is due to the very high resistance of these vessels, and as a result, the BA supplies mainly the efferent PCA's, and the ICA's supply the efferent MCA's and ACA's.

A stenosis or occlusion in the RICA is simulated by a pressure drop from 100 to 80 mmHg, and the resulting flowrates are shown in Figure 5.13. When compared to the normal pre-pressure drop scenario, flow is observed to drop in the RICA and increase in the LICA and BA to compensate. The pressure change in the RICA also causes a change in the direction of flow through the $RACA_1$ resulting in a clockwise flow through the anterior regions of the circle, delivering flow from the LICA through the ACoA to the starved $RACA_2$ and RMCA. Lastly, note that all efferent arteries recover reference flowrates after the pressure drop.

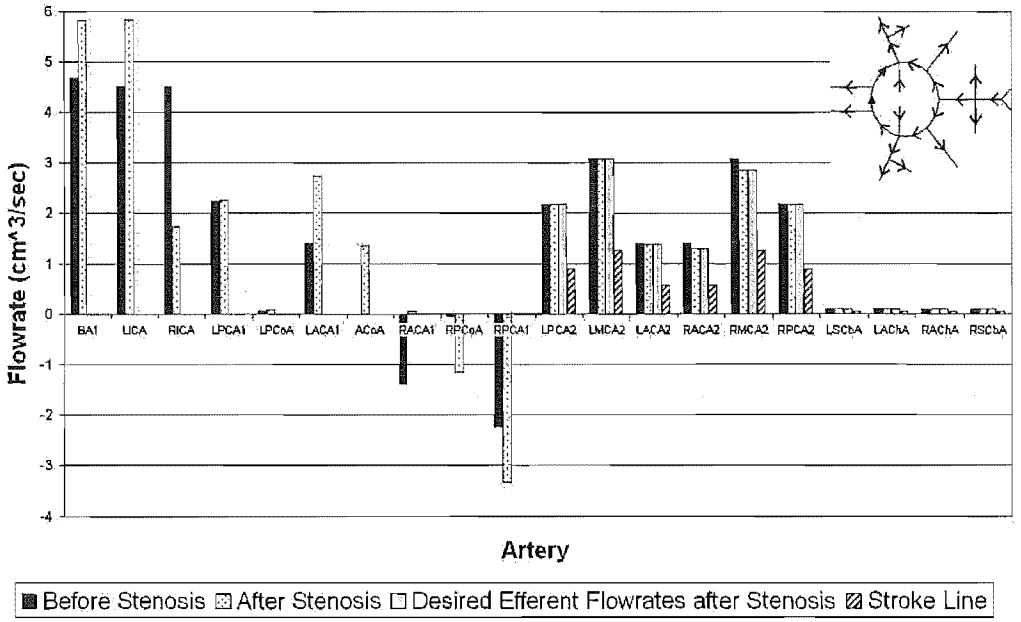

Figure 5.13 Balanced Configuration Response to 20mmHg Pressure Drop in RICA

The step change in pressure from 100mmHg to 80mmHg in the RICA, results in significant changes in the flowrate and the pressure differential in the RMCA. This result is expected because the RMCA is the first of the efferent vessels to

be supplied by the RICA. More specifically, the flowrate dropped 20% and took approximately 20 seconds to return to its original value, as seen in Figure 5.14. The $RACA_2$ also had a 20% drop in flowrate when the pressure drop occurred. The SCbA's and AChA's are not shown due to the tiny amount of flow through these vessels. However, as seen in Figure 5.13, they do obtain their reference values after the pressure drop. Note that the desired flowrates shown in Figure 5.14 are the desired flowrates after recovery from the pressure drop.

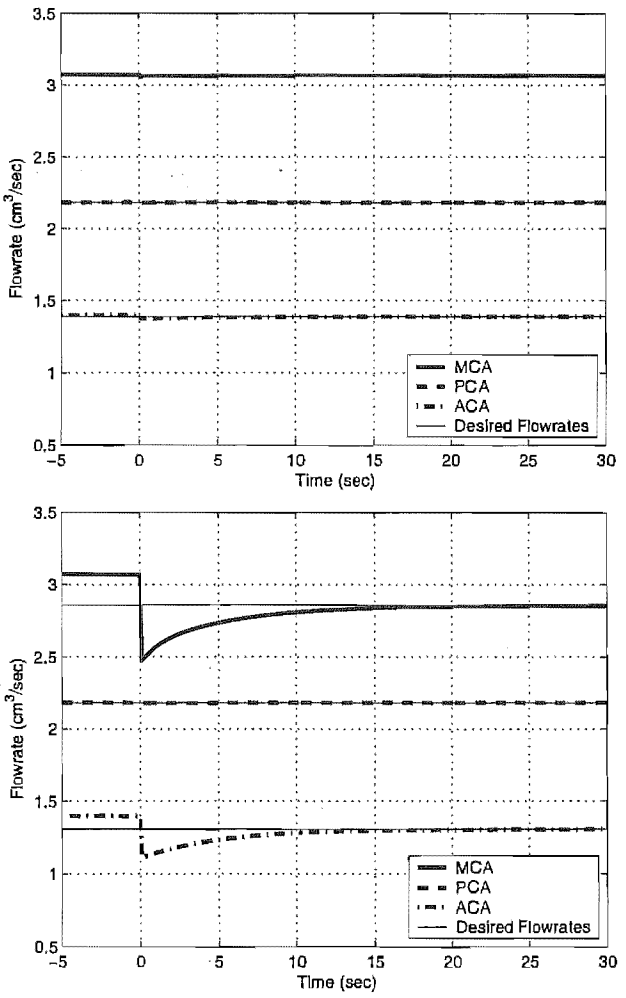

Figure 5.14 Efferent Arterial Response to 20mmHg Pressure Drop in RICA in the Balanced Configuration. Left Efferent Response (*top*); Right Efferent Response (*bottom*)

5.4.2 Absent ACoA

An absent or restricted ACoA is a common physiological condition, and under normal conditions an absent ACoA poses no threat to brain function as shown by the zero flowrate through the ACoA in the normal balanced configuration case in Figure 5.13. The complication of the omission of the ACoA is only significant under flow conditions such as a stenosis or occlusion of an afferent artery, where other arteries are absent, or where there is asymmetry in the circle.

Before the pressure drop, flow through the left and right PCA_1 were identical, whereas after the pressure drop, flow through the $RPCA_1$ increased significantly. This observation is a result of compensation for the pressure drop in the RICA by the BA, which delivers blood at a higher rate through the $RPCA_1$ and RPCoA to supply the RMCA. It can thus be seen that the communicating arteries play a more significant role when the geometry is unbalanced in this fashion, as seen in the flowrate changes in Figure 5.15.

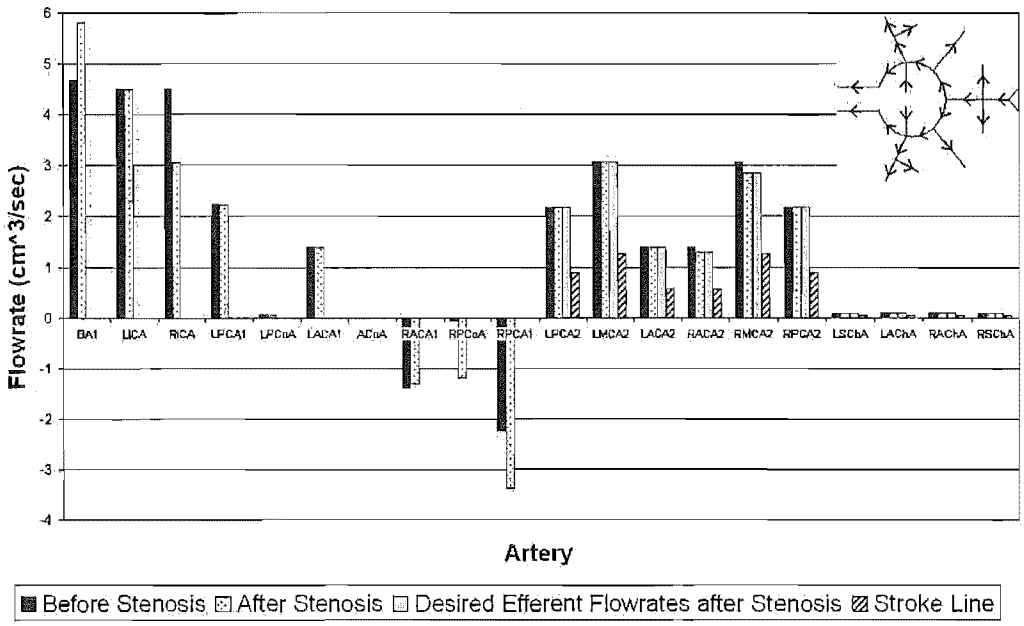

Figure 5.15 Absent ACoA Configuration Response to 20mmHg Pressure Drop in RICA

Unlike the balanced case, the simulated stenosis in the RICA in the absent ACoA case results in little change from the normal flow case. The reason for the low change is that the ACoA can no longer be used to reroute flow from the LICA to help supply the starved right efferent vessels. Flow in the left portion of the brain is virtually unaffected by the stenosis in the RICA. Flow through

the $RACA_1$ changes only to account for the new target ACA_2 flowrate after the pressure drop, as expected since there is no flow through the ACoA. Immediately after RICA stenosis, flow actually increases through the LMCA and $LACA_2$ by 0.2% and 0.3%, respectively. This result is due to an increase in flow through the LICA immediately after the pressure drop to try to compensate for the loss in the RICA. After the LMCA is supplied, the extra flow must go to the $LACA_2$ since no flow can pass through the ACoA. Flow through the LICA then decreases, since its previous increase was not helping supply the right efferent vessels. Flowrates through the LMCA and $LACA_2$ then decrease to their reference values. The immediate increase in flowrate through the LMCA is shown in Figure 5.16, and represents the capture of a very complex, non-linear dynamic for such an overall simple model. The temporal response to a 20mmHg pressure drop in the RICA is shown in Figure 5.17.

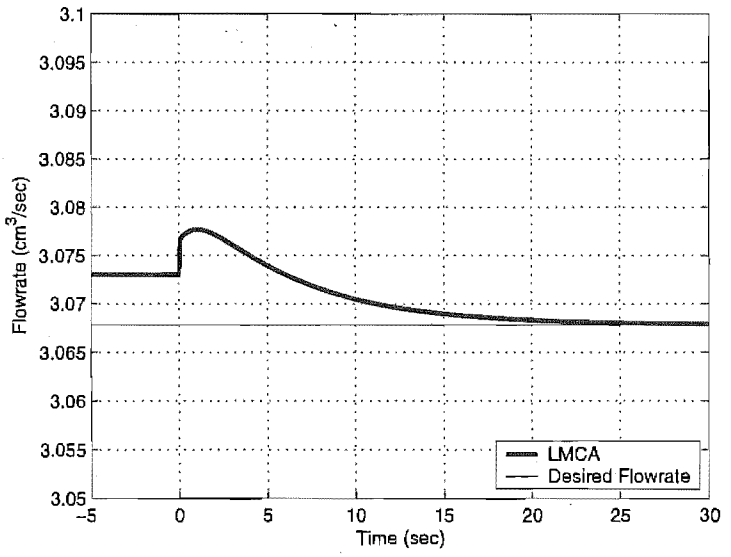

Figure 5.16 LMCA Response to 20mmHg Pressure Drop in RICA with an Absent ACoA

5.4.3 Absent $LACA_1$

This case was very similar to an absent ACoA response in that there was very little difference between the pre-pressure drop scenario and the stenosis situation, especially in the left portion of the brain. Immediately after the RICA stenosis, the RMCA dropped 20% before returning to its asymptotic value, and the $RACA_2$ and $LACA_2$ dropped 22% and 24%, respectively. Note that this immediate drop in flowrate in the $LACA_2$ was the largest in all geometric cases studied. Also of

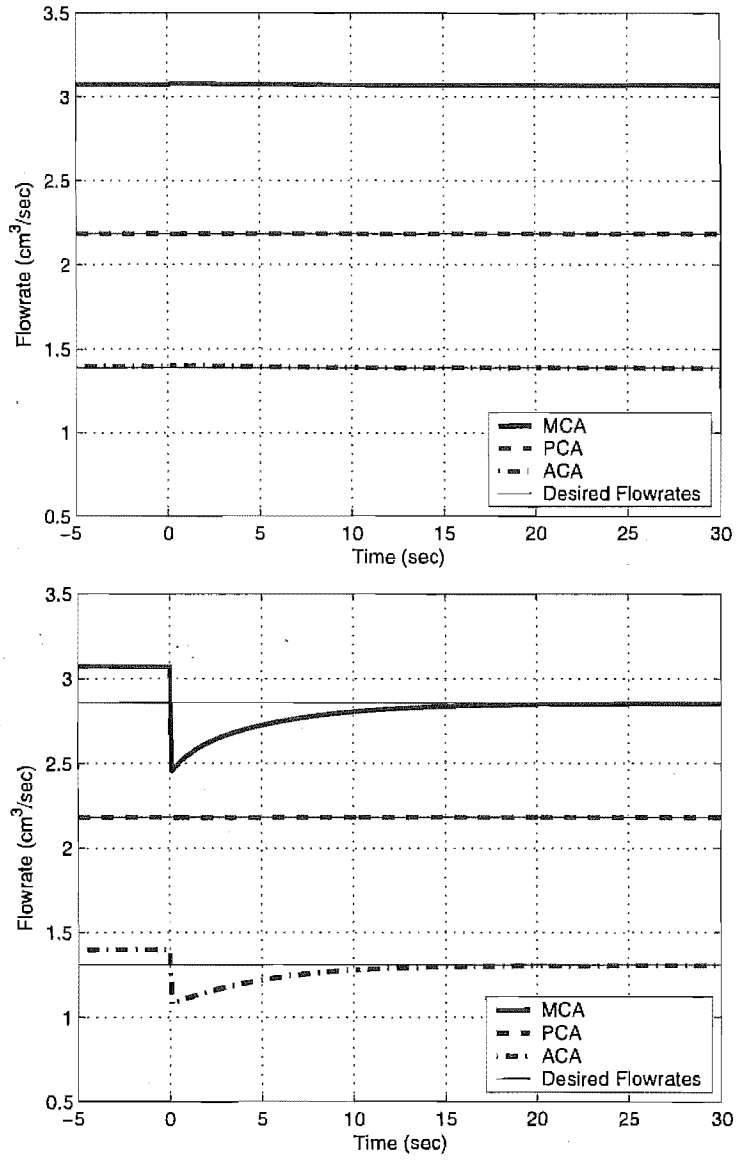

Figure 5.17 Efferent Arterial Response to 20mmHg Pressure Drop in RICA with an Absent ACoA. Left Efferent Response (*top*); Right Efferent Response (*bottom*)

interest, was that the stenosis had the result of initially slightly increasing the flow through the LMCA by 0.2%. This result occurs because flow through the LICA initially increases to help supply right efferent vessels. Because flow can not be redirected to the right side of the circle due to the absence of the $LACA_1$, the LICA flow then decreases, and the LMCA flow decreases to its reference value. The temporal responses of the major efferent vessels are shown in Figure 5.18.

In this absentee case, and also the absent $RACA_1$ case as will be seen, the flowrate through the ACoA is much higher than any other case and over five times

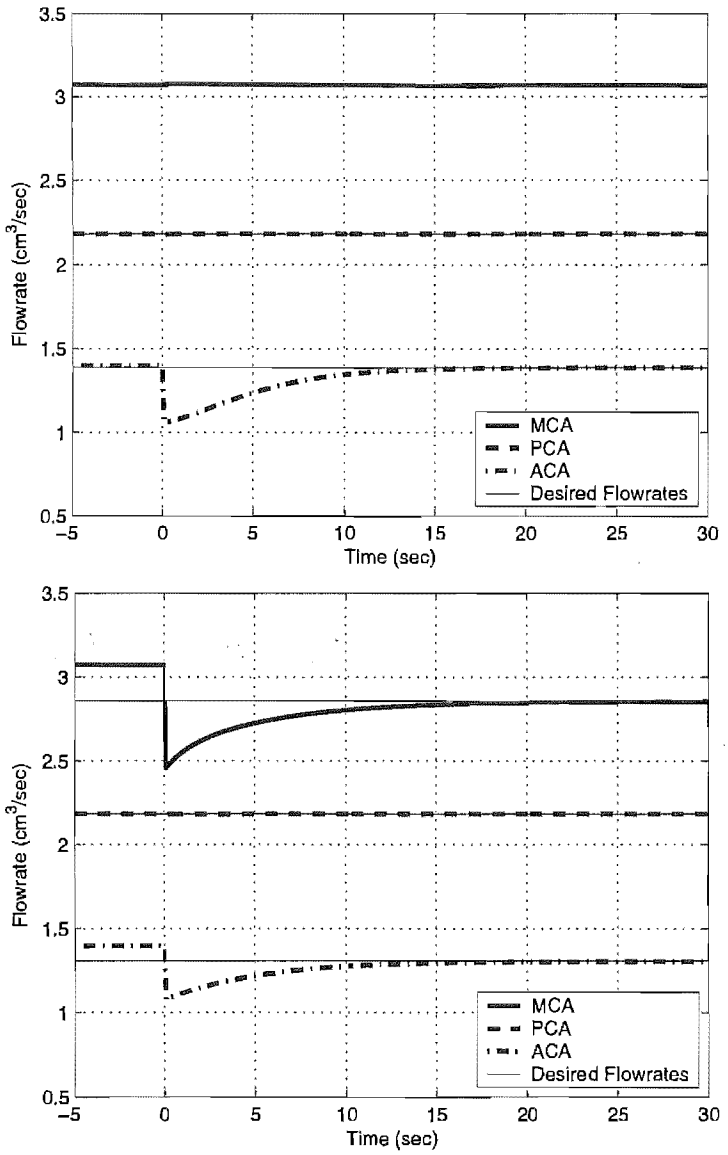

Figure 5.18 Efferent Arterial Response to 20mmHg Pressure Drop in RICA with an Absent $LACA_1$. Left Efferent Response (*top*); Right Efferent Response (*bottom*)

higher than the next highest ACoA flowrate. Flow through the BA has increased after recovery from the stenosis, however flow through the LICA is unchanged, as expected since flow can not be rerouted through the anterior portion of the circle. These changes are observed in Figure 5.19.

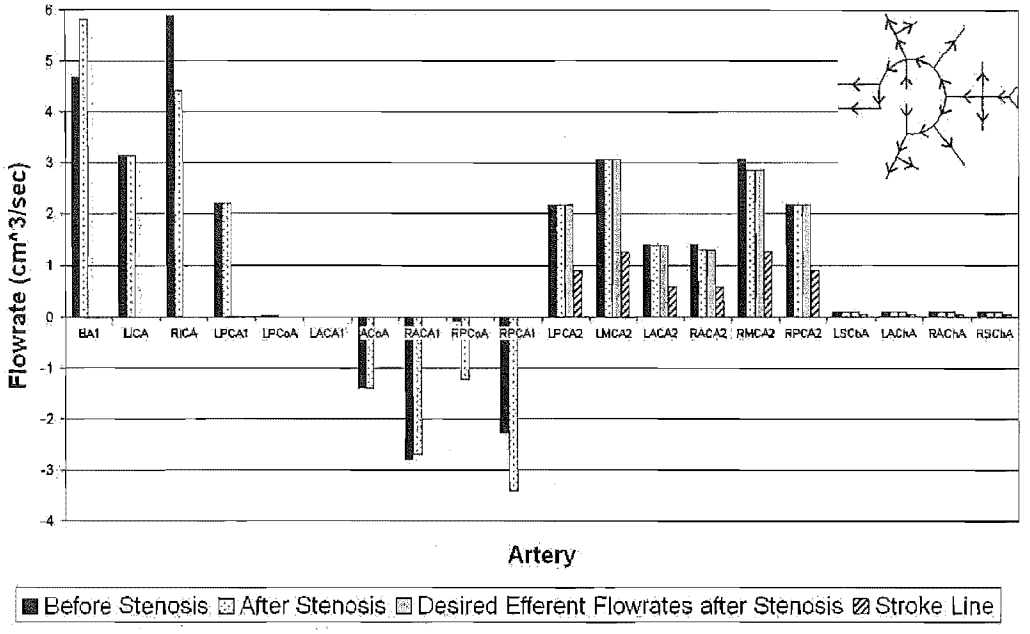

Figure 5.19 Absent $LACA_1$ Configuration Response to 20mmHg Pressure Drop in RICA

5.4.4 Absent $RACA_1$

This case was very similar to an absent ACoA response in that there was very little difference between the pre-pressure drop scenario and the stenosis situation, especially in the left portion of the brain. Immediately after the RICA stenosis, the RMCA dropped 20% before returning to its asymptotic value.Immediately after RICA stenosis in the absent $RACA_1$ case, flow increases through the LMCA, $LACA_2$ and $RACA_2$ by 0.15%, 0.2%, and 3% respectively. Again, this result is due to an increase in flow through the LICA to try to compensate for the loss in the RICA. First, the LMCA is supplied, next the $LACA_2$, and lastly the $RACA_2$ receives not only its desired flow, but also flow intended to aid the RMCA which could not travel through the absent $RACA_1$. Finally, note that all efferent vessels obtain their reference values. The efferent temporal response to simulated stenosis is shown in Figure 5.20.

As in the absent $LACA_1$ case, the flowrate through the ACoA is much higher than any other case and over five times higher than the next highest ACoA flowrate. The flowrate drops through the RICA, and thus as expected, flowrates increase through the BA, LPCoA, and $LPCA_1$ to compensate. FLowrate does not increase through the LICA since flow can not be rerouted through the anterior part of the circle. These flowrate changes are seen in Figure 5.21.

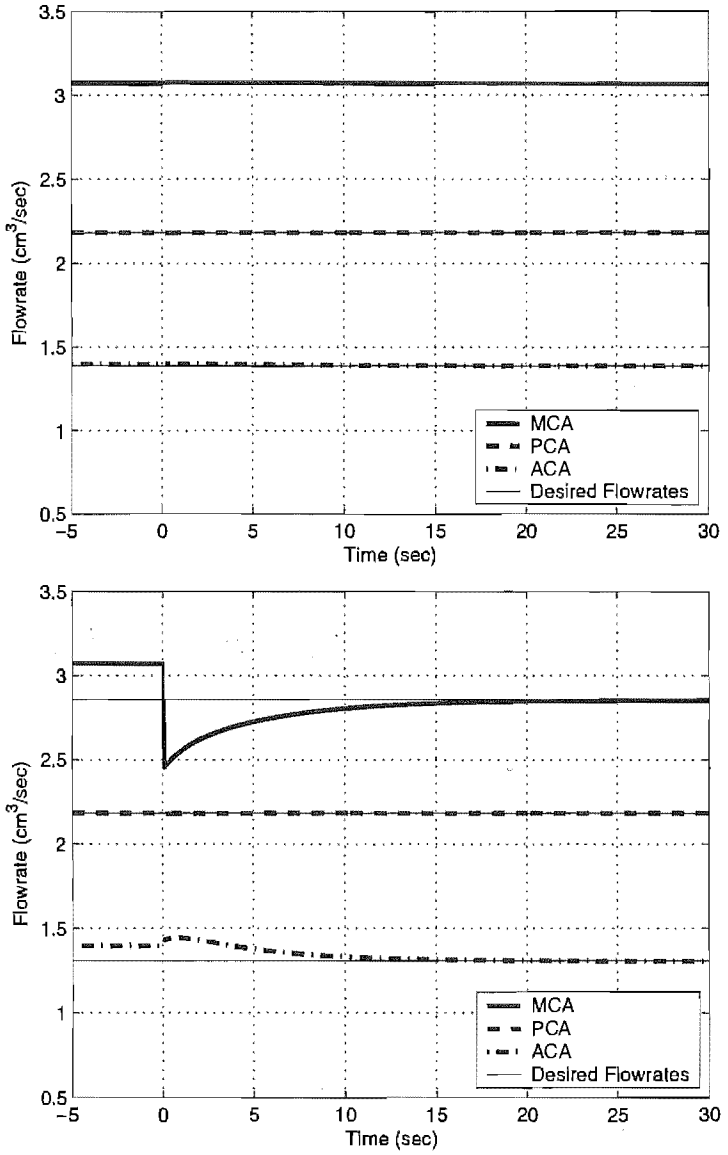

Figure 5.20 Efferent Arterial Response to 20mmHg Pressure Drop in RICA with an Absent $RACA_1$. Left Efferent Response (*top*); Right Efferent Response (*bottom*)

5.4.5 Absent LPCoA

An absent LPCoA has little effect in the pre-pressure drop case due to the high resistance of this vessel. The response is very similar to the balanced case with the most significant change after the pressure drop being the flow through the ACoA. Flowrates increase in the BA and LICA to compensate the loss in the RICA. Consequently, flowrates then increase in the $RPCA_1$ and RPCoA to supply the RMCA from the BA, and increase in the $LACA_1$ to supply the RMCA from

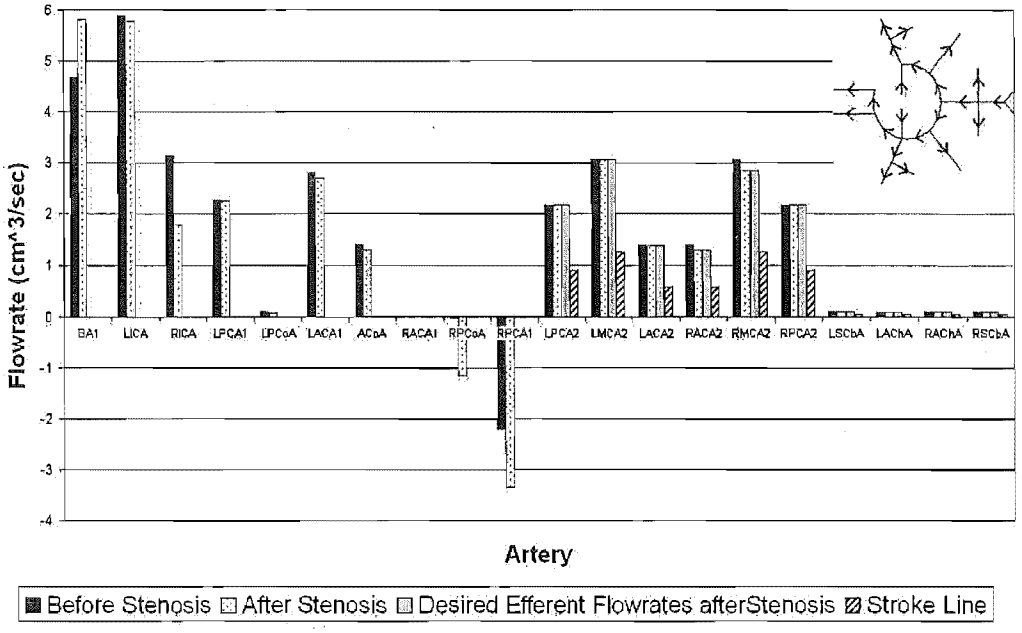

Figure 5.21 Absent $RACA_1$ Configuration Response to 20mmHg Pressure Drop in RICA

the LICA. Flow through the $RACA_1$ even changes direction, to help supply the RMCA from the LICA. These changes are observed in Figure 5.22, and it is noted that all efferent arteries obtain their reference flowrates.

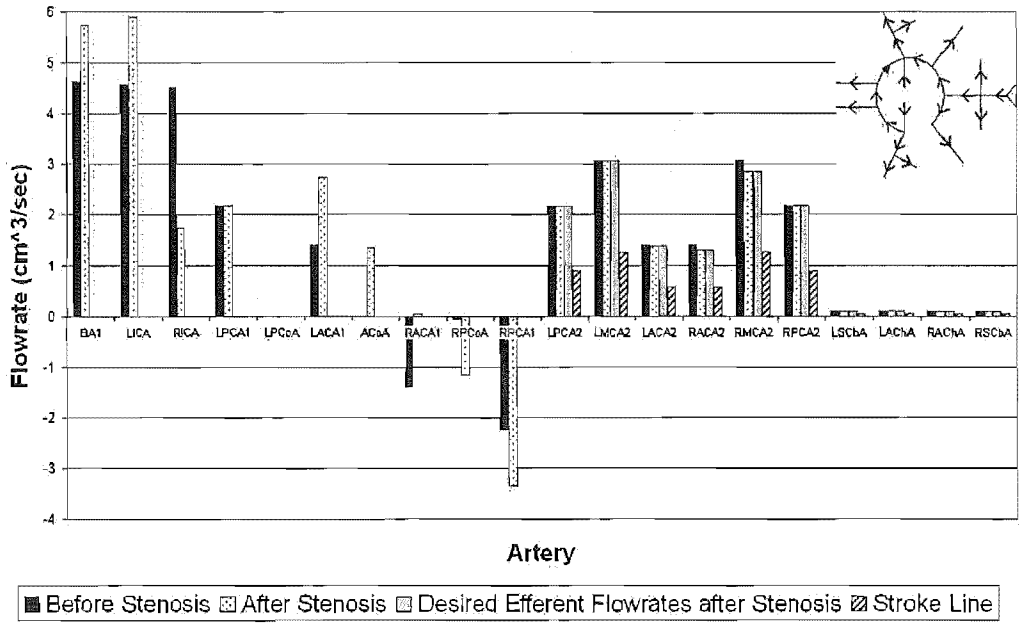

Figure 5.22 Absent LPCoA Configuration Response to 20mmHg Pressure Drop in RICA

The efferent temporal response is shown in Figure 5.22, and it is observed

that flowrates are largely unaffected on the left side of the circle. In contrast, flowrates in the RMCA and $RACA_2$ drop 20% before returning to their reference values.

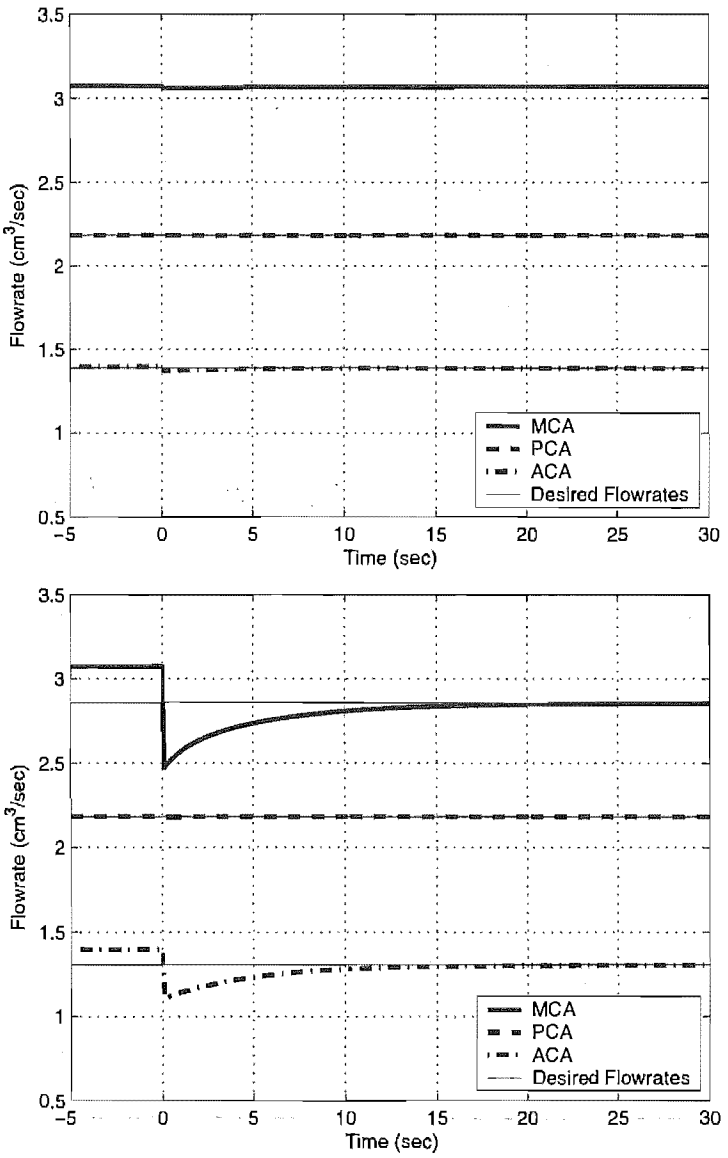

Figure 5.23 Efferent Arterial Response to 20mmHg Pressure Drop in RICA with an Absent LPCoA. Left Efferent Response (*top*); Right Efferent Response (*bottom*)

5.4.6 Absent RPCoA

From the transient responses shown in Figure 5.24, it is seen that the left efferent vessels are largely unaffected by the pressure drop. The RMCA drops 20%, and

the $RACA_2$ drops 21%, before returning to their reference flowrates. In contrast, flow through the $RPCA_2$ increases 0.1% before obtaining its reference value. This result occurs because the BA initially tries to compensate for the drop in flow through the RICA. However, since the RPCoA is missing, flow can not be rerouted via this path.

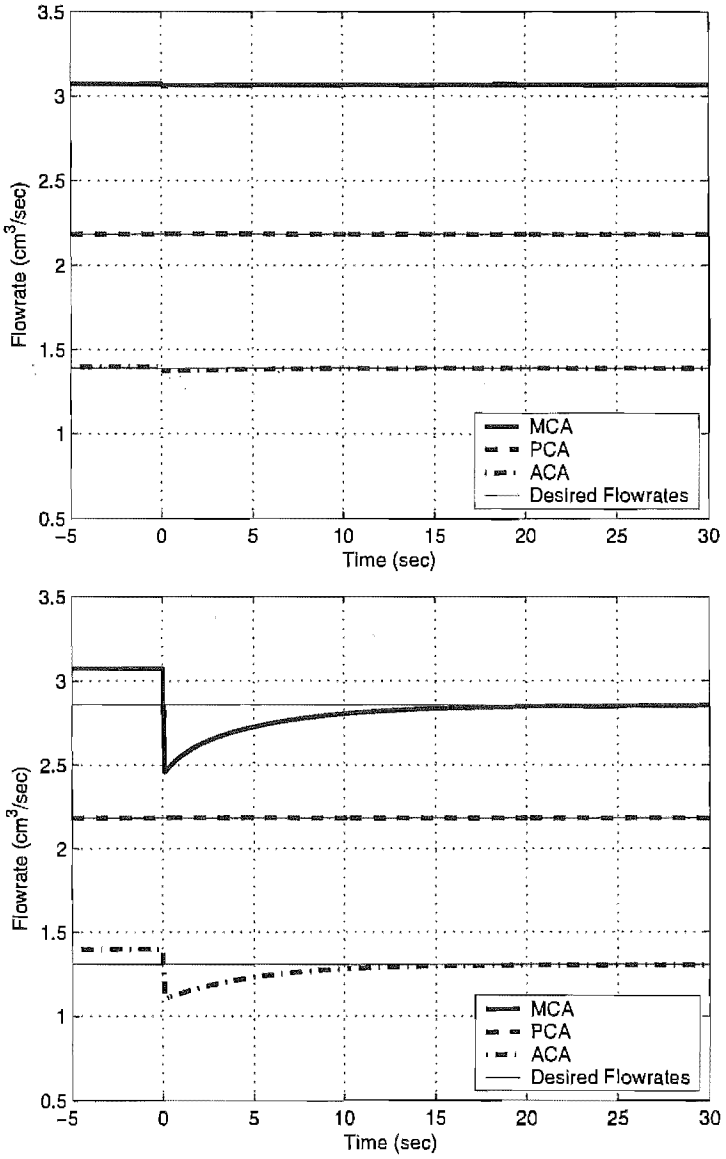

Figure 5.24 Efferent Arterial Response to 20mmHg Pressure Drop in RICA with an Absent RPCoA. Left Efferent Response (*top*); Right Efferent Response (*bottom*)

Again, an absent RPCoA has little effect in the pre-pressure drop case due to this vessel's high resistance. After the pressure drop, flow increases greatly in the LICA, $LACA_1$, and ACoA, as flow is redirected from left side of the circle,

through the anterior regions to help supply the right side of the circle. Flow also changes direction in the $RACA_1$, to help supply the RMCA and RAChA. Note that flow does not increase in the BA after the pressure drop, as it does in the balanced case and absent LPCoA case, since an increased BA flow cannot compensate for the reduced RICA flow with the RPCoA vessel missing. These changes are observed in Figure 5.25.

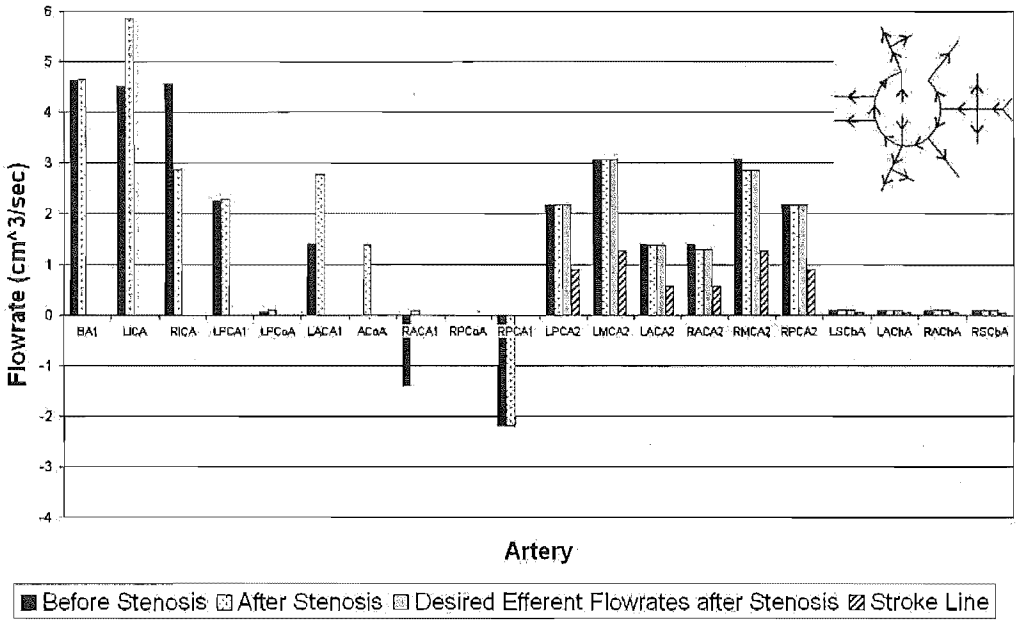

Figure 5.25 Absent RPCoA Configuration Response to 20mmHg Pressure Drop in RICA

5.4.7 Absent $LPCA_1$

With the $LPCA_1$ missing, the BA cannot supply the $LPCA_2$ as it would in all other cases. Consequently, the flowrate through the BA is over 45% less than the other omitted artery cases already discussed in both the normal flow and stenosis situations. The flowrate demanded from the LICA was highest in this absentee situation. The stenosis case demanded a 40% increase in flowrate through the LICA from the normal flow case.

Figure 5.26 shows the transient response to a 20mmHg pressure drop in the RICA. It is observed that the left efferent vessels are relatively unaffected, but the RMCA and $RACA_2$ flowrates drop 20% before obtaining their reference values.

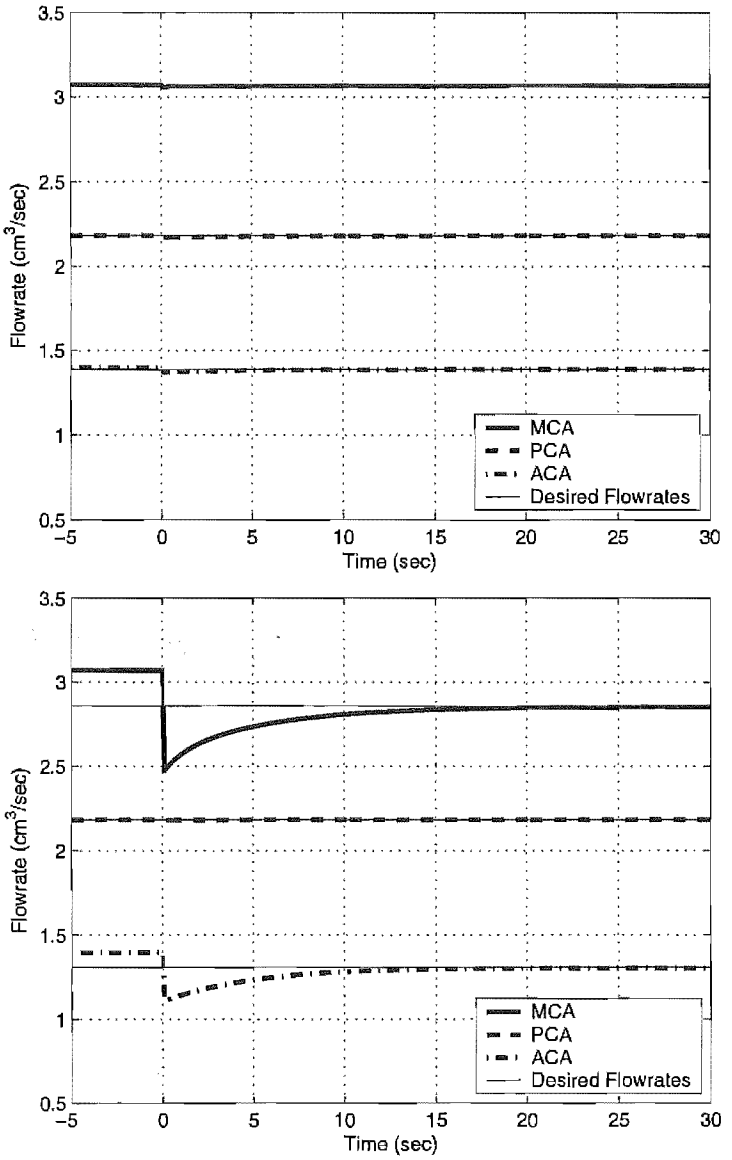

Figure 5.26 Efferent Arterial Response to 20mmHg Pressure Drop in RICA with an Absent $LPCA_1$. Left Efferent Response (*top*); Right Efferent Response (*bottom*)

Before the pressure drop, the LICA supplied the $LPCA_2$ and LMCA, as well as meeting most of the $LACA_2$'s demands. After the pressure drop, flow is sent through the ACoA and supplies most of the $RACA_2$ as well as all left efferent arteries. It is noted that all efferent vessels obtain their reference flowrates, as seen in Figure 5.27.

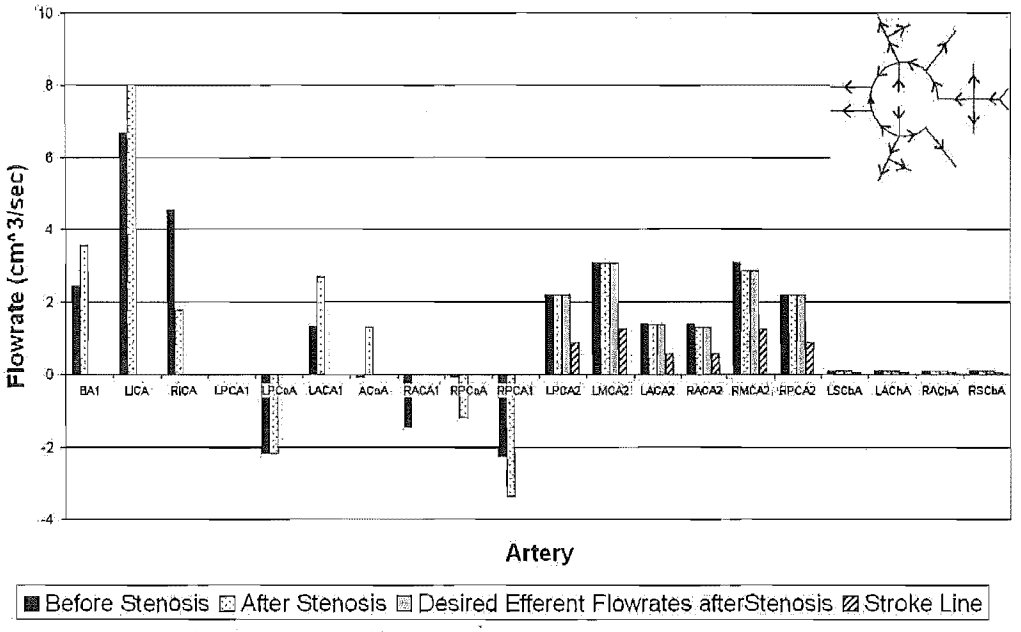

Figure 5.27 Absent $LPCA_1$ Configuration Response to 20mmHg Pressure Drop in RICA

5.4.8 Absent $RPCA_1$

With the $RPCA_1$ missing, the BA cannot supply the $RPCA_2$ as it would in all other cases. Consequently, the flowrate through the BA is over 45% less than the other omitted artery cases already discussed in both the normal flow and stenosis situations. The flowrate was twice as high through the RPCoA as any of the other absentee cases. After the pressure drop, flow is rerouted from the left to the right side of the circle through the ACoA. It is observed in Figure 5.28, that reference flowrates are *not* obtained after the pressure drop.

There is a much larger response to the RICA pressure drop in the $RPCA_2$ than in any other case with an initial reduction in flowrate of 24%. After the pressure drop, the $RPCA_2$ is only able to obtain 77% of its reference flow, although remains well above the 'stroke line', as seen in Figure 5.29. This result occurs because of the high pressure differential required through the RPCoA due to this vessel's high resistance. As a consequence, flow increases through the remaining efferent arteries. Note that clinically, this result is rarely seen, because individuals with a string-like or absent PCA_1 tend to have an ipsilateral PCoA with an increased radius and/or decreased length, thus reducing its resistance by Equation 2.2. When this simulation is repeated with the RPCoA's length decreased by 86%, and

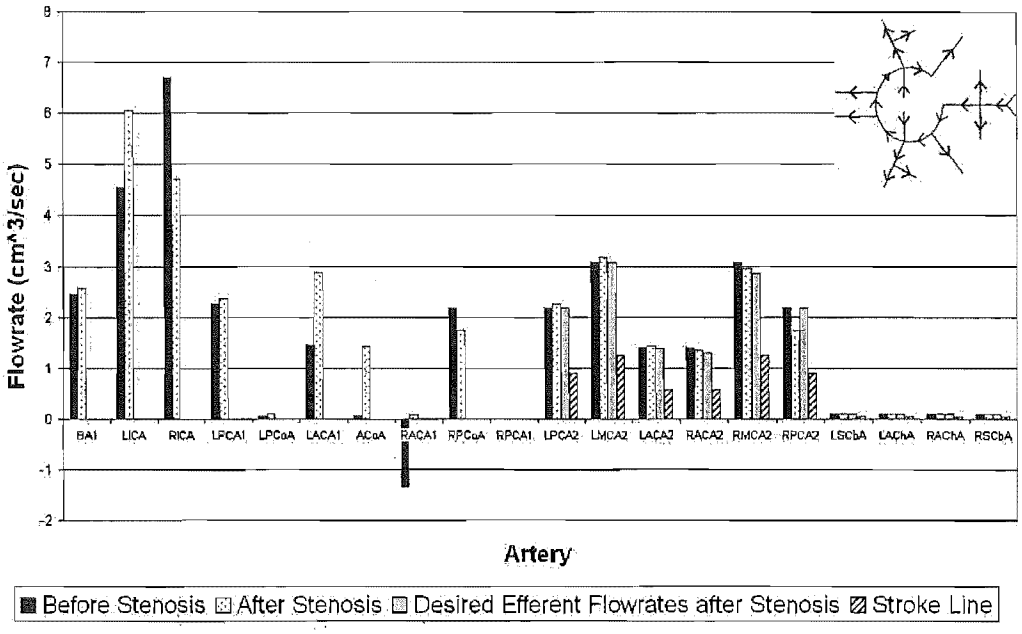

Figure 5.28 Absent $RPCA_1$ Configuration Response to 20mmHg Pressure Drop in RICA

its radius increased by 136% [Arnold et al., 2004], such that its overall resistance is decreased by 75%, reference flow is obtained after the pressure drop, as seen in Figure 5.30.

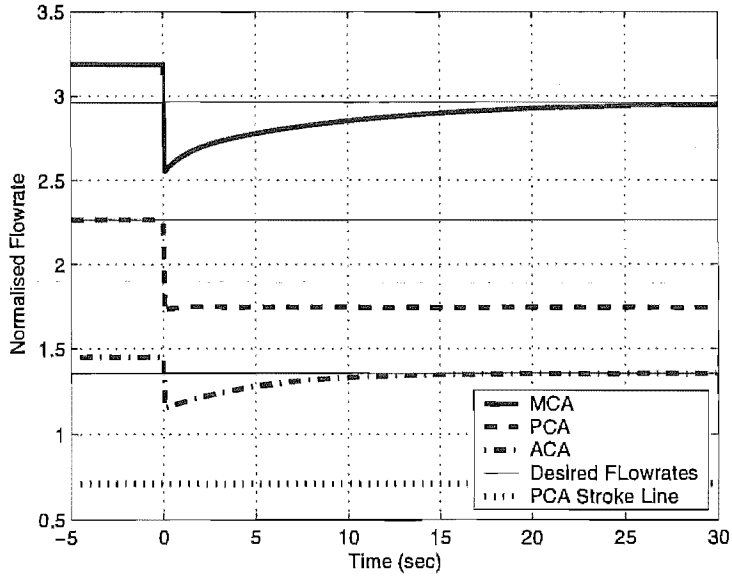

Figure 5.29 Right Efferent Arterial Response to 20mmHg Pressure Drop in RICA with an Absent $RPCA_1$

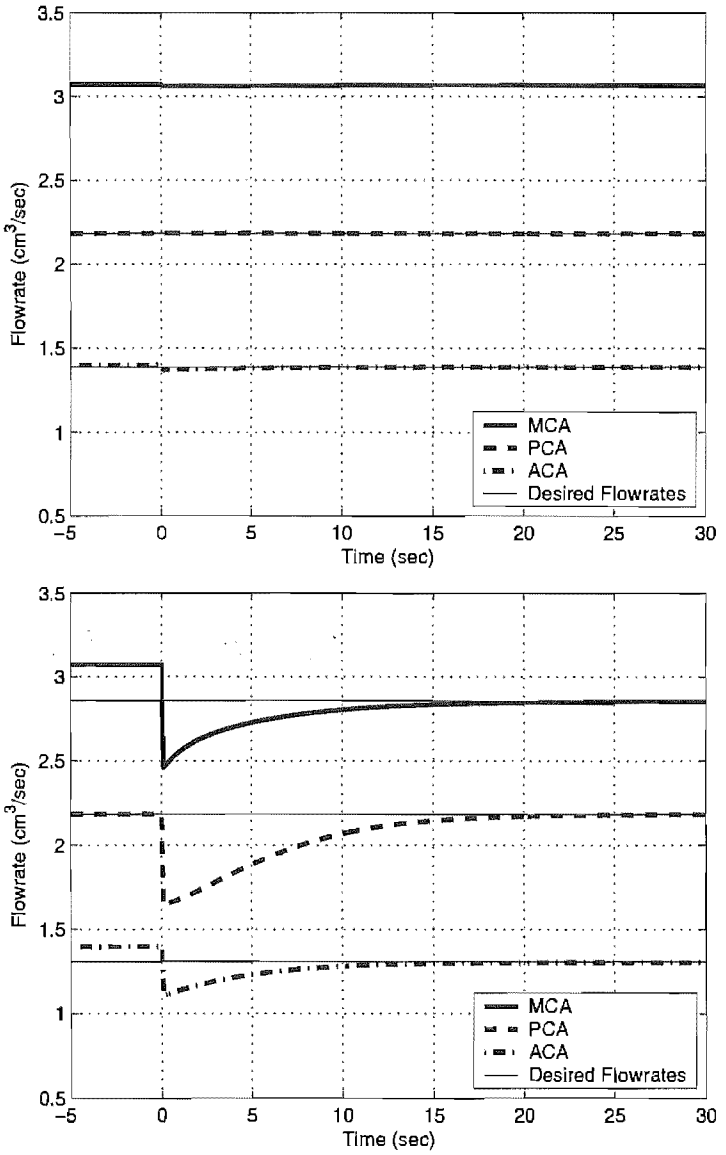

Figure 5.30 Efferent Arterial Response to 20mmHg Pressure Drop in RICA with an Absent $RPCA_1$. Left Efferent Response (*top*); Right Efferent Response (*bottom*)

5.4.9 Stroke Risk Case I

All the prior cases with a single omitted artery were able to maintain the reference flowrate in all the efferent arteries, showing the robustness of the CoW system as a whole. This case represents a realistic situation of increased stroke risk where the autoregulation process cannot keep the efferent flowrates at the desired level. A situation is modelled in which the RPCoA is absent and an 80% carotid stenosis is simulated by suddenly increasing left and right ICA resistances. The RMCA,

$RACA_2$ and RAChA drop below the ischaemic threshold representing a potential stroke, as shown in Figures 5.31 and 5.32.

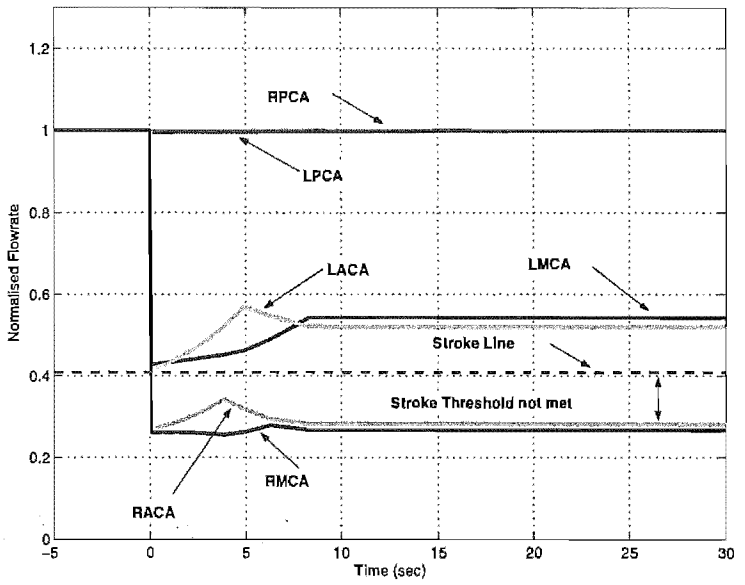

Figure 5.31 Efferent Arterial Response to 80% Carotid Stenosis with an Absent RPCoA

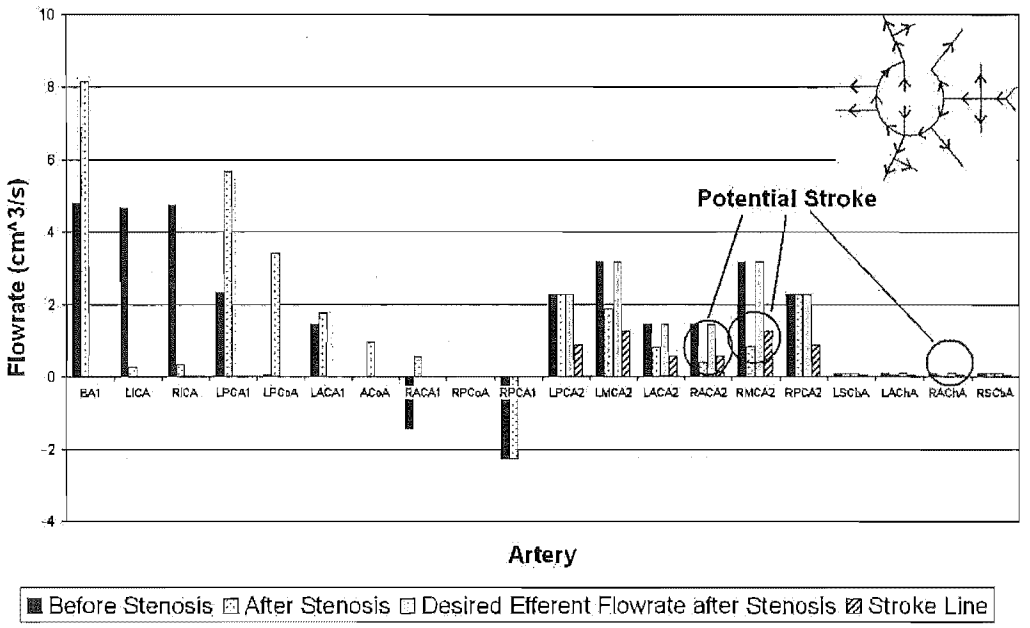

Figure 5.32 80% Carotid Stenosis with Absent RPCoA

This failure to return to reference flowrate occurs because the resistance of the $RACA_2$, RMCA and RAChA cannot be further decreased since the maximum radius of these arteries has been reached as a result of the autoregulation process model. The final flowrate is not only lower than the desired value, but also falls

below the ischaemic threshold, leading to reduced perfusion and higher stroke risk for this type of input. Note in Figure 5.31 that the flowrates are normalised to each efferent artery's 'normal' balanced configuration reference value, and the SCbA's and AChA's are not shown due to the tiny amount of flow through these vessels.

5.4.10 Stroke Risk Case II

As mentioned earlier, at a MAP of 34mmHg the stroke line intersects with the model. Therefore, simulations are performed at afferent pressures just above and just below 34mmHg for verification. When an afferent pressure drop to 35mmHg is simulated, stroke *does not* follow, as shown in Figure 5.33, and when an afferent pressure drop to 33mmHg is simulated, stroke *does* follow, as shown in Figure 5.34. Note that since the circle geometry and pressure drop are symmetrical, left and right efferent flux profiles are identical.

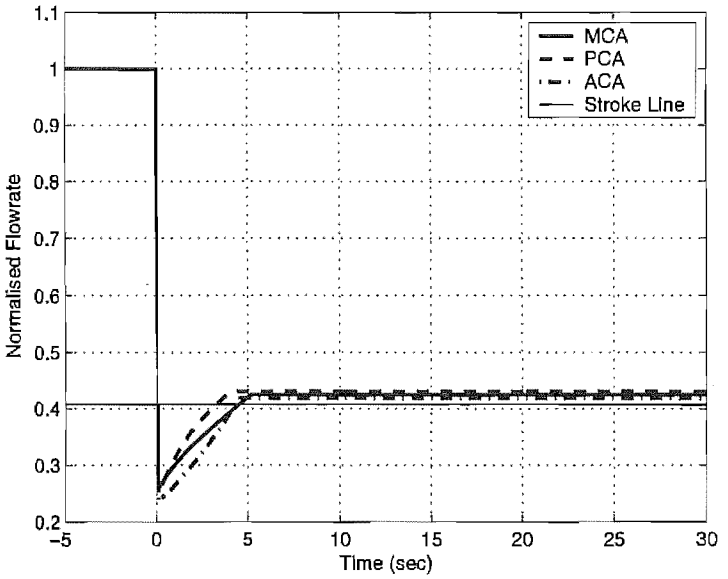

Figure 5.33 Efferent Arterial Response to Afferent Drop to 35mmHg

In Figures 5.33 and 5.34 it is observed that at approximately time $t = 5$ seconds, the flux profile gradients change discontinuously - a result that is probably not observed physiologically. The cause of this discrepancy is the resistance model employed. The resistance model assumes that vessel diameters change as required until they reach the imposed limits, at which point they are abruptly set to their resistance limit. In contrast, real vessels most likely stretch to their

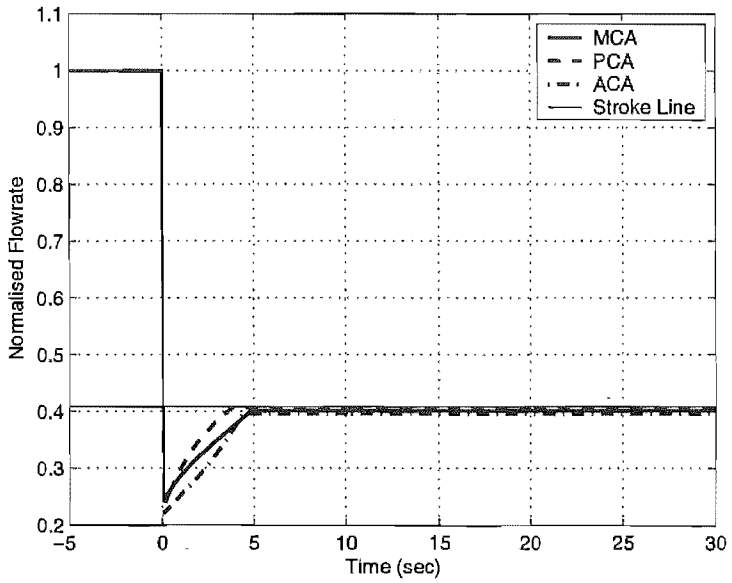

Figure 5.34 Efferent Arterial Response to Afferent Pressure Drop to 33mmHg

limit, rather than reach it abruptly as assumed in the model. These differences are shown schematically in Figure 5.35.

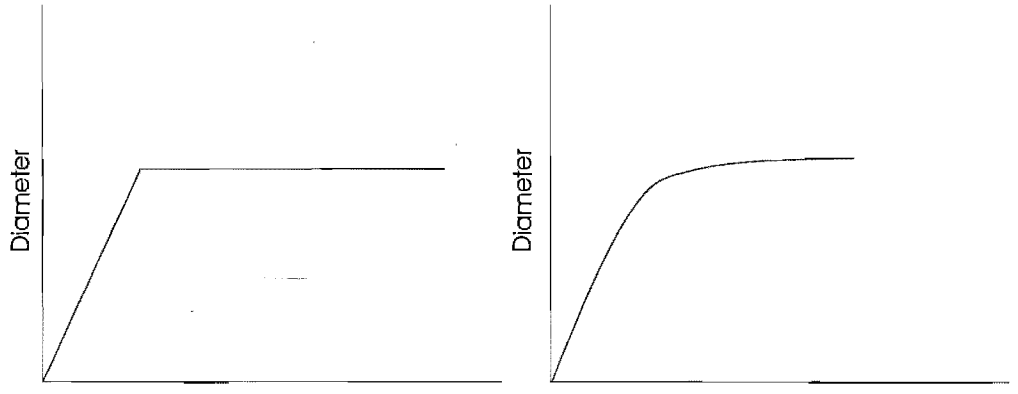

Figure 5.35 Resistance Models. a) Model Employed (*left*); b) More Physiologically Accurate Model (*right*)

In addition, physiologically, once arterioles reach their maximum dilation, their resistance can not be further decreased, and consequently, CBF starts to decrease. This decrease in flow results in less oxygen being delivered to the tissues such that there is a greater concentration difference driving oxygen diffusion to

the tissues. Therefore the amount of oxygen extracted from the tissues increases to a maximum limit, thus initially partially compensating for the reduction in flow.

5.5 Summary

A 1D CFD model of the Circle of Willis has been created to study autoregulation of cerebral blood flow for clinical events such as occlusions or stenoses in afferent arteries, absent or string-like circle vessels, or arterial infarctions. The model captures cerebral haemodynamic autoregulation using PID controllers to modify efferent artery resistances and partial pressures of oxygen to maintain optimal efferent flowrates for a given circle geometry and afferent blood pressure.

The model is physiologically relevant, matching the accepted physiological responses of blood flow as a function of arterial pressure, tissue oxygen partial pressure as a function of blood flow, as well as limited clinical data. The two dynamics account for metabolic autoregulation with appropriate time constants associated with firstly oxygen diffusion and metabolite generation, and secondly peripheral arterial wall vasoconstriction and vasodilation.

Results show excellent correlation with the clinical data. The time-dependent velocity profiles in the MCA were matched to give a 20% decrease in flowrate, followed by approximately 20 seconds to return to steady state conditions in response to a stenosis in the RICA. Simulations have been performed with the omission of any single circulus artery and found that no such omission leads to failure in reaching the required efferent flowrates for a RICA stenosis, thus highlighting the known robustness of the CoW system. A physiologically realistic case with an absent RPCoA and an 80% carotid stenosis was developed and simulated, and it was observed that the RMCA, $RACA_2$, and RAChA flowrates fell below the ischaemic threshold, indicating a possible stroke. This result shows the effectiveness of this model as a tool for determining potential outcomes of surgical or other therapies.

Chapter 6

Conclusions

1D CFD models of the Circle of Willis have been created to study autoregulation of cerebral blood flow for clinical events, such as occlusions or stenoses in afferent arteries, absent or string-like circle vessels, or arterial infarctions. Cerebral haemodynamic autoregulation is captured using PID controllers to maintain optimal efferent flowrates for a given circle geometry and afferent blood pressure. The primary clinical goal is to create a model that can be used to study potential clinical outcomes from surgical or other interventions and effects.

The model presented in Chapter 2 is very simple and captures autoregulation using minimal physiological dynamics. Although some good results and correlations with prior models and clinical data were achieved, the model was too simple to capture all the transient dynamics clinically observed in autoregulation. However, this model was computationally a significant advance over pre-existing models in its incorporation of inner iterations at each solution time-step to find the model equilibrium state, within broad physiological limitations. The inner iterations recognise the non-linearity of the cerebral circulatory system and the autoregulation process in particular, as well as the need to meet equilibrium conditions to ensure a valid solution. Hence, this iterative solution method was retained in subsequent models.

Chapter 3 compared results obtained from the 1D model with results from a 3D CFD model, to verify modelling assumptions, such as approximating blood flow using the Poiseuille flow approximation. Again, some very good correlations were achieved. However, the comparative study pointed out certain limitations in the 1D model, such as the Poiseuille flow approximation allowing for too much flow through the short, geometrically complex communicating arteries. The 3D

THE LIBRARY
UNIVERSITY OF CANTERBURY
CHRISTCHURCH, N.Z.

model made less simplifying assumptions, and therefore with lack of sufficient clinical data, is expected to be a more physiologically accurate model. However, the major disadvantage of the 3D model is the excessive length of time required to run simulations, thus making it impractical as a clinical tool. In contrast, using the 1D model, the solution for the CoW arterial system is obtained in a far shorter time period, and requires significantly less computational effort while retaining a high level of accuracy.

Chapter 4 investigated the decentralised nature of autoregulation control. With wide dilatory resistance limits of $\pm 95\%$, results showed that if a sudden occlusion is imposed in an afferent artery, a 'tug of war' scenario occurs, such that efferent flux profiles fluctuate as a balance is found that best satisfies the independent requirements of each territory of the cerebral mass. However, further investigation found that the physical limits of vessel contraction and dilation of $\pm 95\%$, were not well defined, and did not match the accepted physiological response of blood flow as a function of MAP. With physiologically realistic, tighter resistance limits matched to data from Guyton and Hall [1996], this blood stealing phenomenon was minimized, but not eliminated. Hence, it can be concluded that, clinically, the decentralised aspect of cerebral autoregulation could result in ischaemic stroke after sudden pressure drops due to stenoses or occlusions, where a centralised controller would have a different outcome.

Results obtained in Chapters 2-4 indicated that a more physiologically realistic model was required to overcome the limitations observed in the model. An advanced model was created that included the successful components of the previous model such as PID autoregulation control, as well as better resistance limits for smooth muscle vasomotion, and the oxygen dynamics that physiologically drive the autoregulatory response. This advanced model is more physiologically relevant, matching the accepted physiological responses of blood flow as a function of arterial pressure and tissue oxygen partial pressure as a function of blood flow, as well as matching the limited transient clinical data. Cerebral haemodynamic autoregulation is captured by using a PID controller to modify efferent artery resistances and partial pressures of oxygen to maintain optimal efferent flowrates and oxygen supply to the cerebral mass for a given circle geometry and afferent blood pressure.

Results from the advanced metabolic model show excellent correlation with

the clinical data. The time-dependent velocity profiles in the MCA were matched to give a 20% decrease in flowrate, followed by approximately 20 seconds to return to steady state conditions in response to a stenosis in the RICA. In addition, the two dynamics allowed for a much greater flexibility in efferent flux profiles than the simpler model, such that the specific flux profile matching the clinical data of Newell et al. [1994] showed excellent correlation, with a maximum error of 2.58% and an average error of 1.03%.

Simulations with the omission of any single circulus artery found that no such omission leads to failure in reaching the required efferent flowrates for a RICA stenosis, except in the ipsilateral PCA_1, thus highlighting the known robustness of the CoW system. More specifically, with an absent ipsilateral PCA_1, after a 20mmHg pressure drop was simulated in the RICA, reference flow was not obtained in the $RPCA_2$, however the flowrate remained above the ischaemic threshold. Clinically this result is rarely seen, because individuals with a string-like or absent PCA_1 tend to have an ipsilateral PCoA with an increased radius and/or decreased length, thus reducing its resistance to flow. When this simulation was repeated with a shorter, thicker RPCoA, reference flow *was* obtained after the pressure drop, thus matching anecdotal clinical data.

A physiologically realistic case with an absent RPCoA and an 80% carotid stenosis was developed and simulated, and it was observed that the RMCA, $RACA_2$, and RAChA flowrates fell below the ischaemic threshold, indicating a possible stroke. A second 'stroke risk' case was simulated in order to determine the MAP at which stroke would likely ensue, given a 'normal' CoW geometry. The critical MAP was found to be approximately 34mmHg, which matched the result seen from Guyton and Hall [1996] when an ischaemic threshold of 20mL/100g/min was set [Heiss et al., 1999; Baron, 2001]. These results show the effectiveness of this model as a tool for determining potential outcomes of surgical or other therapies such as endarterectomy, given a patient specific geometry that can be obtained from MRA data.

Overall, 1D CFD models of the CoW have been developed, modified, and verified. These models can take readily available patient specific geometry and capture complex transient, autoregulated haemodynamics. The model and modelling methods have been shown to have good clinical potential for diagnosis and therapy testing of ischaemic events prior to intervention.

Chapter 7

Future Work

One of the biggest obstacles for this research at this stage, is the lack of clinical data for verification. Clinical data will be used to model a greater variety of potential CoW geometries, and correlation to retrospective outcomes will indicate any specific model limitations and increase the level of validation. Currently, work is underway within the research group to perform a statistical analysis of common CoW abnormalities observed from MRA data. In addition, more transient data is required, to study exactly how the CoW reacts to various conditions, as opposed to simply the end result after a steady state is resumed.

The next step in expanding the model, is to incorporate models for myogenic autoregulation, in which vasodilation and vasoconstriction of peripheral vessel walls occurs, to a certain degree, directly in response to changes in transmural pressure in the artery wall. This addition will effectively involve adding another dynamic to the model, and it is postulated that the myogenic response be modelled with a small time constant, allowing for a fast, imprecise change in vessel calibre, while the metabolic response be modelled with bigger time constants providing a slower but more accurate control response.

The current model does not take into account collateral flow from pial vessels. At present, were an efferent vessel to become blocked, the region of cerebral tissue supplied by that vessel would die. Physiologically, that tissue may also receive low levels of collateral flow, and therefore the situation may not be a dire as represented by the model. This approach of including collateral flow would also make it possible to model stoke severity. As such, the extent of the ischaemic core, where the CBF is less than 12mL/100g/min, and the ischaemic penumbra, where CBF is 12-23mL/100g/min, could be determined under a variety of pathological

conditions. The difficulty in modelling collateral flow, is in obtaining sufficient clinical data about the geometry and resistance of the pial arteries. In addition, collateral vessels can develop in response to a blockage, but the extent to which this angiogenesis occurs is extremely variable and generally unknown.

Advancements to the 3D CFD model will include studying embolism behaviour, using *Fluent* Macroscopic Particle Model (MPM) software. MPM is used to model the interaction of large scale particles within a fluid flow. Therefore, embolic pathways could be modelled by creating a 3D model of the arterial network, and releasing macroscopic particles representing emboli into the bloodstream, and tracking their movement.

Although many of the theoretical aspects of cerebral autoregulation are reasonably well understood, there is little point pursuing overly complex models that require parameters that can not be measured. Therefore, the underlying goal of all future research is to develop models that are physiologically accurate, but contain parameters that can be readily measured and/or matched to clinical data.

References

B. J. Alpers and R. G. Berry. Circle of Willis in Cerebral Vascular Disorders. *Archives of Neurology*, 8:398–402, 1963.

B. J. Alpers, R. G. Berry, and R. M. Paddison. Anatomical Studies of the Circle of Willis in Normal Brain. *AMA Archives of Neurology*, 81:409–418, 1959.

J. Arnold, J. Fink, T. David, J.G. Chase, S. Moore, K.T. Moorhead, and S. Alzaidi. Anatomical variations of the Circle of Willis and magnetic resonance measurement techniques. In *Annual Conference of the Australasian College of Physical Scientists and Engineers in Medicine (ACPEM)*, Christchurch, 2004.

J.C. Baron. Perfusion thresholds in human cerebral ischemia: historical perspective and therapeutic implications. *Cerebrovasc Dis*, 11:2–8, 2001.

S. K. Battacharji, E. C. Hutchinson, and A.J. McCall. The Circle of Willis - the incidence of developmental abnormalities in normal and infarcted brains. *Brain*, 90:747–758, 1967.

F. Cassot, M. Zagzoule, and J. Marc-Vergnes. Hemodynamic role of the circle of Willis in stenoses of internal arteries. An analytical solution of a linear model. *Journal of Biomechanics*, 33:395–405, 2000.

G. V. Childs. University of Texas Medical Branch Microanatomy Class - Smooth Muscle Study Guide. *http://www.cytochemistry.net/microanatomy/muscle/smoothmuscle2001.htm*, 2001.

M.J. Cipolla, N.I. Gokina, and G. Osol. Pressure-induced actin polymerisation in vascular smooth muscle as a mechanism underlying Myogenic behaviour. *FASEB*, 16, 2002.

San Mateo County Community College. San Mateo County Community College - Muscles and Muscle Tissue, 2002.

R.E. Collins. *Flow of Fluids through Porous Materials.* Reinhold Publishing Corp., New York, 1961.

M.J. Davis, J.A. Donovitz, and J.D. Hood. Stretch-activated single-channel and whole cell currents in vascular smooth muscle cells. *American Journal of Physiology*, Apr; 262((4 Pt 1)):C1083–8, 1992.

Ulrich Dirnagl and William Pulsinelli. Autoregulation of Cerebral Blood Flow in Experimental Focal Brain Ischaemia. *Journal of Cerebral Blood Flow and Metabolism*, 10:327–336, 1990.

A. Ferrandez, T. David, J. Bamford, J. Scott, and A. Guthrie. Computational Models of Blood Flow in the Circle of Willis. *Computer Methods in Biomechanics and Biomedical Engineering*, 4:1–26, 2000.

A. Ferrandez, T. David, and M. D. Brown. Numerical Models of Auto-regulation and Blood Flow in the Cerebral Circulation. *Computer Methods in Biomechanics and Biomedical Engineering*, 5(1):7–20, 2002.

M. Fog. Cerebral Circulation. The reaction of plial arteries to a fall in blood pressure. *Arch, Neurol. Pyschiat.*, 37:351–364, 1937.

Y.C. Fung. *Biomechanics: Motion, Flow, Stress and Growth.* Springer-Verlag Inc., New York, 1990.

E. Gao, W. L. Young, J. Pile-Spellman, E. Orstein, and Q. Ma. Mathemathical considerations for modeling cerebral blood flow autoregulation to systemic arterial pressure. *American Journal of Physiology*, 43:H1023–H1031, 1998.

D. Gebremedhin, P. Bonnet, A.S. Greene, S.K. England, N.J. Rusch, J.H. Lombard, and D.R. Harder. Hypoxia increases the activity of Ca^{2+}-sensitive K^{+} channels in cat cerebral arterial muscle cell membranes. *Pflugers Arch*, Oct;428: 621–30, 1994.

A.C. Guyton and J.E. Hall. *Textbook of Medical Physiology.* W.B. Saunders Company, Philadelphia, 9 edition, 1996.

W-D. Heiss, A. Thiel, M. Grond, and R. Graf. Which Targets are Relevant for Therapy of Acute Ischaemic Stroke? *Stroke*, 30:1486–1489, 1999.

B. Hillen, B.A. Drinkenburg, H.W. Hoogstraten, and L. Post. Analysis of flow and vascular resistance in a model of the circle of Willis. *Journal of Biomechanics*, 21(10):807–14, 1988.

B. Hillen, H.W. Hoogstraten, and L. Post. A mathematical model of the flow in the circle of Willis. *Journal of Biomechanics*, 19.(3):187–94, 1986.

A.G. Hudetz, J.H. Halsey, and C.R. Horton. Mathematical Simulation of Cerebral Blood Flow in Focal Ischemia. *Stroke*, 13(5):693–700, 1982.

Z.S. Katusic, J. Schugel, F. Cosentino, and P.M. Vanhoutte. Endothelium-dependent contractions to oxygen-derived free radicals in the canine basilar artery. *American Journal of Physiology*, Mar; 264:H859–64, 1993.

J. Keener and J. Sneyd. *Mathematical Physiology*, volume 8. Springer-Verlag, NewYork, 1998.

K. Ketchum. University of Wisconsin, Department of Radiology - NeuroRadiology Tutor. *www.radiology.wisc.edu/MedStudents/neuroradiology/NeuroRad/NeuroRad*, 2003.

R. E. Klabunde. *Cardiovascular Physiology Concepts*. Lippincott Williams & Wilkins, 2004.

J.B. Lansman, T.J. Hallam, and T.J. Rink. Single stretch-activated ion channels in vascular endothelial cells as mechanotransducers? *Nature*, 325(6107):811–3, 1987.

J. Lodder, R. Hupperts, A. Boreas, and F. Kessels. The size of territorial brain infarction on CT relates to the degree of internal carotid artery obstruction. *Journal of Neurology*, 243(4):345–349, 1996.

C. A. Lodi, M. Ursino, P. Di Giammarco, and E. Belardinelli. Hemodynamic Effect of Cerebral Vasospasm in Humans: A Modeling Study. *Annals of Biomedical Engineering*, 27:257–273, 1999.

G. Mancia and A.L. Mark. *Arterial Baroreflexes in Humans, volume 3 of Handbook of Physiology, Section 2.* American Physiological Society, New York, 1983.

S.M. Moore, K.T. Moorhead, J.G. Chase, T. David, and J. Fink. 1D and 3D Models of Cerebrovascular Flow. *ASME J. Biomechanics*, accepted 7/04 - to appear, 2004.

K.T. Moorhead, C.V. Doran, J.G. Chase, and T. David. Lumped Parameter and Feedback Control Models of the Auto-regulatory Response in the Circle

of Willis. *Computer Methods in Biomechanics and Biomedical Engineering*, 7 (3):121–130, 2004.

D. W. Newell, R. Aaslid, and A. Lam. Comparison of Flow and Velocity During Dynamic Autoregulation Testing in Humans. *Stroke*, 25(4):793–797, 1994.

U. Peiper and R. Laven. *Noradrenaline and pH effects at the membrane of vascular smooth muscle.* Ionic Actions on Vascular Smooth Muscle. Berlin, 1976.

S. K. Piechnik, M. Czosnyka, K. Cieslicki, and D. Ciesla. Problems in application of purely linear models in cerebral circulation. *Journal of Biomechanics*, 35: 553–554, 2002.

W.K. Purves, G.H. Orians, and H.C. Heller. *Life. The Science of Biology.* Sinauer Associates Inc., Massachusetts, 1995.

D. Randall, W. Burggren, and K. French. *Eckert Animal Physiology: Mechanisms and Adaptations.* W.H. Freeman and Company, 2002.

R. Riggs and C. Rupp. Variation in form of Circle of Willis. The relation of hte variations to collateral circulation: anatomic analysis. *Archives of Neurology*, 8:24–30, 1963.

G.M. Rubanyi, A.D. Freay, K. Kauser, A. Johns, and D.R. Harder. Mechanoreception by the endothelium: mediators and mechanisms of pressure- and flow-induced vascular responses. *Blood Vessels*, 27:246–57, 1990.

G. Siegel, H. Gustavsson, R. Ehehalt, and B. Lindman. The role of membrane potential in the regulation of vascular tone. *Biblthca anat.*, 15:126–135, 1977.

G.J. Tortora. *Introduction to the Human Body: The Essentials of Anatomy and Physiology.* Addison Wesley Longman Inc., 4 edition, 1997.

A. van der Zwan, B. Hillen, C. A. F. Tulleken, and M. Dujovny. A Quantitative Investigation of the Variability of the Major Cerebral Arterial Territories. *Stroke*, 24:1951–1959, 1993.

A. Vander, J. Sherman, and D. Luciano. *Human Physiology - The Mechanisms of Body Function.* McGraw Hill, 8 edition, 2001.

F.J.M. Walters. Intracranial Pressure and Cerebral Blood Flow. *Update in Anaesthesia*, (8):4:1–4, 1998.